

CONTROL OF STATIONARY CROSSFLOW MODES
USING PASSIVE PATTERNED ROUGHNESS AND DBD PLASMA
ACTUATORS AT MACH 3.5

A Dissertation

Submitted to the Graduate School
of the University of Notre Dame
in Partial Fulfillment of the Requirements
for the Degree of

Doctor of Philosophy

in

Aerospace Engineering

by

Chan Yong Schuele, M.S.

Thomas C. Corke, Director

Graduate Program in Aerospace and Mechanical Engineering
Notre Dame, Indiana

September 2011

CONTROL OF STATIONARY CROSSFLOW MODES
USING PASSIVE PATTERNED ROUGHNESS AND DBD PLASMA
ACTUATORS AT MACH 3.5

Abstract

by

Chan Yong Schuele

CONTENTS

FIGURES	5
SYMBOLS	12
CHAPTER 1: INTRODUCTION	1
1.1 Motivation	1
1.2 Background	3
1.2.1 Overview Laminar-Turbulent Transition	3
1.2.2 The Crossflow Dominated Laminar-Turbulent Transition in Detail	4
1.2.2.1 Crossflow Basics	4
1.2.2.2 Excitation of Defined Cross-flow Wavenumbers	5
1.2.2.3 Crossflow Experiments in Supersonic Boundary Layers	7
1.2.3 Swept Wing vs. Cone	9
1.2.4 Transition Experiments with Cones	10
1.2.5 Choice of Windtunnel	12
1.2.6 DBD Plasma Bumps	13
1.3 Objective	14
CHAPTER 2: EXPERIMENTAL SETUP	16
2.1 Windtunnel	16
2.2 Cone	17
2.3 Traverse	19
2.3.1 Calibration Procedure and Estimation of Uncertainty for the LVDT Sensor	22
2.3.2 Offset Estimation Procedure	25
2.3.3 Pitot Probe	25
2.4 Data Acquisition	26
2.5 Numerical Stability Analysis	26
2.6 Disturbance Generators	28
2.6.1 Mechanical Dimples	28

2.6.2	Plasma Disturbance Generators	30
2.6.2.1	Individual Circular Plasma Dots	30
2.6.2.2	Serrated Edge / Comb actuator	31
2.6.2.3	Vapor Deposition	32
2.6.2.4	Kapton Film Actuator	34
2.6.2.5	Dielectric Cone Actuator	37
2.6.3	Surface Roughness Characterization of the Cone Tips . . .	40
CHAPTER 3: DBD Plasma Roughness Array Evaluation		43
3.1	Circular Plasma Dots	43
3.2	Serrated edge actuator	47
CHAPTER 4: MEASUREMENTS WITH THE DISTRIBUTED ROUGHNESS CONE TIPS		55
4.1	Surface Flow Visualization	55
4.2	Pitot Tube Surveys	58
4.2.1	Receptivity to Forcing Wavenumber	58
4.2.2	Cross Flow Vortex Path	62
4.2.3	Detailed Wavenumber Analysis	65
4.2.4	Repeatability	67
4.3	Transition Front Detection	70
CHAPTER 5: MEASUREMENTS DBD PLASMA ROUGHNESS CONE TIP		81
5.1	Pitot Tube Surveys: Receptivity to Forcing Wavenumber	81
5.2	Repeatability	86
5.3	Initial Amplitudes	87
5.4	Comparison with the Dimple Cone Tips	91
CHAPTER 6: CONCLUSIONS		93
6.1	Disturbance Generators	94
6.2	Receptivity	94
6.3	Transition	96
CHAPTER 7: RECOMMENDATIONS FOR FUTURE WORK		97
CHAPTER 8: APPENDIX		100
8.1	Experimental DBD Plasma Body Force Study in Sub-Atmospheric Pressure	100
8.1.1	Experimental Setup	101
8.1.2	Actuator Measurements	102

BIBLIOGRAPHY 111

FIGURES

1.1	Schematic of cross flow, adapted from White [34].	5
1.2	Streamwise velocity contours of regularly forced cross flow vortices with 12 mm in low speed flow are shown on the left hand side. The right hand side shows the equivalent location with natural roughness. Picture taken from Saric [25].	7
1.3	Naphthalene flow visualization on a 45° sweep wing at a chord reynolds number of $Re_c = 2.4 \times 10^6$. Left hand side shows natural roughness case and left hand side shows subcritical forcing with 8 mm spacing and 6 μm height bumps. Flow is from left to right. Well visible is the delayed transition to turbulence and a regular 8 mm pattern of CF vortices on the right hand side picture [26].	8
1.4	Infrared thermographic images of a 30° swept wing at $Ma = 1.85$ under a F15 jet comparing subcritical forcing to natural roughness as found in [27]. The flow is moving from right ro left. Dark regions show lower temperature than brighter regions.	9
1.5	Cross flow Reynolds number contours on the 7° half angle cone at 4.2° angle of attack. The black lines represent inviscid surface streamlines.	11
1.6	12
2.1	NASA Langley SLDT windtunnel. View on testsection and the bleed system [4].	17
2.2	Cross section of the NASA Langley Mach 3.5 SLDT axisymmetric nozzle. The picture is showing the quiet test core and its constraints due to radiated noise.	18
2.3	Schlieren image of the cone model inside the quiet core of the supersonic nozzle at Mach 3.5. Bleed valves are open and Gø”rtler vortices are present. The quiet core is free of shocks.	19

2.4	Cross section of the 7° half angle cone with dimensions including the mounted removable cone tip. The drawing does not include the axial mounting sting	20
2.5	Traverse seen from the side.	21
2.6	The tip of the traverse arm: Removable wedge with Pitot tube and LVDT sensor for positioning.	22
2.7	LVDT displacement sensor for the wall normal motion of the wedge and Pitot tube.	22
2.8	Schematic of the optical rotary encoder RIK 2C 64/2048 L1-W3 from Numerik Jena.	23
2.9	Calibration curve for the LVDT sensor.	24
2.10	Rays of constant azimuthal angle on the cone.	27
2.11	Growth rates and N-factors for axial rays at constant azimuthal angle θ obtained from Balakumar's linear stability calculations.	28
2.12	Pictures of the $m = 45$ cone tip and magnified views on the $m = 45$ and $m = 68$ dimples including the topography across the dimples.	29
2.13	Schematic drawing of a single plasma dot actuator arrangement including the induced flow direction.	32
2.14	Left hand side: Schematic of the streamwise vorticity generator as used by Saric and Corke in 2001 to excite stationary cross flow modes. Right hand side: Drawing of the comb actuator geometry as used in the current supersonic experiments. λ is the wavelength of the desired stationary mode, either $m=45$ ($218 \mu\text{m}$) or $m = 68$ ($144 \mu\text{m}$). $h = \lambda$ and $w = \lambda/2$	33
2.15	Enlarged image of the exposed electrode after lift off. Each dot has a diameter of 0.003 in and is spaced approximately 0.006 in apart. The substrate is a 0.5 mil thick Kapton film.	35
2.16	0.5 mil thick Kapton actuator glued to a Torlon carrier cone. Right hand side picture shows the operating plasma dots at 3 inHg ambient pressure with 2.2 kVpp and 3 kHz sin-wave HV	36
2.17	Drawing of the Macor/Aluminum cone tip showing the cross section.	38
2.18	5 mil diameter Plasma Dots with $m=45$ spacing on a Macor dielectric cone tip	40

2.19	Image (a) shows the serrated edge design on the Macor plasma tip. The pattern corresponds to a m=45 roughness tip. (b) is the magnified view of a m=68 plasma roughness tip with a Keyence Model VHX-600 3-D Imaging Microscope, and (c) is a high resolution optical image of four single "fingers" of image (b)	41
2.20	The images show the plasma pattern that forms around the edges of the exposed electrode on the dielectric cone. A voltage of 5 kVpp in 3 inHg ambient pressure with a sine AC signal of 5 kHz is applied. Concentrations of plasma are formed around the tips of the "fingers" of the serrated edge. Additionally a two dimensional plasma sheet can be seen.	42
3.1	Modeling of the circular plasma actuator in Comsol. D is the dielectric thickness, r is the radius of the circular dot and t is the thickness of the electrode. A parametric sweep of $\frac{r}{D}$ from 0.12 to 3 is done. $\frac{t}{D}$ stays constant and is 4×10^{-4}	44
3.2	Surface plots of the normalized potential U/U_0 for $r/D=0.56$, $r/D=1.56$ and the limit case of the standard straight edge arrangement ($r \rightarrow \infty$) for mesh A.	46
3.3	Comparison of the unit electrical field norm E^* with the unit $\frac{V/V}{in/in}$ along the dielectric surface for mesh A.	47
3.4	Schematic drawing of the 8x magnified m=45 equivalent serrated edge actuator. Included is a picture with plasma at atmospheric pressure, 24 kVpp and 5 kHz sine waves. On the right hand side is a picture of the actual m=45 Macor cone tip running at an ambient pressure of 3 inHg and 5 kVpp at 5 kHz sine waves	48
3.5	Drawing of the PIV light sheet and camera arrangement relative to the exposed serrated edge electrode	49
3.6	Velocity magnitude of the first plane at x=0 cm of v and w including streamlines.	50
3.7	Velocity magnitude of v and w in the z-plane at z=0.85 cm. This plane was interpolated from a series of 26 x-planes (see figure 3.6) starting at x = 0 cm and ending at x = 0.35 cm	51
3.8	Drawing of the PIV light sheet and camera arrangement relative to the exposed serrated edge electrode	52
3.9	z-Vorticity of the serrated edge arrangement. The z-plane is positioned about 0.2 cm downstream of the actuator edge.	54

4.1	Surface Flow Visualization at different unit Reynolds numbers and flow conditions at Mach 3.5. $p_0 = 25psi \equiv Re = 9.45 \times 10^6 m^{-1}$, $p_0 = 35psi \equiv Re = 1.32 \times 10^7 m^{-1}$, $p_0 = 42psi \equiv Re = 1.59 \times 10^7 m^{-1}$ and $p_0 = 50psi \equiv Re = 1.89 \times 10^7 m^{-1}$	57
4.2	Schematic drawing of the cone showing the axial and azimuthal coordinates	59
4.3	Azimuthal scan at 0.0015 in above the surface and $x=11.2$ in with the $m = 0$ tip. Shown at the top is the high pass filtered Pitot probe pressure normalized by its maximum. The middle figure shows the normalized power spectral density (PSD) of the scan. At the bottom of the figure, the normalized power for each frequency at differen azimuthal location is shown (wavelets).	60
4.4	Azimuthal scan at 0.0015 in above the surface and $x=11.2$ in with the $m = 68$ tip. Shown at the top is the high pass filtered Pitot probe pressure normalized by its maximum. The middle figure shows the normalized power spectral density (PSD) of the scan. At the bottom of the figure, the normalized power for each frequency at differen azimuthal location is shown (wavelets).	61
4.5	Pitot Tube scans at different axial and azimuthal locations at 0.0015 <i>in</i> above the surface for $m = 68$	62
4.6	Paths of the cross flow vortices of the $m=68$ roughness tip as measured with the Pitot tube in comparison with the surface streamlines of the baseline flow and vortex paths of the DNS calculations with a $m=40$ distributed disturbance at $x=0.5$ in obtained from Balakumar's CFD calculations [3].	63
4.7	Azimuthal scan at $x=5$ in with constant Pitot probe height of 0.05 mm (top). The figure in the center shows the normalized PSD of the Pitot probe scan for the entire domain and the region of passive forcing which is identified in the wavelet plot at the bottom. . . .	65
4.8	Comparison of the dominant wavenumbers with the $m=68$ dimple tip at 25 psia for different Reynolds numbers at 0.05 mm height above surface. There are two azimuthal ranges of the FFT. (a) and (b) correspond to the zones wind- and leeward of the previously identified parting vortex trace.	66
4.9	Repeated measurements of azimuthal pressure distributions at constant axial position. The left hand side shows the non-repeatability for the smooth tip and a well repeatable pattern for the $m = 68$ tip.	68

4.10	Pitot probe measurements at constant azimuthal angle and three different free stream unit Reynolds numbers: $Re_{25psi} = 0.25 \times 10^6 in^{-1}$, $Re_{35psi} = 0.35 \times 10^6 in^{-1}$ and $Re_{45psi} = 0.45 \times 10^6 in^{-1}$	69
4.11	Preston Probe measurements for $m = 45$ (top) and $m = 68$ (bottom) forcing at $Ma = 3.5$ and a freestream unit Reynolds number of $0.45 \times 10^6 in^{-1}$. The heights correspond to the normalized total pressure at the probe tip.	71
4.12	RMS values for constant Reynolds numbers from figure 4.11.	72
4.13	Preston probe method showing sharp rise in measured total pressure with increasing free stream Reynolds number at location of transition onset. The measurements were taken in the NASA Mach 3.5 SLDT with $T_0 = 100$ F. Figure is taken from [18].	74
4.14	Straightened Preston probe scans showing the normalized total pressures and paths of the analyzed pressure traces for the detection of laminar-turbulent transition. $p_0 = 45$ psi	75
4.15	$m=45$ normalized pressure traces parallel to the cross flow vortex structure. The traces are azimuthally centered in the middle between the two visible pressure maxima. They are shown for every 0.5° and cover approximately 6° from 105° to 111° in azimuthal direction. The angles refer to the initial angle where the measurement was started for each trace. The dashed red line is a linear curve fitted to the slope of the pressure signal before it levels out. The intersection with the $p_t/p_0 = 0.022$ is defined as laminar turbulent transition onset.	76
4.16	$m = 68$ normalized pressure traces parallel to the cross flow vortex structure. There are two low pressure regions (a) and (b) for which the transition Reynolds number Re_{tr} is estimated. The angles correspond to the initial angle where the measurement of the traces was started.	77
4.17	Shown are the laminar-turbulent transition locations for the $m = 45$ and $m = 68$ distributed roughness tips including error bars. The black circular dots (a) and (b) correspond to the traces in figure 4.14 with $m = 68$ forcing. The blue dot corresponds to the location identified in figure 4.15 with $m = 45$ forcing.	78

4.18	The top figure is adapted from King [18] and shows the qualitative shape of the transition front. Added to that is the shape of the transition front based on Balakumar's linear stability analysis [3]. A N-factor of 11 is assumed at the onset of laminar turbulent transition. The bottom figure shows the results of the Preston probe measurements including curves of constant N-factors which pass through the location of the measured onset of transition to turbulence. These correspond to $N \approx 6$ for $m = 45$ and $N \approx 9$ for $m = 68$	80
5.1	Pitot probe traces at 0.027 mm height above the surface for multiple axial locations at 25 psia and $T_0 = 100$ F with the m=45 DBD plasma cone tip. Also shown are the vortex traces with plasma on and off as dashed lines. The blue area corresponds to the zone where forcing at 0.5 in has no influence (from figure 4.6.)	82
5.2	Pitot probe traces at 0.04 mm height above the surface for multiple axial locations at 25 psia and $T_0 = 100$ F with the m=68 DBD plasma cone tip. Also shown are the vortex traces with plasma on and off as dashed lines. The blue area corresponds to the zone where forcing at 0.5 in has no influence (from figure 4.6.)	83
5.3	Shown are azimuthal pitot probe scans at constant height and $Re_x = 1.5 \times 10^6$ on the $m = 45$ DBD plasma cone tip. The white area in the top plot corresponds to the range of azimuthal angles where the FFT analysis of the bottom plot is done.	85
5.4	Shown are azimuthal pitot probe scans at constant height and $Re_x = 1.5 \times 10^6$ on the m=68 DBD plasma cone tip. The white area in the top plot corresponds to the range of azimuthal angles where the FFT analysis of the bottom plot is done.	86
5.5	Shown are azimuthal pitot probe scans at constant height and $Re_x = 1.75 \times 10^6$ on the m=45 DBD plasma cone tip. The white area in the top plot corresponds to the range of azimuthal angles where the FFT analysis of the bottom plot is done.	87
5.6	Shown are azimuthal pitot probe scans at constant height and $Re_x = 1.75 \times 10^6$ on the m=45 DBD plasma cone tip. The white area in the top plot corresponds to the range of azimuthal angles where the FFT analysis of the bottom plot is done.	88
5.7	Repeated azimuthal pressure scans with plasma on before and after a wind tunnel restart. m=68, $p_0 = 25$ psi, $T_0 = 100$ F, $Re_x=2,000,000$	89

5.8	Repeated azimuthal pressure scans with AC driving frequencies from 1 kHz to 6 kHz and different voltages. $m=68$, $Re_x = 2 \times 10^6$, $p_0 = 25$ psi, $T_0 = 100$ F	90
8.1	Teflon plasma actuator on the shielded force balance inside the vacuum vessel.	101
8.2	Comparison of thrust measurements inside and outside the vacuum vessel.	102
8.3	Influence of different ambient pressures on the voltage vs. thrust curves. 2kHz ramps.	103
8.4	Influence of different ambient pressures on the voltage vs. thrust curves. 2kHz ramps.	104
8.5	Maximum thrust values in dependence of ambient pressure for different AC driving frequencies.	105
8.6	Dependence of thrust at constant applied voltage on ambient pressure.	106
8.7	Necessary applied voltage to maintain constant body force for different ambient pressures.	107
8.8	Necessary applied voltage to maintain constant body force for different ambient pressures.	108
8.9	Thrust measurements for a 1/4 in thick Teflon dielectric with 1 in and 2 in wide covered electrodes at different ambient pressures.	109
8.10	Thrust measurements for a 1/8 in thick Macor dielectric with 1 in and 2 in wide covered electrodes at constant pressures and different AC driving frequencies.	110

SYMBOLS

CF	Abbreviation for Cross Flow
Re	Reynolds number or unit Reynolds number
m	Wavenumber based on $1/360^\circ$
Ma	Mach number
α	Angle of Attack
θ	Cone Half Angle
$()_0, ()_{stag}$	Stagnation condition
$()_t$	Total condition
$()_{tr}$	Transition

CHAPTER 1

INTRODUCTION

1.1 Motivation

The development of commercial supersonic aircraft has been pursued for several decades. After the start of the Concorde program in 1969 and its end in 2003, no other newly developed commercial supersonic airplane became operational although planes like the Tu144 or Boeing's B2707 were developed [14]. There are multiple challenges that still need to be overcome. As summarized by Coen [10], these are the supersonic cruise efficiency, and the need for light weight materials with durability at high temperatures. Besides purely increasing the efficiency, environmental aspects also have to be considered. These include airport noise, sonic boom, and high altitude emissions. In the case of the Concorde, the sonic boom prevented supersonic flight over land.

Different approaches can be taken to improve the efficiency as well as to address the acoustic emissions. The sonic boom can be mitigated by modifying the shape of the aircraft's nose ("boom shaping" [12]) or adding a nose spike that generates a series of small shocks instead of one large shock ("quiet spike" [15]). However, these methods of mitigating the sonic boom increase the aerodynamic drag of the aircraft and thus decrease the efficiency.

Therefore, the efficiency needs to be maximized by minimizing the aerodynamic

drag even more, especially over the lifting surfaces which are the main contributor to the overall aerodynamic drag. As first recognized by Adolf Busemann in 1935[6], wing sweep mitigates wave drag on the aircraft or it can be completely avoided if the wing sweep is large enough to place the wings inside the Mach cone. The downside of high sweep angles is the generation of a mean cross flow and the resulting cross-flow instability that is the principle mechanism leading to laminar turbulent transition on a swept wing. It is desirable to maintain a laminar boundary layer over an as large as possible area of the wing because laminar viscous drag is considerably lower than turbulent drag [2]. Other boundary layer instabilities such as Tollmien-Schlichting waves, attachment line instabilities, and a Görtler instability can be minimized by an appropriate shaping of the wing [22] whereas the instability linked to cross flow exists whenever wing sweep exists.

An active method to limit the occurrence of cross flow instabilities is e.g. wall suction [5]. This method however requires complicated hardware that also requires high maintenance. Passive methods on the other hand as developed by Saric [28] have proven to work efficiently on swept wings and flat plates. As shown in different experiments in low subsonic speeds, the application of micron sized distributed roughness elements on swept wings [24] can be utilized to control cross flow dominated laminar-turbulent transition. Depending on the introduced wave number, the extent of laminar flow can be increased or reduced. Since this method does not require any complicated modification to the wing, it has the potential to be a practical solution to lowering viscous drag on aircraft that is commercially viable. As mentioned by Bushnell [7], reliability and maintainability are the key factors for the commercial application of laminar flow control technology.

Motivated by the significant impact of laminar turbulent transition control on

supersonic aircraft efficiency, the simple yet highly effective passive roughness element approach is further studied in supersonic flows. Its applicability is also extended by the development of active plasma bumps which allow for the dynamic adaption to changing flight conditions, e.g. during climbing and descend of a mission. This is a very important step towards the design of a practical flow control device for highly efficient future supersonic aircraft.

1.2 Background

1.2.1 Overview Laminar-Turbulent Transition

Generally the transition from laminar to turbulent flow undergoes several stages. It starts with external disturbances like freestream vorticity, freestream sound, freestream entropy spots, surface roughness or vibrations and is then internalized by a process called receptivity¹. Disturbances are initially damped until they reach the point of neutral amplification. Growth of the disturbances takes then place downstream of the point of the so called branch I of stability. Depending on the initial amplitudes either linear theory can be used to describe instability growth or in case of high initial disturbances the whole linear regime can be bypassed and only the nonlinear stage including secondary and tertiary modes will develop before transition to turbulence. If the initial amplitudes are somewhere in between so called transient growth can occur.

Modes of linear amplification in a boundary layer include viscous instabilities like

¹A few descriptions of the term receptivity found in [5]: "... the mechanisms leading to the entrainment of external disturbances into the boundary layer and to the generation of instabilities with initial amplitudes dependent on the external disturbances" or in [1]: "receptivity describes the birth of a disturbance, whereas sensitivity is a concept of larger breath, describing the modification incurred by the state of a system as a response to parametric variations." and in [17]: "Receptivity describes processes by means of which instability waves appear in boundary layers under the action of some external perturbation of various physical sources."

the Tollmien Schlichting waves, inflectional or inviscid instabilities like cross flow instabilities which will be the main interest of this work, adverse pressure gradient or oblique first-mode waves at supersonic Mach numbers, Second or Mack modes for hypersonic flows ($Ma_\infty > 5$) and Görtler vortices for curved streamlines. The nonlinear stage generally develops over a much shorter region than the linear growth regime.

1.2.2 The Crossflow Dominated Laminar-Turbulent Transition in Detail

1.2.2.1 Crossflow Basics

Cross flow instability is a property of three-dimensional boundary layer flows. It appears wherever in plane curved streamlines occur e.g. like on swept wings and swept cylinders, cones at angle of attack, and rotating discs. A schematic of the cross flow in a boundary layer is shown in figure 1.1. Curved streamlines generate centrifugal forces which are balanced by radial pressure gradients. Since pressure is assumed to be constant in wall normal direction within a boundary layer, the excess of pressure due to its radial gradient at the boundary layer edge will generate cross flow. The noslip condition leads to zero cross flow velocity at the wall. At the same time the cross flow component is also zero at the edge of the boundary layer and leads thus to an inflectional velocity profile which fulfils the necessary and sufficient condition for instability according to Tollmien.

The first stage of cross flow instability dominated transition starts with the process of receptivity. The free stream turbulence level defines if travelling or stationary modes will dominate the transition process. Although travelling cross flow waves are more amplified than stationary cross flow modes as based on linear theory, stationary modes are exposed to larger initial amplitudes in low turbulence en-

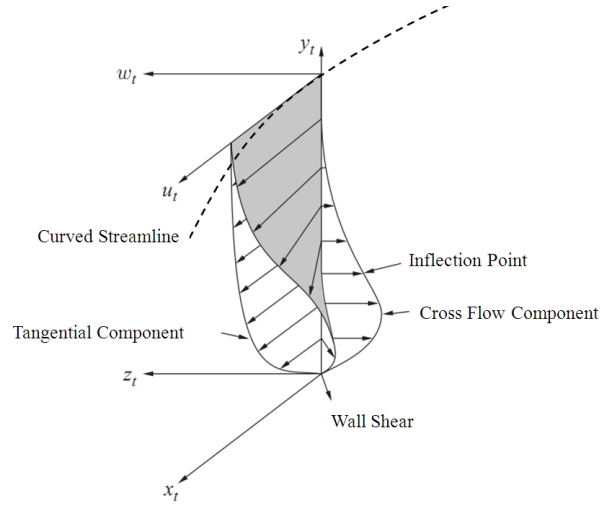


Figure 1.1. Schematic of cross flow, adapted from White [34].

vironments as can be found in free flight. Due to their approximate alignment with the inviscid streamlines of the baseline flow, they have a strong integrated effect on the boundary layer and dominate the laminar-turbulent transition process. Deyhle and Bippes measured a background turbulence level of up to 0.2% until travelling modes were the leading laminar-turbulent transition mechanism over stationary modes.

The stationary cross flow mode forms co-rotating vortices and grows initially linearly up to an amplitude between 10% and 30% [9], [34] where nonlinear saturation of the vortices sets in. At some point of the nonlinear saturation stage, secondary high frequency disturbances develop and lead quickly to turbulent breakdown.

1.2.2.2 Excitation of Defined Cross-flow Wavenumbers

Stationary cross flow vortices are highly receptive to 3-D surface roughness. Saric exploited this property to excite stationary cross flow modes with arrays of

circular micron sized distributed roughness elements. He showed that exclusively the forced wavenumber and superharmonics of it appeared in the boundary layer. All other wavenumber cross flow vortices were completely suppressed. This led to the idea of forcing a weakly amplified stationary cross flow instability which grows at first and decays then completely. If the wavenumber of this forced mode is larger than the naturally most amplified, no superharmonics feed into the growth of the most amplified wavenumber and laminar-turbulent transition is delayed. It is the initial amplitude of the cross flow disturbance originating from surface roughness which decides over the dominant wavenumber. Saric called forcing with a wavenumber larger than the most amplified subcritical forcing, whereas forcing with a wavenumber equal to the naturally most amplified wavenumber critical forcing. U-velocity pitot probe scans of the stationary cross flow instability in the boundary layer of a swept wing at $Re_c = 3 \times 10^6$ without and with forcing are shown in figure 1.2. It can be clearly seen that the initially random distribution of stationary structures is replaced by equally spaced cross flow vortices in case of regular roughness element forcing.

His experiments on swept wing models in free flight and low speed wind tunnel tests showed that the wavelength to roughness array element diameter needs to be at least 0.5 to excite the targeted mode. He was able to delay laminar-turbulent transition from 60 % to 80 % chord with subcritical forcing on a swept wing at $Re_{chord} = 2.4 \times 10^6$ and to move the location of transition slightly upstream by forcing with the critical wavenumber[24]. The effect on the laminar-turbulent transition location is shown with the help of Naphthalene flow visualizations in figure 1.3. Naphthalene sublimates faster in regions of higher surface shear stress which means that in the locations where large areas of the white streaky struc-

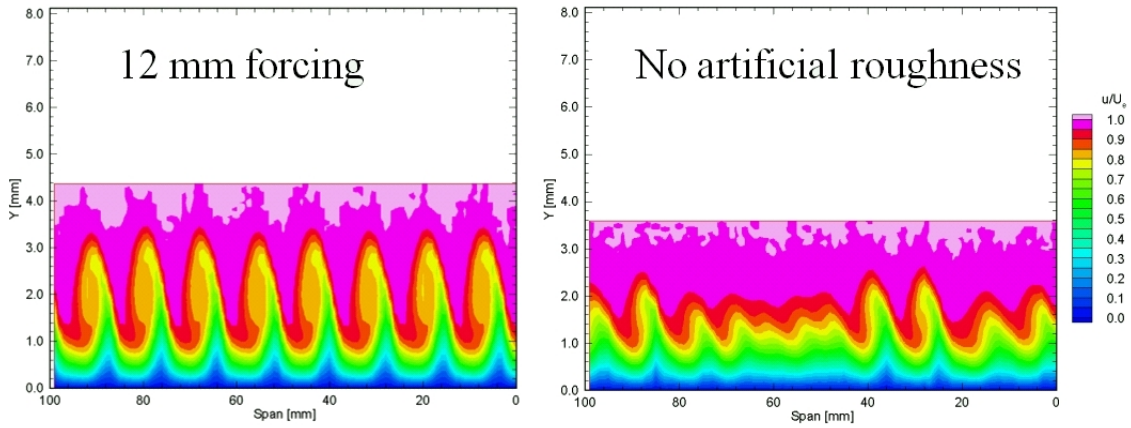


Figure 1.2. Streamwise velocity contours of regularly forced cross flow vortices with 12 mm in low speed flow are shown on the left hand side. The right hand side shows the equivalent location with natural roughness. Picture taken from Saric [25].

tures disappear, higher surface shear stress as e.g. in turbulent boundary layers are present. The onset of Naphthalene free regions are identified as location of laminar-turbulent transition onset.

Interestingly, the initial height of the roughness elements in the range from 6 to 48 μm had only a weak effect on the saturation amplitudes and the onset of laminar-turbulent transition[24]. The roughness heights were in the range . Additionally, no effect of free stream acoustics and 2-D roughness could be found on the formation of stationary cross flow vortices.

1.2.2.3 Crossflow Experiments in Supersonic Boundary Layers

Most of the experiments with detailed boundary layer measurements in cross flow dominated laminar-turbulent transition were done at subsonic low Mach number flows. Only two authors, Saric [22], [27] and Semionov [31], investigated the

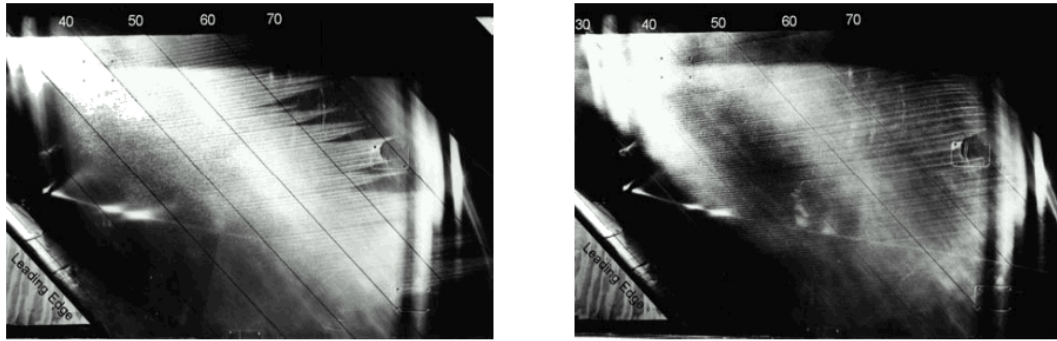


Figure 1.3. Naphtalene flow visualization on a 45° sweep wing at a chord reynolds number of $Re_c = 2.4 \times 10^6$. Left hand side shows natural roughness case and left hand side shows subcritical forcing with 8 mm spacing and $6 \mu\text{m}$ height bumps. Flow is from left to right. Well visible is the delayed transition to turbulence and a regular 8 mm pattern of CF vortices on the right hand side picture [26].

effect of distributed roughness elements on the location of laminar-turbulent transition under supersonic free stream conditions on swept surfaces.

Saric's & Reed's swept wing was in a Mach 2.4 flow with a subsonic leading edge. By choosing a subcritical wavenumber for their micron sized leading edge roughness array made of dimples or bumps, they could delay transition to 80% of the chord, beyond the pressure minimum. If the Reynold number was slightly increased, the transition location went back to 50% chord length although the method of subcritical forcing should work for a range of wavenumbers around the most amplified.

In 2004 they mounted a swept wing with applied roughness elements under the body of a F15 jet and with the help of infrared thermography they showed some transition delay over a very limited span towards the tip of the test wing as shown in figure 1.4. They mention that this limited effect on laminar-turbulent transition might have been an effect of flow interference from the body of the aircraft.

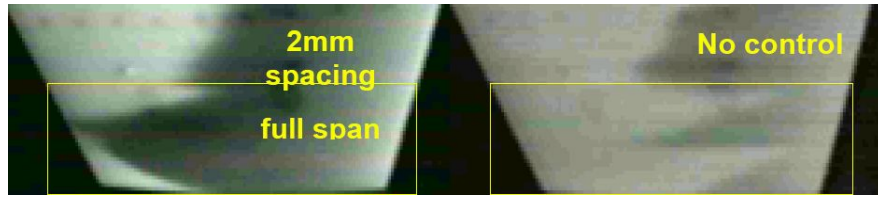


Figure 1.4. Infrared thermographic images of a 30° swept wing at $Ma = 1.85$ under a F15 jet comparing subcritical forcing to natural roughness as found in [27]. The flow is moving from right to left. Dark regions show lower temperature than brighter regions.

Semionov in 2006 and 2008 ran measurements on a Mach 2, 40° swept wing in combination with an array of $6 \mu\text{m}$ distributed roughness elements. The flow shows some response to the roughness elements. However in contrast to be expected from Saric's observations [28], transition seemed to be slightly delayed when the roughness elements were spaced at the most amplified wavenumber. In addition there was no information given about the background disturbance levels of the wind tunnel which is crucial to estimate what kind of instabilities might be excited on the swept wing model.

The experiments done so far on turbulent transition delay with micron sized roughness elements in supersonic flow show not completely conclusive data on the transition location. It is therefore necessary to collect more data in order to prove that subcritical forcing in supersonic free stream flow delays the onset of laminar-turbulent transition.

1.2.3 Swept Wing vs. Cone

Although the target application is a swept wing, the flow around a sharp cone will be the subject of experimentation. The conical flow at incidence generates a

streamline-normal pressure gradient which, if properly chosen, can lead to cross flow dominated transition. The basic transition mechanism is therefore identical between the swept wing and the cone which is sufficient for a proof of concept experiment.

Cones have a distinct advantage over infinite swept wings when tested in supersonic windtunnels with limited diameter test sections. In order to experimentally establish cross flow induced transition on a swept wing or a flat plate respectively, either displacement bodies and contoured walls [13] or contoured walls [34] have to be added. They are needed to establish infinite wing conditions and a favorable pressure gradient to suppress the growth of TS-waves. These additional bodies in a supersonic flow will cause Mach waves radiating into the test section which increase the overall disturbance level. A cone on the other hand fits more easily completely inside the constant Mach number core of the test section without being exposed to contamination based on finite model dimensions, which guarantees complete exposure to the undisturbed free stream flow conditions.

1.2.4 Transition Experiments with Cones

Transition experiments on cones in supersonic flows at angle of attack have been done for the last several decades. A comprehensive summary is given by Schneider [30].

Generally can be said that the cross flow instability activity is maximized where the largest cross flow Reynold number is expected. For a cone at angle of attack, the cross flow Reynolds number increases and then decays moving from the windward towards the leeward side with its maximum towards the leeward side

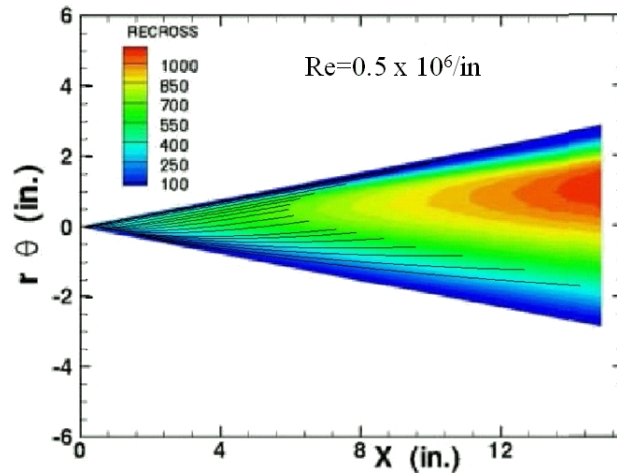


Figure 1.5. Cross flow Reynolds number contours on the 7° half angle cone at 4.2° angle of attack. The black lines represent inviscid surface streamlines.

at about 130° as shown in figure 1.5 from Balakumar's computations [3]. The boundary layer profiles of u-velocity at constant axial location for different azimuthal angles are shown in figure 1.6. They show a thickening of the boundary layer from the windward towards the leeward side. The leeward ray at 180° is where the flow from both sides meet and a relatively thick boundary layer with an inflectional profile is formed. The inflectional boundary layer profile can be seen in figure 1.6 for $\theta = 180^\circ$.

Therefore three different types of instability mechanisms can be observed on the cone at angle of attack: Viscous/First modes on the windward side, three dimensional CF modes on the sides and Inviscid/Inflectional instabilities on the leeward side. The amplification rates of first modes on the windward side are usually much smaller than for the CF instabilities and the leeward side inflectional boundary layer inviscid instabilities. This has been shown in transition experiments [18] as well as N-factor calculations [3].

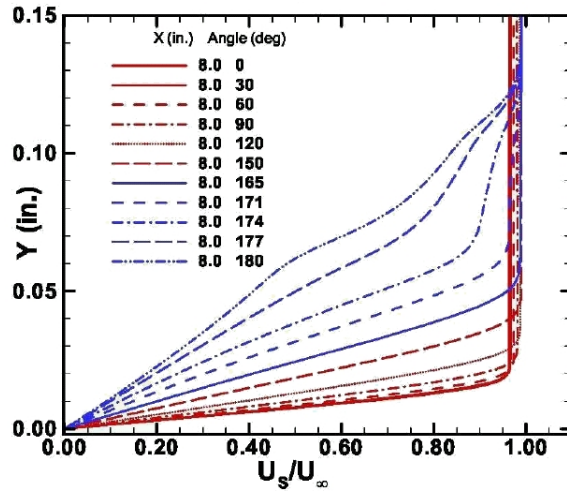


Figure 1.6.

If the ratio of angle of attack (α) and cone half angle (θ) are chosen properly, CF modes will be the dominating transition mechanism over the majority of the surface. King [18] demonstrated that stationary cross flow vortices are visible in the range of $\frac{\alpha}{\theta} = 0.4$ to 0.8 in the NASA Mach 3.5 SLDT quiet tunnel.

No experiments with micron sized distributed roughness elements or DBD plasma actuators for the purpose of laminar-turbulent transition delay exist up to date for cones at angle of attack in supersonic flow.

1.2.5 Choice of Windtunnel

As explained in the chapters before, the initial free stream disturbances dictate if stationary or travelling instabilities will dominate in the laminar-turbulent transition process. The future application of the investigated forcing mechanism will be on supersonic aircraft in atmospheric high altitude flight where low free stream disturbance backgrounds are expected. The NASA Mach 3.5 SLDT wind

tunnel which is used for the conducted experiments, is equipped with boundary layer bleed slots which allow for a low disturbance constant Mach number core with a turbulence level of less than 0.05%. As shown in King's cone measurements, this suffices for stationary cross flow vortices to be the principal laminar-turbulent transition mechanism. Other supersonic wind tunnels without special precautions to keep the supersonic nozzle wall laminar exhibit significantly higher background disturbance levels and do not relate to relevant free flight conditions.

1.2.6 DBD Plasma Bumps

As part of the experiments, an array of DBD plasma actuators will be used as equivalent replacement for the micron sized roughness array. DBD plasma actuators are active flow control devices which use a non-thermal plasma to assert a body force on neutral air molecules. The great advantage of DBD plasma actuators is that they have a high frequency response and do not require any mechanically movable parts. Additionally they can be mounted flush with the surface which is especially important for an application that is highly sensitive to 3-D surface roughness.

Plasma actuators have been used in several active flow control scenarios over a wide range of Reynolds numbers. These range from separation control on airfoils and bluff bodies to the forcing of viscous instabilities like TS waves. A review of the DBD plasma actuator and its applications can be found in [11].

An isolated roughness element generates a horseshoe vortex which wraps around the base of the roughness element and moves downstream into the direction of the flow. The two arms of the entrained vortices are counter rotating and generate a local thinning and thickening of the boundary layer due to the entrainment

of fluid normal to the wall. If an array of roughness elements is used, a periodic thinning and thickening of the boundary layer can be generated which corresponds to the generation of positive and negative vorticity. The same effect needs to be achieved with a DBD plasma actuator array. Standard electrode geometries used for that purpose are plasma synthetic jets[21] or streamwise vortex generator arrangements[32]. In 2001 Corke and Saric were able to show receptivity of a low speed swept wing boundary layer to the streamwise vortex generator arrangement. The induced velocity of thin dielectric plasma actuators is in the range of a couple m/s . This might appear small compared to a free stream Mach number of 3.5 but nonetheless, the actuator generates the initial disturbance of an instability whose growth is based on linear theory and needs therefore just an infinitesimally small initial disturbance to be amplified. DNS simulations by Balakumar [3] show that the perturbation amplitude at the location of branch I is sufficient if it is just 0.5 % of the free stream velocity. In case of his simulation parameters in Mach 3.5 flow, this corresponds to about 3 m/s . This shows that an initial perturbation of just a couple meters per second or less can force the growth of stationary cross flow modes. The general forcing needs to be just strong enough to distinguish itself from the effect of natural surface roughness.

1.3 Objective

The delay of transition to turbulence on the highly swept wings of a supersonic aircraft increases the supersonic cruise efficiency. This helps to design economically and environmentally feasible civil supersonic aircraft. The overall objective of this work is therefore to show the delay of cross flow dominated laminar-turbulent transition on highly swept surfaces in a Mach 3.5 flow by means of subcritical

forcing with an array of DBD plasma actuators. DBD plasma actuators make it possible to quickly adapt to changing environmental conditions like free stream Reynolds number during changing mission plans of the aircraft which is a necessary step towards a practical application of subcritical mode forcing.

The experiments are conducted on a cone at angle of attack that is exposed to cross flow. Hence transition to turbulence is dominated by stationary cross flow modes in the same manner as on a highly swept wing if the free stream disturbance levels are as low as in the used constant Mach number core of the NASA Mach 3.5 SLDT quiet tunnel.

The following steps need to be done to show the overall objective of this work:

1. Establish that stationary cross flow instabilities are responsible for laminar turbulent transition on the used 7° half angle cone cone at 4.2° angle of attack.
2. Show that the stationary cross flow instability is receptive to the forcing wavenumber with a traditional micron sized roughness array
3. Prove that subcritical forcing delays laminar turbulent transition relative to the critical forcing case
4. Show that the stationary cross flow instability is receptive to the input wavenumber of the DBD plasma actuator array

CHAPTER 2

EXPERIMENTAL SETUP

2.1 Windtunnel

There are currently four quiet tunnels in the US which have different capabilities in terms of Mach number and Run time. The only quiet tunnel which has the capability of extended run times is the NASA Langley Mach 3.5 Supersonic Low Disturbance Tunnel (SLDT). It is designed as a blow down facility and uses dry air which is filtered for particles larger than $1 \mu m$. The tunnel exhausts to vacuum spheres, providing typical run times between 30 and 45 minutes. The stagnation pressures can be set from 5 to 175 *psia* at a free stream Mach number of 3.5. The settling chamber includes seven turbulence management screens and five sintered mesh porous plates attenuating incoming pressure fluctuations (acoustics). In order to obtain a testzone with low free stream disturbance, a specially modified 3-D axisymmetric nozzle was designed. It has a highly polished slow expansion contour to limit Görtler vortex formation on the nozzle wall. Additionally, boundary layer bleed slots are used at the nozzle throat to remove the turbulent boundary-layer which originates from the nozzle's contraction. The boundary layer bleed slots can be opened and closed by valves which are connected through a circular manifold to a vacuum reservoir. The resulting constant Mach number quiet test core length, Δx , along the centerline of the nozzle is depending on the total pressure

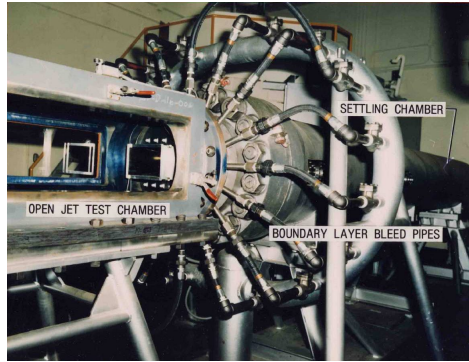


Figure 2.1. NASA Langley SLDT windtunnel. View on testsection and the bleed system [4].

p_0 . The cross section of the 3-D axisymmetric nozzle is shown in figure 2.2. Hot wire measurements along the centerline of the nozzle at $p_0 = 25$ psia and $p_0 = 50$ psia and a total temperature of $T_0 = 311$ K show that the extent of the quiet core is $\Delta x = 14$ in and $\Delta x = 11$ in respectively. The quiet core length becomes smaller due to the more upstream transition to turbulence of the nozzle wall boundary layer at higher free stream Reynolds numbers. Typical pressure fluctuations in the quiet zone are lower than 0.05% of the free stream static pressure [16]. With open bleed valves the existence of Görtler vortices originating from the inside nozzle wall can be seen (Figure 2.3), proving that the boundary layer on the expanding nozzle is laminar and the quiet core is free of shocks.

2.2 Cone

The cone-model used in the experiments is a hollow, thin-skinned right circular cone with a 7° half angle. It has a total length of 14 in or 35.56 cm and consists of 15-5ph stainless steel which is precipitation hardened to a H-1050 surface hardness and polished to a mirror finish. The wall thickness over 85% of the cone surface

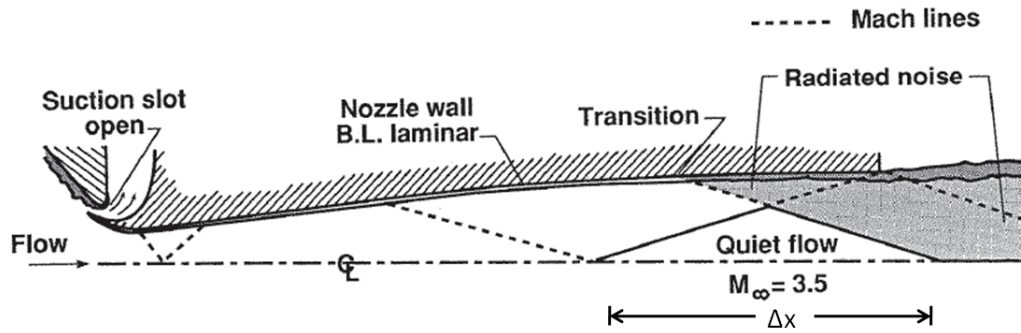


Figure 2.2. Cross section of the NASA Langley Mach 3.5 SLDT axisymmetric nozzle. The picture is showing the quiet test core and its constraints due to radiated noise.

is 0.08 in whereas the other 15% have a wall thickness of 0.03 in along a strip in flow direction. This strip contains thermocouples that are spot welded to the inner wall. On the opposite side of the thermocouples 20 pressure taps with a diameter of 0.03 in are installed. They are spaced 0.55 in apart and start 2.15 in downstream of the cone tip [8]. The maximum variation in the cone radius per inch downstream is 0.0002 in or 0.005 mm, corresponding to 1% of the minimum boundary layer thickness [19]. The base of the cone is mounted to a sting which is connected to a vertical strut on a base plate. The sharp tip of the cone is designed to be removable and threads into the front end of the cone body (See figure 2.4). In order to generate sufficient cross flow the cone is mounted at 4.2° angle of attack. The $\frac{\alpha}{\theta}$ ratio is 0.6 which is proven to cause cross flow Reynolds numbers large enough for the occurrence of cross flow dominated transition [18].

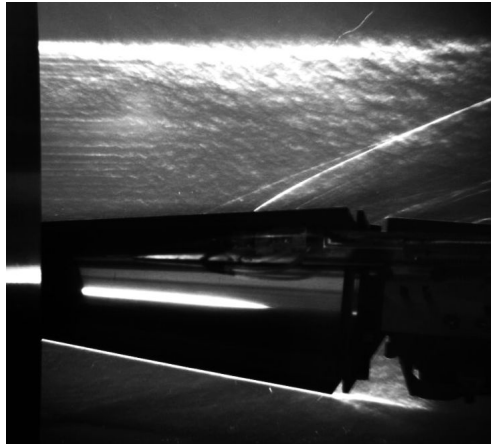


Figure 2.3. Schlieren image of the cone model inside the quiet core of the supersonic nozzle at Mach 3.5. Bleed valves are open and Görtler vortices are present. The quiet core is free of shocks.

2.3 Traverse

The traverse can move in wall normal, axial and azimuthal direction. The whole mechanism is coaxially mounted with sleeve brass bearings to the sting of the cone. A stepper motor with gear box on the traverse turns itself and the traverse around the sting. It is marked as "Azimuthal Motion" in figure 2.5. The arm which is carrying the pitot tube is mounted on a linear slide and can be moved with another stepper motor in axial direction (See figure 2.5). The tip of this arm is connected with a hinge pin to a steel connector piece which holds a sensor for the estimation of its wall normal position. The pitot tube is integrated into a steel wedge which can be mounted with a screw on the connector piece (See figure 2.6). Because the tip of the traverse arm can rotate around the hinge pin, a screw is used to push or pull it in axial direction right above the center of rotation. By doing so, the height above the cone surface can be controlled. This screw is connected to another stepper motor with gear box which is mounted at

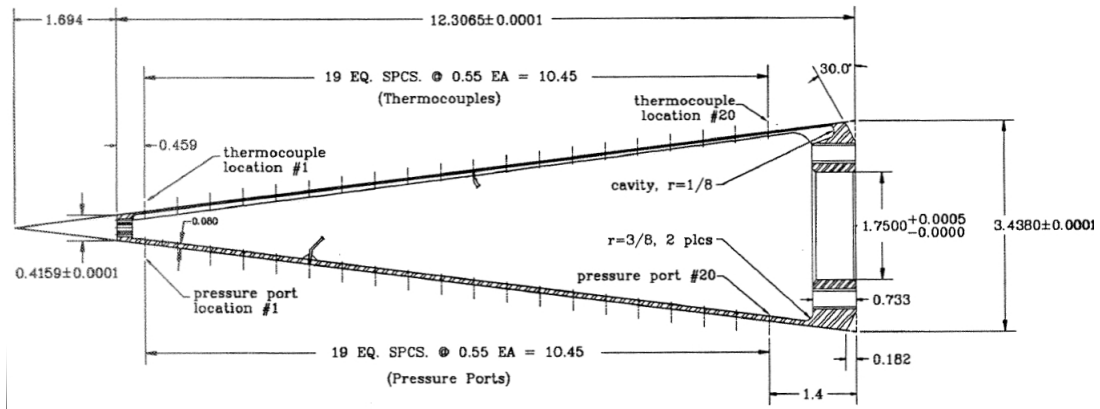


Figure 2.4. Cross section of the 7° half angle cone with dimensions including the mounted removable cone tip. The drawing does not include the axial mounting sting

the rear end of the traverse arm.

The traverse is also equipped with a rotary encoder made by Numerik Jena¹ to detect the accurate azimuthal position (See figures 2.8 and 2.5). It is based on an optical disk with 2056 lines which is read by an encoder including a 5x interpolation electronics which generates a RS255 output signal. The resolution is 0.036° .

The wall normal position of the pitot tube is measured with a differential variable reluctance sensor² (DVRT) or also known as half bridge linear variable displacement sensor (LVDT) which detects the relative rotation between the traverse arm and the wedge. The DVRT is a miniature version of a standard DVRT displacement sensor. It consists of a 1.8 mm outer diameter cylindrical sensor body and a 0.8 mm outer diameter titanium sliding core. A picture of the LVDT sensor is shown in figure 2.7. The sliding core is attached to the rotatable wedge

¹Numerik Jena GmbH, D-07743 Jena

²Microminiature DVRT[®] by Microstrain Inc, Williston, VT, USA

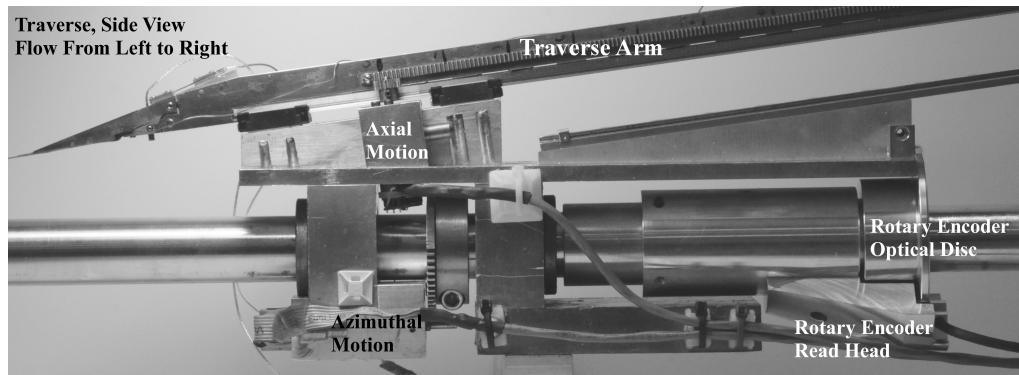


Figure 2.5. Traverse seen from the side.

and the sensor body is mounted on the traverse arm thus it detects the relative motion between the traverse arm and the rotating wedge (see figure 2.6).

The azimuthal and wall normal position sensors are used as proportional feedback sensors for the wall normal and azimuthal motion. The axial motion stepper motor on the other hand is run in an open loop without position feedback. The stepper motor is equipped with a zero backlash gear box whereas the pinion gear which moves the axial arm has a small amount of slack. Because the axial motion is facing a constant drag force by the supersonic flow during tunnel operation, the axial motion arm is being constantly pushed against the teeth of the axial motion pinion gear which removes the slack for motions up and downstream in axial direction. This means that the traverse arm will not suffer from backlash during tunnel operation, even without active position feedback.

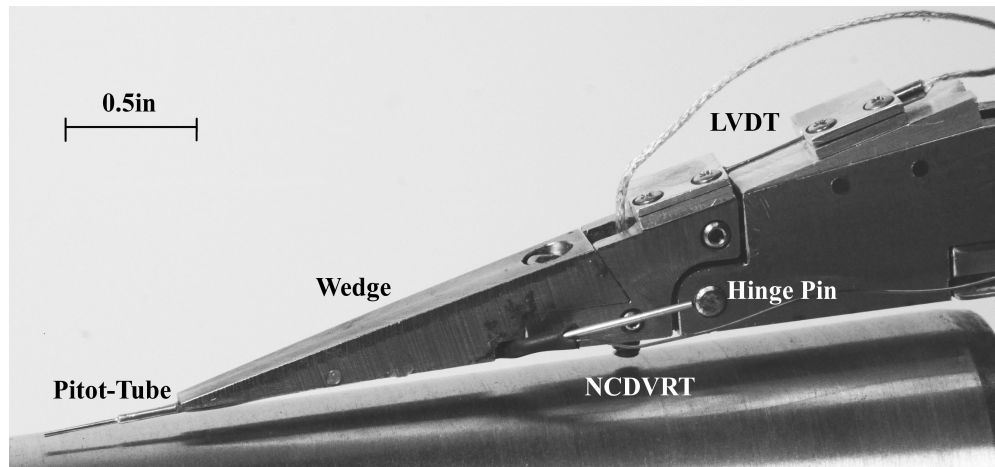


Figure 2.6. The tip of the traverse arm: Removable wedge with Pitot tube and LVDT sensor for positioning.



Figure 2.7. LVDT displacement sensor for the wall normal motion of the wedge and Pitot tube.

2.3.1 Calibration Procedure and Estimation of Uncertainty for the LVDT Sensor

A Keyence³ LS optical micrometer is used to calibrate the LVDT sensor. A 249 mm long balsa wood rod is connected to the steel connector piece at the tip of the traverse arm. The up and down motion of the tip piece is amplified and can be more easily measured during calibration. The tip of the balsa wood rod generates a shade in the measurement field of the optical micrometer which is

³Keyence Corp of America, Woodcliff Lake, NJ, USA

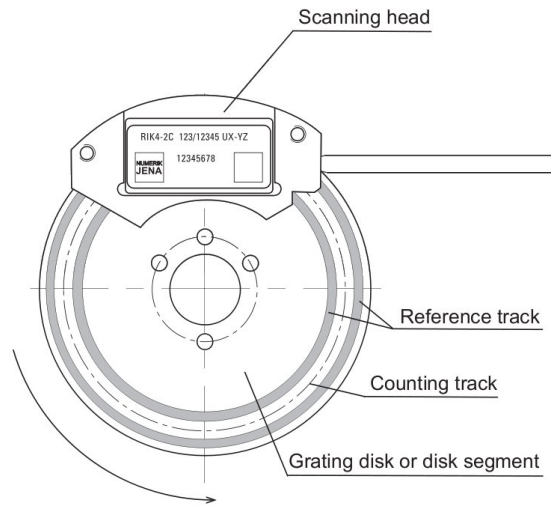


Figure 2.8. Schematic of the optical rotary encoder RIK 2C 64/2048 L1-W3 from Numerik Jena.

directly translated into an absolute position. The repeatability of the micrometer is given with $\pm 0.2 \mu\text{m}$ while the accuracy is $\pm 3 \mu\text{m}$. The calibration curves for the LVDT is shown in Figure 2.9. The second order polynomial fit of the LVDT calibration shows a 95% confidence interval of $\pm 36 \mu\text{m}$ or 0.26% of the range. The combination of the first order uncertainty from the micrometer and the calibration curve is approximately $36.1 \mu\text{m}$ at the tip of the balsa calibration arm. The resolution of the LVDT itself as given by the manufacturer as $\pm 0.3 \mu\text{m}$ with a hysteresis and repeatability of $\pm 1 \mu\text{m}$. The accuracy is $\pm 0.1\%$ of the measurement range. With this information the first order uncertainty of the LVDT sensor is calculated for the displacement measurement of the calibration arm tip. Knowing the radial distance from the hinge pin to the LVDT, the error in displacement at the calibration arm tip based on the manufacturer given values is

then $87\mu m$ ⁴. To derive the uncertainty at the Pitot probe tip, the ratio between the Pitot probe length relative to the hinge pin and the Balsa wood length is used in a similar manner as just done with the uncertainty calculation of the calibration arm displacement. The uncertainty of the pitot probe position is then $23\mu m$ or 1.8% of the wall normal motion range of 0.05 in or 1.27 mm. ⁵

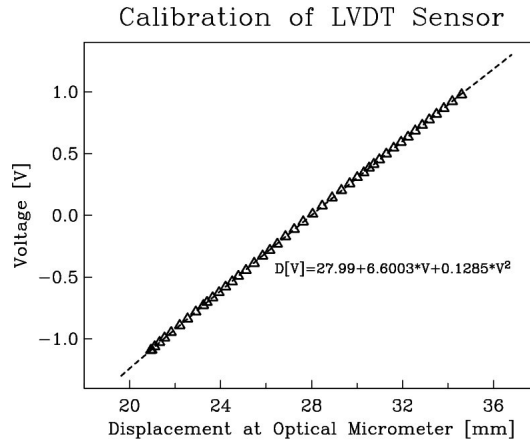


Figure 2.9. Calibration curve for the LVDT sensor.

⁴Calculated with $\Delta z_{BalsaTip} = \frac{r_{LVDT-Hinge}}{r_{BalsaTip-Hinge}} \Delta l_{LVDT}$. $r_{LVDT-Hinge} = 10.55mm$ and $r_{BalsaTip-Hinge} = 249mm$. The uncertainty in the measurements of the dimensions is 0.001 in or 0.025 mm. The combined uncertainty in the LVDT displacement measurement based on the manufacturer's data is $2.8\mu m$. The range of displacement at the LVDT sensor is $\Delta l_{LVDT} = 1$ mm. In order to consider the measurement uncertainty of the geometric dimensions, the change of $z_{BalsaTip}$ with respect to $r_{LVDT-Hinge}$ and $r_{BalsaTip-Hinge}$ needs to be calculated for the maximum values of the range of motion. The combined uncertainty is then $u_{BalsaTip} = \sqrt{\left(\frac{\partial \Delta z_{BalsaTip}}{\partial \Delta l_{LVDT}} \delta \Delta l_{LVDT}\right)^2 + \left(\frac{\partial \Delta z_{BalsaTip}}{\partial r_{LVDT-Hinge}} \delta r_{LVDT-Hinge}\right)^2 + \left(\frac{\partial \Delta z_{BalsaTip}}{\partial r_{BalsaTip-Hinge}} \delta r_{BalsaTip-Hinge}\right)^2}$.

⁵ $\Delta z_{Pitot} = \frac{r_{Pitot-Hinge}}{r_{BalsaTip-Hinge}} z_{BalsaTip}$ with $r_{Pitot-Hinge} = 65$ mm and $r_{BalsaTip-Hinge} = 249mm$. The measurement uncertainties of the lengths is again 0.001 in. The overall range of motion $z_{BalsaTip}$ is 15 mm.

2.3.2 Offset Estimation Procedure

In order to estimate the offset of the LVDT calibration curves, a so called touch circuit is used. Because the Pitot tube is electrically insulated from the rest of the traverse, it can be used as a contact switch which closes an electric circuit when it touches the cone surface. The cone surface can then be used as a natural zero reference point for the Pitot probe positioning.

2.3.3 Pitot Probe

For the measurements two different Pitot probes were used. The first Pitot probe is made of a hypodermic steel tube with 0.89 mm outer diameter. The tip is flattened to an oval shape to increase the vertical resolution in the thin boundary layer of the cone and has a height of 0.46 mm and a width of 1.2 mm. The length of the Pitot tube is 12.5 mm. The second Pitot probe has the same length but an inner diameter of 0.25 mm and an outer diameter of 0.5 mm. This allows for a higher spacial resolution and less flow interference. The influence of Pitot tube length and diameter on the interference with the flow field is examined in [19]. It shows that Mach number profiles obtained with a probe diameter of 0.4 mm and a length of 12.5 mm should generate an error in Mach number of at least 35%. Nevertheless, under the assumption of a constant offset it should adequately resolve a change in axial flow velocity associated with cross flow vortex formation over different azimuthal positions. At the most upstream position of the Pitot probe tip, minimum wavelengths of the stationary cross flow modes are expected to be around 0.9 mm based on the local cone circumference at $x = 3.5$ in and a wavenumber of $m = 70$. An inner diameter of the Pitot probe of 0.25 mm is about a quarter of the shortest expected wavelength and should be therefore sufficient to

resolve the wavenumber content of the stationary cross flow modes. The pressure on the static pressure ports on the cone, stagnation pressure, and the Pitot probe pressure were measured with a Baratron⁶ 690 pressure transducer in combination with a MKS Type 670 signal conditioner.

2.4 Data Acquisition

The data acquisition is done with the PMCCorp⁷ motion control card which includes 8 analog input channels. These are used to monitor the total pressure of the pitot tube, the static pressure at the surface of the cone, the surface contact circuit, the LVDT-Demodulator output and the temperature in the testsection. The program to control the traverse motion and data acquisition is written in C.

2.5 Numerical Stability Analysis

As described in the introduction, the choice of the wave number and location of the initial disturbance is crucial for the successful application of subcritical forcing. Dr. P. Balakumar from the NASA Langley Research Center, Flow Physics & Control Branch provided a stability analysis of the cone model at experimental conditions. He solved the full compressible Navier Stokes equations with a 5th order weighted essentially non-oscillatory (WENO) scheme for spatial discretization and a third order total-variation-diminishing (TVD) scheme for temporal integration. The linear stability analysis was then performed assuming local parallel theory. Further details are given in [3].

Linear stability analysis predicts the location of branch I and wavenumber of the

⁶MKS Instruments, Andover, MA

⁷Precision MicroControl Corp., Carlsbad, CA 92011

initially most amplified stationary cross flow mode accurately. Growth rates

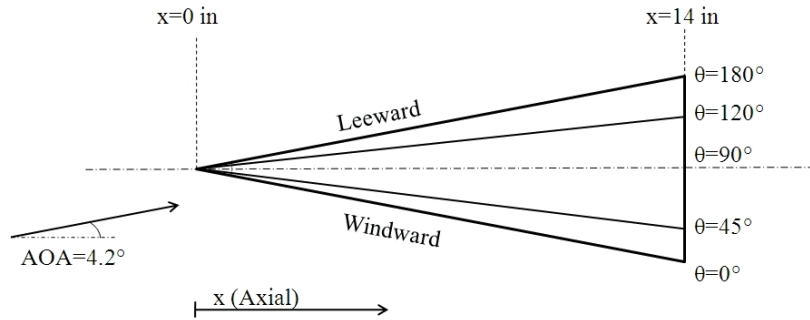


Figure 2.10. Rays of constant azimuthal angle on the cone.

and N-factors for the most amplified and one less amplified stationary cross flow mode along rays of constant azimuthal angle at 45° , 90° and 120° as depicted in figure 2.10 are shown in figure 2.11. The top and bottom row show the results for free stream unit Reynolds numbers of 250,000/in and 500,000/in. The stationary cross flow modes start to be amplified around axial locations of 0.5 to 1 in depending on the free stream Reynolds number. Therefore a location of $x = 0.5$ in is chosen for the placement of the instability forcing which ensures that forcing happens in all cases upstream of the point of neutral growth. The wavenumber of the initially most amplified stationary mode is very close to 45 for each case and is thus defined as the critical wavenumber. Based on the critical wavenumber, the subcritical wavenumber is defined as a wavenumber that is larger than the critical wavenumber. A factor of 1.5 between the critical and the subcritical wavenumber was chosen so that the subcritical forcing case corresponds to $m = 68$.

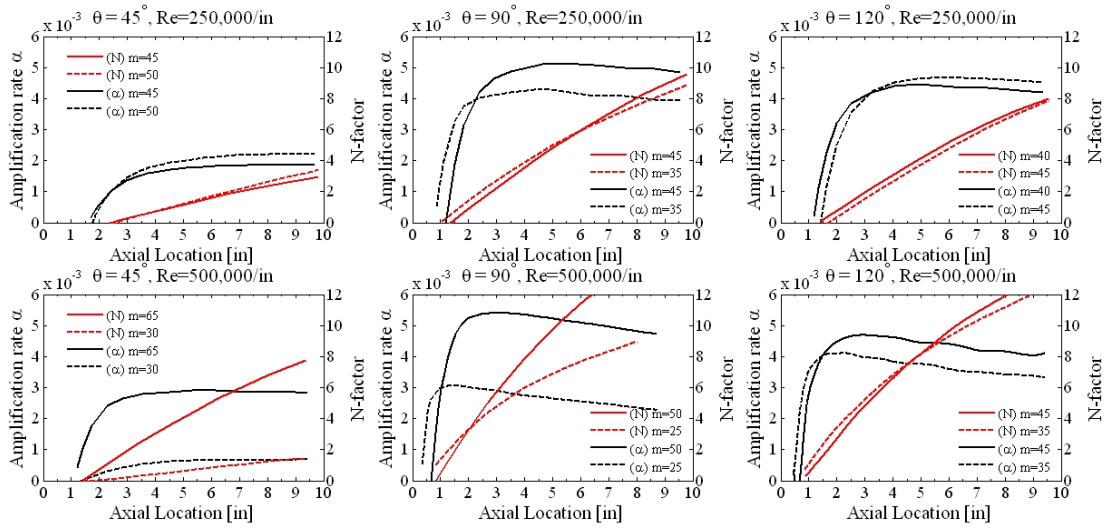


Figure 2.11. Growth rates and N-factors for axial rays at constant azimuthal angle θ obtained from Balakumar's linear stability calculations.

2.6 Disturbance Generators

The exchangeable cone tip is made of Polyamide-imide or Torlon⁸ 4301 resin which is electrically insulating and possesses a high tensile strength of 82 *MPa*. A non conductive material was chosen to make the future usage of plasma generators on the surface possible.

2.6.1 Mechanical Dimples

Two different cone tips were made which had 68 and 45 equi-distant dimples around the circumference at 0.5 in axial distance away from the tip. The dimples were generated with a sharp needle that was pressed into the relatively soft Torlon surface. The number of dimples corresponds to the wavenumber m which is supposed to be excited in the experiments. A Keyence Model VHX-600 3-D Imaging

⁸Trademark of Amoco Performance Products, Inc., Alpharetta, GA

Microscope is used to quantify the depth and size of the dimples. The dimples on the $m = 45$ tip are oval and with a length of $245 \mu\text{m}$, an azimuthal width of approximately $145 \mu\text{m}$ and a depth of $39 \mu\text{m}$. The wavelength to diameter ratio is 0.65. The dimple diameter of the $m = 68$ cone tip is about $80 \mu\text{m}$ with a

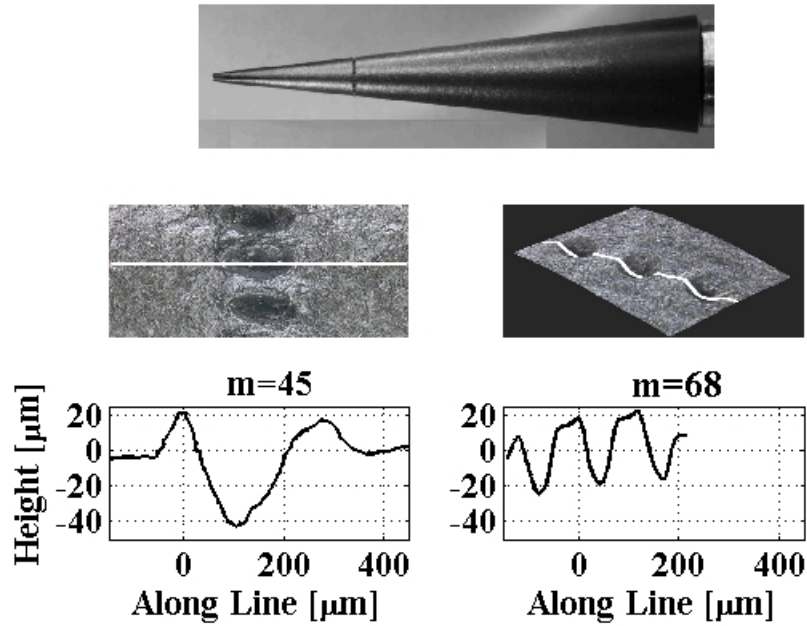


Figure 2.12. Pictures of the $m = 45$ cone tip and magnified views on the $m = 45$ and $m = 68$ dimples including the topography across the dimples.

diameter to wavelength ratio of about 0.6. The wavenumber $m = 45$ corresponds to the naturally most amplified wavenumber whereas $m = 68$ represents a subcritical wavenumber. Again, a wavenumber is subcritical if it is larger than the

critical wavenumber, e.g. $\frac{3}{2}$ times the most amplified wavenumber. The dimple dimensions exceed the minimum diameter to wavelength ratio of 0.5 for effective forcing for a bump as described by Saric and Radeztsky [20].

A third cone tip made of polished steel with mirror finish was used as unforced reference case, denoted as $m = 0$.

2.6.2 Plasma Disturbance Generators

Two different approaches were used to fabricate a controlled wavenumber plasma disturbance generator for the tip of the cone. One is the usage of individual circular plasma dots, acting like miniature synthetic jets and the other one is the design of a serrated edge actuator that generates streamwise vorticity. There are two main challenges in the design of the plasma actuator based disturbance generators. At first, it is very important not to introduce any passive roughness effects by adding a plasma actuator to the surface and secondly, the space where the plasma needs to be generated is very confined and not flat as e.g. on airfoil surfaces. The design and fabrication of the actuators under these challenging constraints is described in the next subsections.

2.6.2.1 Individual Circular Plasma Dots

The fundamental idea is to generate plasma in localized spots to introduce a vortical disturbance into the boundary layer.

The standard DBD plasma actuator arrangement consists of two asymmetrically arranged electrodes separated by a dielectric layer (See left or right half of cut A-B in figure 2.13). If an AC voltage with sufficient amplitude is applied, a weakly ionized gas forms at the edge of the exposed electrode. Whenever the temporal

change of the AC voltage is at its maximum, a plasma sheet forms on the surface and sweeps away from the exposed electrode. The charged particles exchange momentum with the neutral ambient air and a net body force away from the exposed electrode edge is asserted on the surrounding air which leads to the formation of a wall tangential jet of air.

In order to generate a pattern of individual circular plasma zones, a similar arrangement is chosen. Two plane copper electrodes are again separated by a dielectric. The exposed electrode is continuous except for circular holes which are cut into the exposed electrode. When an AC high voltage signal is supplied to the electrodes, plasma forms at the edges of the holes on the dielectric. The plasma asserts a body force on the neutral air that points towards the center of the hole and generates a flow field comparable to a synthetic jet in wall normal direction. A schematic of the geometry and flow field is shown in 2.13.

2.6.2.2 Serrated Edge / Comb actuator

The second electrode pattern is designed as a comb structure that is very similar to the successfully used streamwise vortex generators for the excitation of CF vortices by Corke and Saric in 2001 as shown in figure 2.14. The plasma around the comb-shaped electrode fingers accelerate fluid in normal direction away from the electrode edges. Whenever the flow from two facing surfaces collide, an updraft normal to the surface is generated and forms a vortical structure. This happens at each finger of the comb structure which results into the generation of pairs of co- and counter-rotating vortices. A detailed analysis of the flow field of the comb actuator is given in chapter 3.

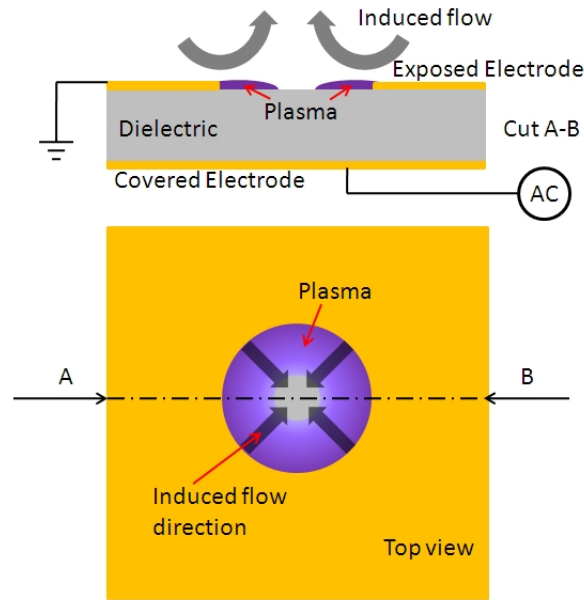


Figure 2.13. Schematic drawing of a single plasma dot actuator arrangement including the induced flow direction.

2.6.2.3 Vapor Deposition

The challenge with cross flow experiments is the very high sensitivity of the cross flow instability to surface roughness. The patterned surface electrode has to be smooth enough to disappear within the natural random surface roughness. Otherwise the targeted cross flow modes will be excited no matter if the plasma is turned on or off.

One method of generating a smooth surface despite of holes in the exposed electrode is the usage of a very thin exposed electrode layer. The material which is chosen is Copper due to its good electrical conductivity and its simple treatment for etching and patterning. Copper has a resistivity of $\rho = 1.68 \times 10^{-8} \Omega m$ which results depending on the thickness t , width W , and length L into a resistance of $R = \frac{\rho L}{tW}$. Assuming that $L = 1.1$ in and $W = 0.39$ in (circumference at the plasma

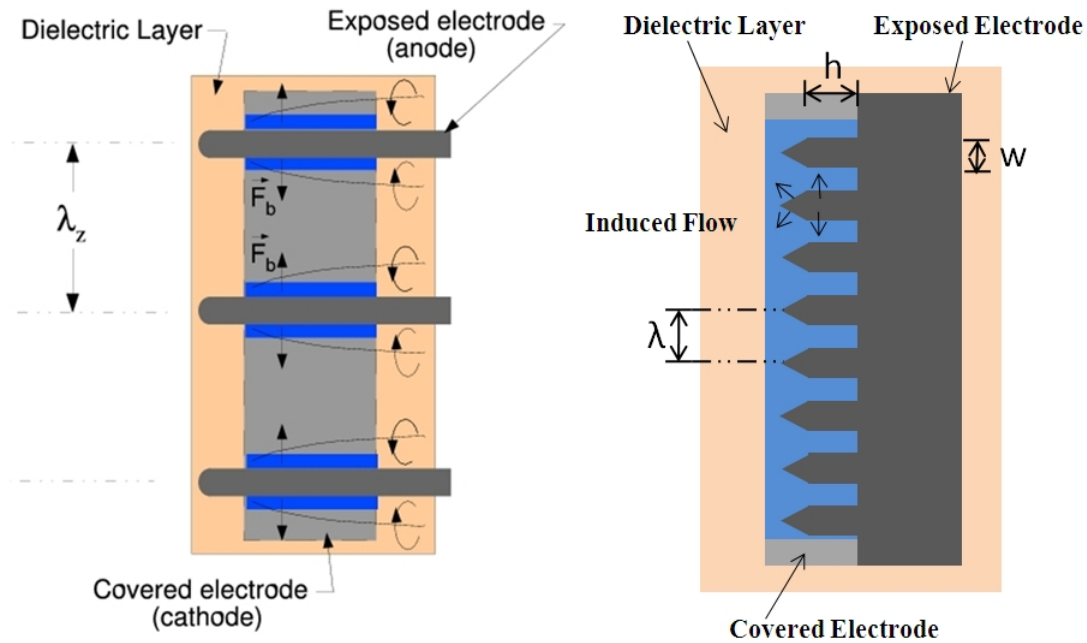


Figure 2.14. Left hand side: Schematic of the streamwise vorticity generator as used by Saric and Corke in 2001 to excite stationary cross flow modes. Right hand side: Drawing of the comb actuator geometry as used in the current supersonic experiments. λ is the wavelength of the desired stationary mode, either $m=45$ ($218 \mu\text{m}$) or $m = 68$ ($144 \mu\text{m}$).

$$h = \lambda \text{ and } w = \lambda/2$$

array at $x = 0.5$ in) a thickness of only 47 nm is sufficient to result into a sheet resistance of less than 1Ω . A thickness of 47 nm is less than a tenth of the rms roughness for a surface with mirror finish.

One of the most common ways of generating a thin layer of a non-organic material is vapor deposition. The sample to be coated is placed inside the ultra high vacuum chamber of an electron beam evaporator facing a small crucible filled with solid copper. An electron beam is focused onto the copper which heats it up so that it liquifies. The copper slowly evaporates and condenses on all the surfaces

which are in direct line of sight. The deposition rate and final thickness can be accurately monitored with a quartz crystal deposition controller.

2.6.2.4 Kapton Film Actuator

A few test actuators were made of 0.5 and 1 mil thick Kapton⁹ film. The process consists of multiple steps: Mask making, photolithography, vapor deposition, and lift-off.

The mask is designed with a CAD software and then translated into a set of equivalent squares which are loaded into the mask making machine control software. The machine then exposes the pattern with UV light into a chromium emulsion on a glass carrier.

In the first step of the process, the Kapton film is attached with thermal release tape (Revalpha¹⁰) on a 120 mm diameter Silicon wafer. Thermal release tape loses its adhesion when heated up above a certain temperature. If the tape was just standard pressure sensitive glue there would be a good chance that the deposited copper peels off when being removed from the Silicon wafer carrier. The wafer itself is used to hold the Kapton film for further processing in standard machines for microelectronic fabrication. In the second step, the surface of the Kapton film is coated with a thin layer of AZ¹¹ 5214 negative photoresist in a spin coater. The resist is then exposed with UV light using the mask which was made in the step before. After developing the resist, there is a series of circular islands left on the surface of the Kapton. In the third step, Copper is deposited on the surface with the resist islands. After deposition, the Copper layer is cleaned with Acetone

⁹Trademark of E.I. DuPont de Nemours and Co, Wilmington, DE

¹⁰Nitto Americas, Inc., Teaneck, NJ 07666, U.S.A.

¹¹Clariant Corporation, Somerville NJ 08876

which dissolves the resist under the copper and removes the copper on top of the resist residues. The result is shown in figure 2.15. This technique is also known as "lift off" patterning. In the last step, the wafer is heated up to release the Kapton film. The Kapton film is then again glued with thermal release tape on a silicon wafer, this time the copper is facing the wafer. The "covered" electrode is then vapor deposited on the upward facing side.

The Kapton film with the exposed and covered electrodes is finally cut into a

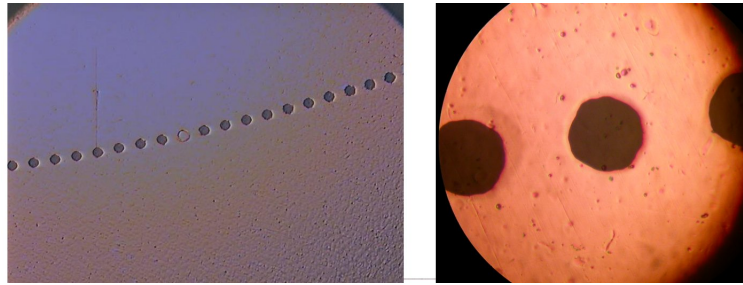


Figure 2.15. Enlarged image of the exposed electrode after lift off. Each dot has a diameter of 0.003 in and is spaced approximately 0.006 in apart. The substrate is a 0.5 mil thick Kapton film.

pie-like shape and wrapped around the cone tip. Two component Epoxy is used as glue.

The cone tip itself was made of Torlon and designed with a hollow center and a through hole drilled through the surface to make space for a thin wire soldered with low temperature solder to the covered electrode. The low temperature solder melts at 275° F. When higher temperatures are applied to the deposited copper,



Figure 2.16. 0.5 mil thick Kapton actuator glued to a Torlon carrier cone. Right hand side picture shows the operating plasma dots at 3 inHg ambient pressure with 2.2 kVpp and 3 kHz sin-wave HV

the copper immediately peels off leaving nothing but the bare Kapton surface. Although the plasma dots generate plasma as planned, it is almost impossible to glue the Kapton film actuator on the surface of the Torlon carrier cone without adding any steps or other unwanted surface modifications. It is not possible to wrap the Kapton film around the cone without leaving a little gap where both edges meet. Especially the step that is formed at the upstream end of the Kapton film is a significant source of surface roughness. This is very critical due to its proximity to the neutral growth region. Nonetheless a picture with the glued Kapton film and running plasma with this arrangement is shown in figure 2.16. The surface step when transitioning from the Torlon cone to the glued Kapton film towards the tip can be clearly seen. Therefore the Kapton film approach is not further pursued but instead a design which uses the cone itself as dielectric is developed. The description is given in the following section.

2.6.2.5 Dielectric Cone Actuator

In order to avoid the difficult process of wrapping and gluing the Kapton film on the cone tip surface, the cone tip structure itself was designed as dielectric. The cross section of the final design is shown in figure 2.17. The cone tip consists of two materials, Macor¹² towards the tip and Aluminum at the base. The tip itself is made in several steps. At first a 7° tapered end mill is used to drill a tapered hole into a 3/8 in diameter Macor rod. Then a 7° taper is cut into the end of an Aluminum rod which has a through hole in the center to account for the electrical connection of the covered electrode. Conductive silver epoxy (Loctite¹³ 3888) is filled into the tapered hole of the Macor rod to act as covered electrode and to hold the FEP coated high voltage wire¹⁴. It has an outer diameter of 0.05 in and is rated to 14 kVrms dielectric strength. The high voltage wire is lead through the through hole in the Aluminum rod and both parts are joined together at the tapered end of the Aluminum rod and the tapered base of the Macor rod by filling the formed cavity with fast curing two component epoxy (Loctite 608). The joined parts are then cut in a lathe into the conical shape whereas the dimensions are calculated so that the wall thickness at the Macor tip is about 15 – 20 mils. The entire surface of the cone tip is then smoothed with sandpaper (grit size 280 to 1800) and lapping compound (equivalent grit size 3200). The wall thickness of the Macor part is about 15 - 20 mil which results in a dielectric strength of 12 - 15 kVpp [29]. The tip consists now of the dielectric and the powered, buried electrode. The exposed electrode is made by depositing Copper on the outer surface of the cone tip, on top of the Macor and the Aluminum part of the cone

¹²Corning SAS, 77211 Avon Cedex France

¹³Henkel AG & Co. KGaA, D-40589 Düsseldorf

¹⁴ETN-2026-10, Connectronics Corp, Toledo, OH-43607, USA

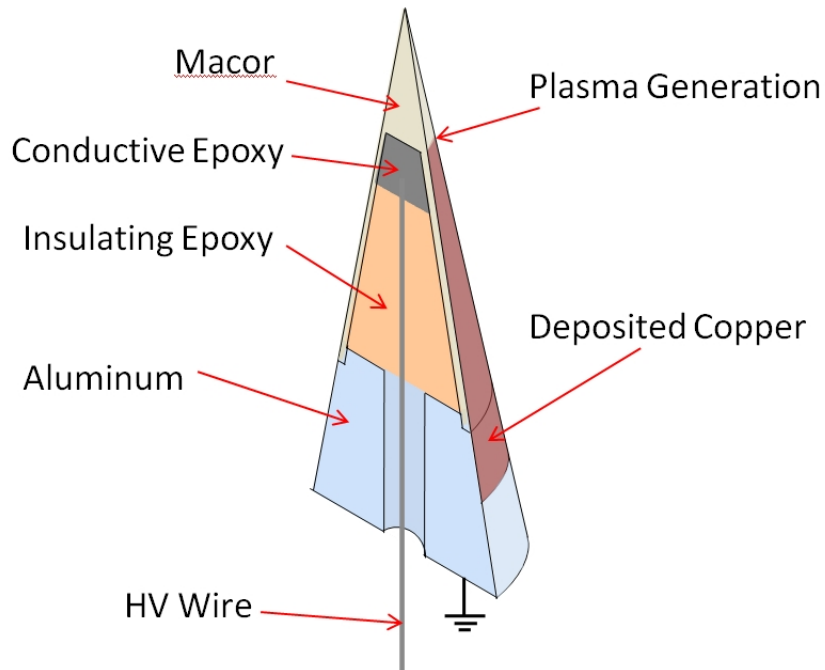


Figure 2.17. Drawing of the Macor/Aluminum cone tip showing the cross section.

tip. By doing so, the continuous Copper layer is electrically connected to the base of the cone tip which is in turn connected to the entire experimental setup at ground potential.

The surface curvature of the cone is a big challenge for photolithography. Neither of the standard techniques, spin coating and the usage of a flat mask can be directly applied to the cone. A solution was found by using positive MicroSpray spray-on photoresist from Microchem¹⁵. It comes in a can and can be easily sprayed on the surface of the cone tip. The best result is obtained by spraying one passage every 45° over the cone tip at about 8 in distance. The resist was then baked in an oven for about 10 minutes at 120° F to evaporate the solvent in the

¹⁵Microchem Corp., Newton, MA 02464

resist layer. The manufacturer originally recommends a higher baking temperature of about 220 F on a hot plate. Unfortunately this exceeded the Loctite 608 Epoxy glass transition temperature which made the epoxy expand strong enough to push the two parts apart.

A mask pattern as shown on the right hand side of figure 2.14 was designed in AutoCAD and sent to be printed on a 0.1 mm thick polyester based transparency with a line resolution of 10 μm .

The mask was flexible enough to be bent around the cone surface. In order to push the mask close enough onto the surface for contact masking, two conical rings made of Torlon were slipped over the mask on the cone tip. For exposure a Spectronics¹⁶ SB-100P UV-A lamp with 4.8 mW/cm² (at 15 in distance) was pointed at the masked cone which was mounted in a mechanical indexer. Sufficient exposure was achieved when the color of the reflected light on the photoresist changed from a purple to an orange tone. This happened usually after 20 – 25 seconds if the light source was about 4 in away from the surface. The cone is then axially rotated by a quarter turn to continue the exposure.

After developing the resist a positive pattern stays on the surface of the exposed electrode. Cu 49-1 Copper Etchant¹⁷ is used to remove the uncoated copper and only the desired electrode pattern stays on the Macor surface. Figure 2.18 shows the dot pattern corresponding to a forcing wavenumber of $m=45$ on the dielectric cone surface.

In the next figure 2.19, the cone tip with the serrated edge structure is shown. There are three images: (a) the overall view of the Macor cone tip, (b) a magnified view of the electrode edge and (c) a high resolution image of separate fingers of the comb electrode. The highly magnified image of

¹⁶Spectronics Corp., Westbury, NY 11590

¹⁷Transene Company, Inc., Danvers, MA 01923

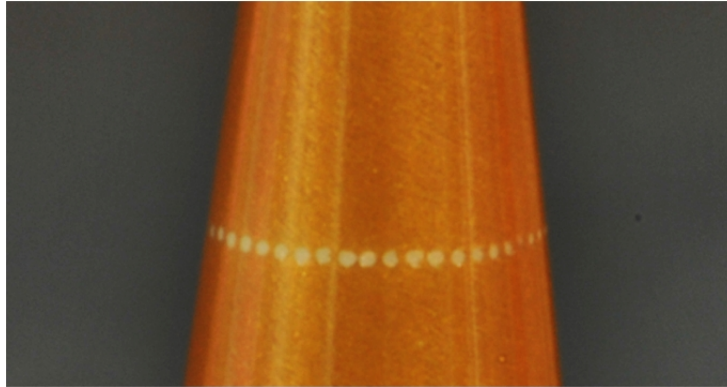


Figure 2.18. 5 mil diameter Plasma Dots with $m=45$ spacing on a Macor dielectric cone tip

the exposed electrode pattern was taken after the wind tunnel runs with plasma were finished. It shows that the electrodes were not physically altered by the presence of the plasma. The $m = 45$ and $m = 68$ serrated edge actuators with plasma on are shown in figure 2.20 at 3 inHg ambient pressure. It is clearly visible that concentrations of plasma are formed at the location of the sharp tips of the single fingers of the electrode edge. Additionally there is a 2D plasma sheet generated around the electrode edge. The flow field generated by the actuator arrangement is further investigated in chapter 3.

2.6.3 Surface Roughness Characterization of the Cone Tips

Still waiting for Steve...

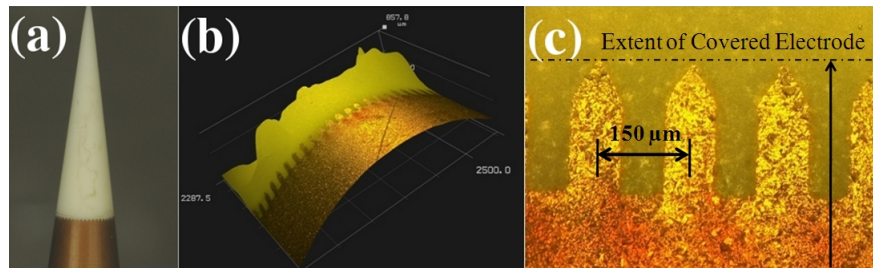


Figure 2.19. Image (a) shows the serrated edge design on the Macor plasma tip. The pattern corresponds to a $m=45$ roughness tip. (b) is the magnified view of a $m=68$ plasma roughness tip with a Keyence Model VHX-600 3-D Imaging Microscope, and (c) is a high resolution optical image of four single "fingers" of image (b)

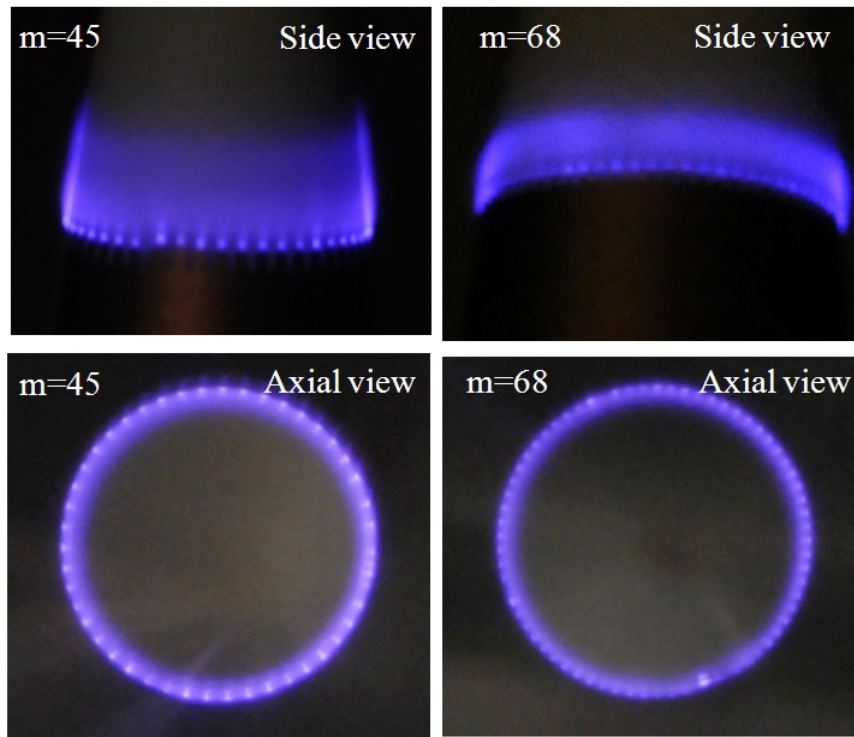


Figure 2.20. The images show the plasma pattern that forms around the edges of the exposed electrode on the dielectric cone. A voltage of 5 kVpp in 3 inHg ambient pressure with a sine AC signal of 5 kHz is applied. Concentrations of plasma are formed around the tips of the "fingers" of the serrated edge. Additionally a two dimensional plasma sheet can be seen.

CHAPTER 3

DBD Plasma Roughness Array Evaluation

3.1 Circular Plasma Dots

The circular plasma dot design worked on the 0.5 mil thick Kapton film in sub-atmospheric pressure around 3 inHg. A voltage of less than 2 kVpp was necessary to start the plasma inside the circular holes of the exposed electrode. The same electrode pattern on the dielectric Macor cone on the other hand did not show any plasma up to the maximum tested voltage of 9 kVpp. It was not possible to further increase the voltage because the internal insulation between the powered and grounded electrodes was not strong enough in the low pressure environment to withstand higher voltages. This made it impossible to use the circular pattern for actual wind tunnel testing. The question raised what the reason for the increased plasma initiation voltage was. The main difference between both setups is the thickness of the dielectric. The diameter of the circular holes in the exposed electrode was increased from 0.003 in to 0.005 in for the Macor cone tip whereas the dielectric thickness was increased by a factor of 40 from about 0.5 mil to 15 - 20 mil. Interestingly, the initiation voltage for the thick dielectric Macor cone with just a straight edge actuator turned out to be approximately 3 kVpp at 3 inHg with 5 kHz sine waves.

To answer the question why there is such a discrepancy between the initiation

voltages of the straight edge plasma actuator and the two circular actuator designs on the Kapton tape and the Macor dielectric, the electrical field norms in the vicinity of the electrode edges are compared. The straight edge actuator is the reference case to estimate which voltage is necessary to cause breakdown with the circular actuators, assuming that a certain minimum break down field strength needs to be surpassed for its initiation.

The static electrical potential is calculated by solving the Poisson equations of electrostatics in Comsol¹ 4.0. The geometrical model is a 2-D axisymmetric case for a single circular plasma actuator. The 2-D cross section including the mesh is shown in figure 3.1. A total amount of 275,000 free triangular mesh elements

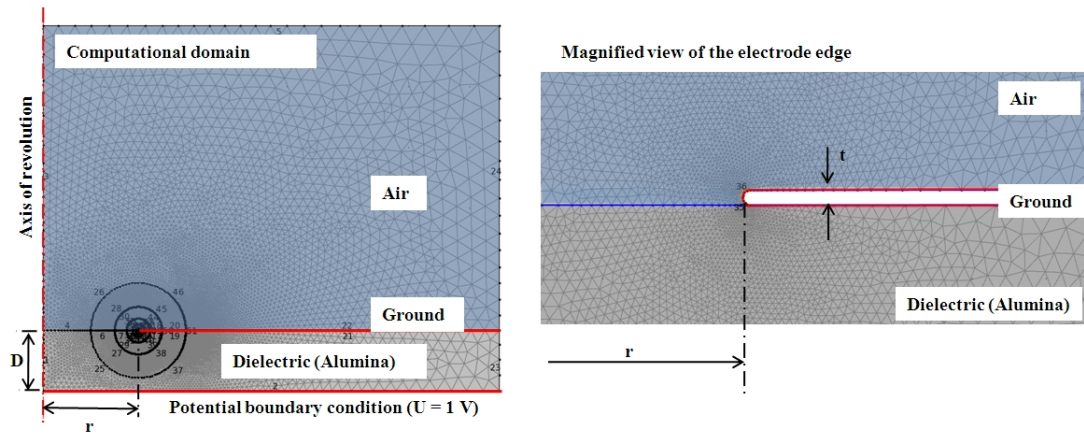


Figure 3.1. Modeling of the circular plasma actuator in Comsol. D is the dielectric thickness, r is the radius of the circular dot and t is the thickness of the electrode. A parametric sweep of $\frac{r}{D}$ from 0.12 to 3 is done. $\frac{t}{D}$ stays constant and is 4×10^{-4} .

¹Comsol, Inc

were used in mesh A. The mesh has its highest resolution around the leading edge of the exposed grounded electrode where a total amount of 80 nodes is placed to resolve the field gradients. Each of the concentric circles around the electrode edge has 560 nodes. The left hand side boundary of the computational domain is defined as 2-D axisymmetric boundary condition and the bottom side is defined as potential boundary condition. The remaining boundaries are defined with charge conservation. The edges of the exposed electrode are set to ground potential. To ensure grid independence, the same calculations are done on the the same geometry with 370,000 elements and 120 nodes on the edge of the exposed electrode (Mesh B). Each concentric circle around the electrode edge holds 760 nodes in case of the refined mesh. As can be seen in figure 3.3 the maximum electrical field norm is matching up in amplitude and location between mesh A and B, insuring a mesh independent solution.

In order to evaluate the effect of the geometrical changes to the actuator from a traditional straight edge arrangement to the circular dot pattern, the ratio r/D is introduced. r is the radius of the circular plasma actuator and D is the dielectric thickness. r/D is about 0.15 for the 20 mil thick macor dielectric and about 1.5 for the 0.5 mil thick Kapton film actuator. Interestingly the equipotential lines of the voltage seem to be strongly limited above the free dielectric surface with the smallest r/D ratio as shown in the surface potential plots in figure 3.2. When the radius of the hole in the exposed electrode is increased, more field lines with higher potential are forming above the dielectric surface. This behaviour is reflected in the electrical field norm plots of figure 3.3. The field norm is normalized by the dielectric thickness and the potential which is applied to the covered electrode. In all cases the maximum field strength occurs directly at the

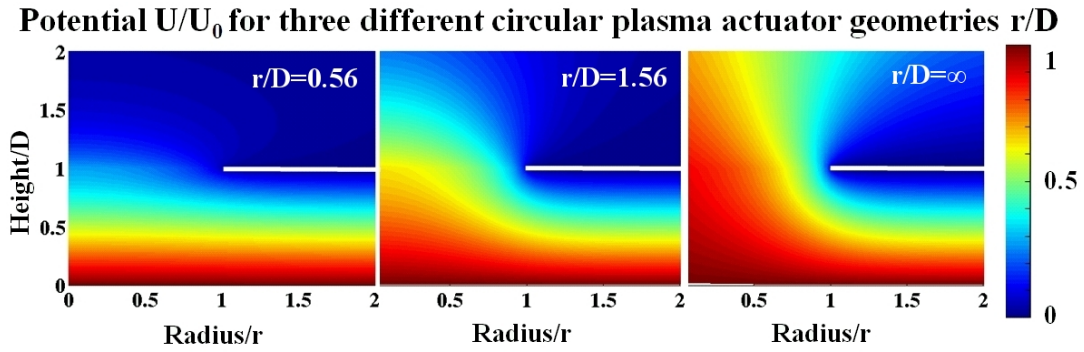


Figure 3.2. Surface plots of the normalized potential U/U_0 for $r/D=0.56$, $r/D=1.56$ and the limit case of the standard straight edge arrangement ($r \rightarrow \infty$) for mesh A.

rounded edge of the exposed electrode and falls off quickly towards the center of the circular actuator. The maximum peak is growing with increasing r/D ratio, showing that the presence of an electrode with the same potential on the opposite side weakens the overall electric field strength. Assuming that the break down field strength for an ambient pressure of 3 inHg and a frequency of 5 kHz at the straight edge actuator needs to be the same to generate plasma in the circular electrode arrangement, a dimensionless initial electrical field norm of roughly 300 has to be surpassed. This means for the tested dot diameter ratio of 0.15 that the applied voltage needs to be at least three times larger to increase the dimensionless field strength to a value sufficient for plasma initiation. The actuator was tested up to 9 kVpp but according to this calculation a minimum voltage of 9 kVpp would have been sufficient to initiate plasma. Nonetheless even by increasing the diameter of the dots by a factor of two, no plasma could be generated. Doubtlessly, the dot geometry weakens the field potential and leads to the formation of weaker electric fields at the exposed electrode edge with decreasing dot diameter.

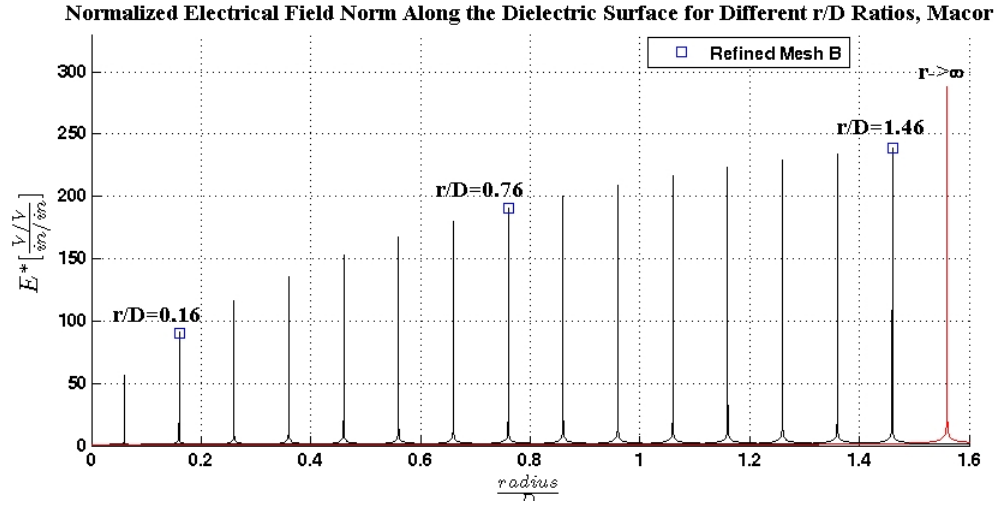


Figure 3.3. Comparison of the unit electrical field norm E^* with the unit $\frac{V/V}{in/in}$ along the dielectric surface for mesh A.

3.2 Serrated edge actuator

The serrated edge actuator is a slightly modified miniature version of a standard stream wise vortex generator. In order to measure the induced flow field, 2-D PIV measurements were done in two planes around the serrated edge geometry. A 10 x 10 x 10 in large acrylic box was made to contain the seeding particles and the plasma actuator. In the first approach a serrated edge actuator was made on a flat piece of 15 mil thick Macor. The problem was that the 60 nm thick deposited copper eroded at the edge when the plasma was turned on in the seeding box. This was not observed when the plasma actuator was operated just in air. Additionally it was somewhat difficult to ensure a sufficient seeding density in the highly magnified field of view. Therefore the size of the actuator was increased by a factor of eight. The dielectric is still Macor and has a thickness of 1/8 in. The edge geometry is magnified by the same factor. Because the deposited electrode

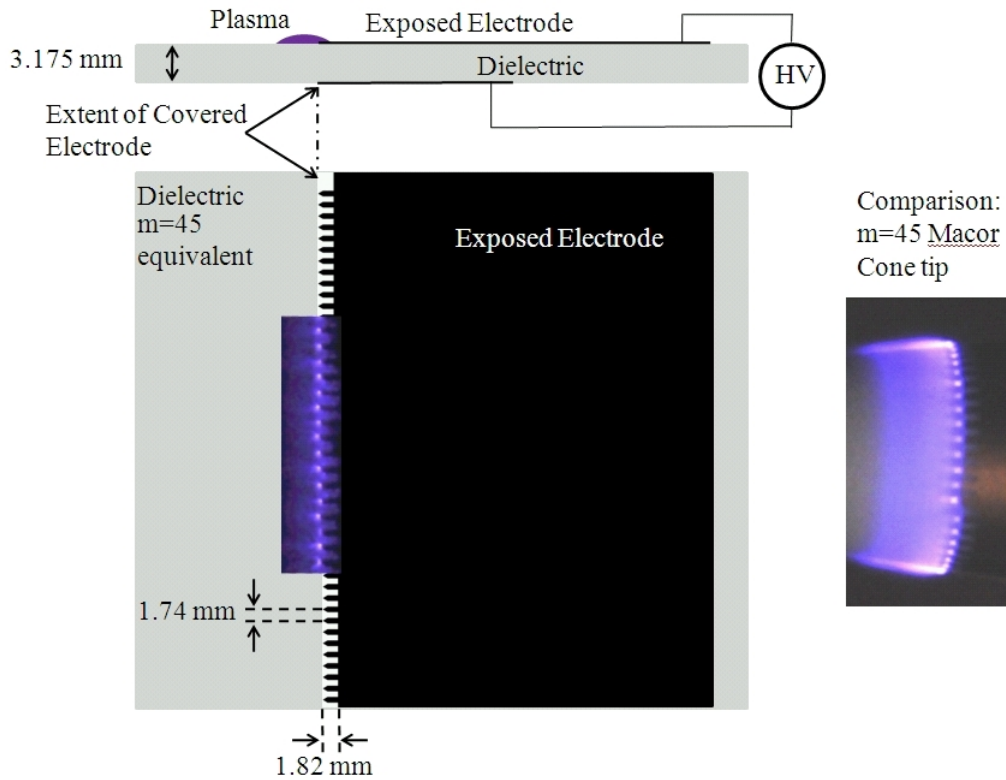


Figure 3.4. Schematic drawing of the 8x magnified $m=45$ equivalent serrated edge actuator. Included is a picture with plasma at atmospheric pressure, 24 kVpp and 5 kHz sine waves. On the right hand side is a picture of the actual $m=45$ Macor cone tip running at an ambient pressure of 3 inHg and 5 kVpp at 5 kHz sine waves

corrodes in the seeding and plasma environment, an exposed electrodes made of standard copper tape is used instead. The copper tape has a thickness of less than 1 mil and is cut with a razor blade to the same shape as used on the dielectric cone. The covered electrode is on the bottom side of the Macor dielectric and ends where the tips of the exposed serrated edge electrode ends. This is geometrically the same arrangement as on the Macor dielectric cone tip. A drawing including dimensions and images of the running plasma actuators is shown in figure 3.4. It

can be seen that the light emissions from the model actuator used for the PIV measurements and the cone tip used in the experiment are very similar. This similarity allows to assume that the qualitative behaviour of the flow field is in both cases similar as well.

The PIV system used for this study consists of a pair of New Wave² Nd:YAG

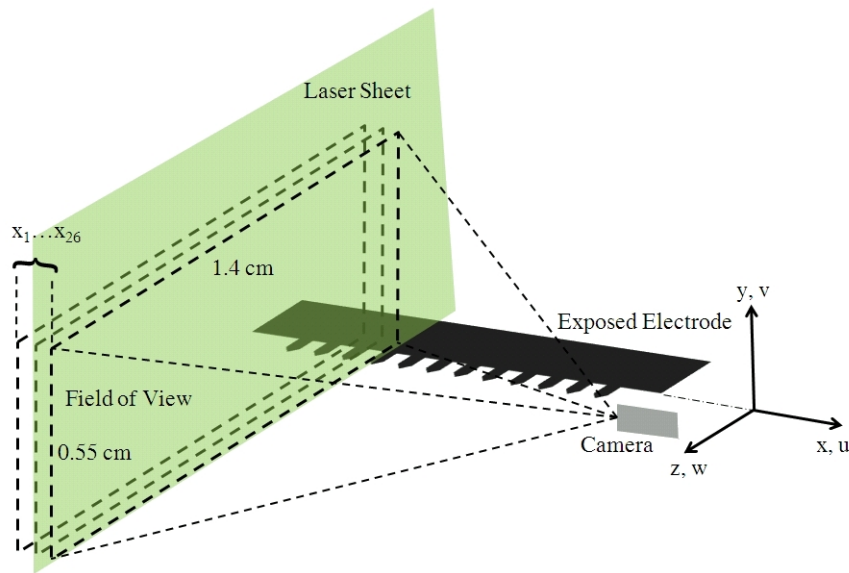


Figure 3.5. Drawing of the PIV light sheet and camera arrangement relative to the exposed serrated edge electrode

lasers, a PIVCAM 10-30 by TSI³ with 1000 x 1000 pixels resolution and a TSI synchronizer. Calibrations were done by holding a ruler in the center of the field of view, assuming that there is no significant distortion of the overall image created

²Electro Scientific Industries, Inc., Portland, OR 97229

³TSI Incorporated, Shoreview, MN 55126

by the used lense. For each location, 200 image pairs were taken to ensure temporal convergence of the mean vector fields. The interrogation area for the image correlations was set to 32 x 32 pixels with an overlap of 16 pixels for cross correlations. The time Δt between two image pairs was set so that the maximum particle displacement is roughly 10 pixels between two image exposures. Post-Processing of the obtained vector fields included a double correlation and the filling of areas where no valid correlations could be found.

The first set of PIV images is taken in z-y planes at twenty six x-locations as shown

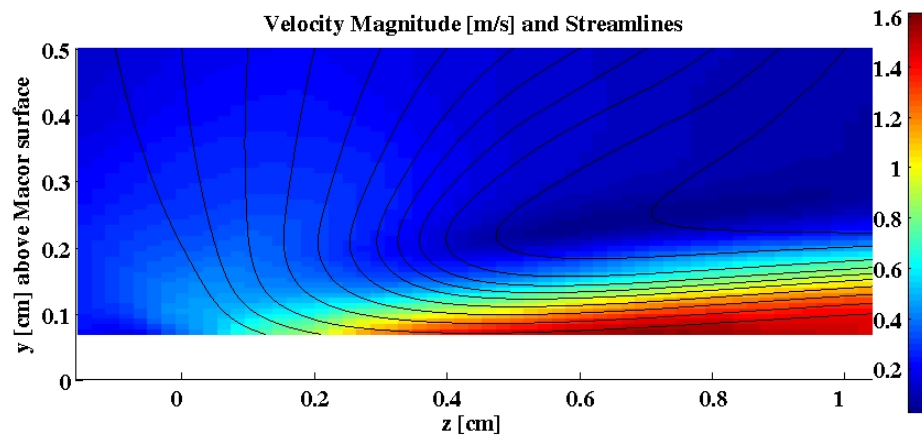


Figure 3.6. Velocity magnitude of the first plane at $x=0$ cm of v and w including streamlines.

in figure 3.5. The planes are spaced 0.15 mm apart. The x-spacing between the electrode tips of the exposed electrode is 1.74 mm which means that there are about 12 z-y planes over the wavelength of the serrated edge actuator. The origin

of the coordinate system is chosen so that $y = 0$ corresponds to the Macor surface and $z = 0$ corresponds to the edge of the exposed electrode. A voltage of 26

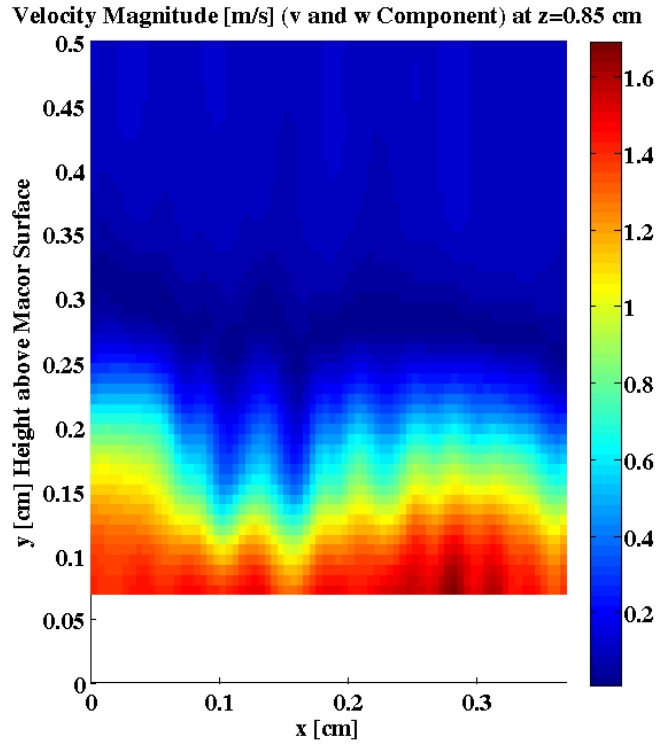


Figure 3.7. Velocity magnitude of v and w in the z-plane at $z=0.85$ cm. This plane was interpolated from a series of 26 x-planes (see figure 3.6) starting at $x = 0$ cm and ending at $x = 0.35$ cm

kV p-p with 5 kHz sine waves is applied to the covered electrode of the serrated edge actuator. The obtained velocity distribution including stream lines is shown in figure 3.6 for one z-y plane at $x=0$ cm. About 0.75 mm of the field of view

in wall normal direction were removed from the analysis due to light reflections from the copper electrode tape. A maximum induced velocity of about 1.6 m/s is measured. It can be seen that air is entrained from above the actuator edge at $z=0$ and accelerated in z -direction, forming a tangential wall jet. This is what is expected from a standard straight edge DBD plasma actuator arrangement. The difference to be shown is the variation of the flow field in x -direction with the

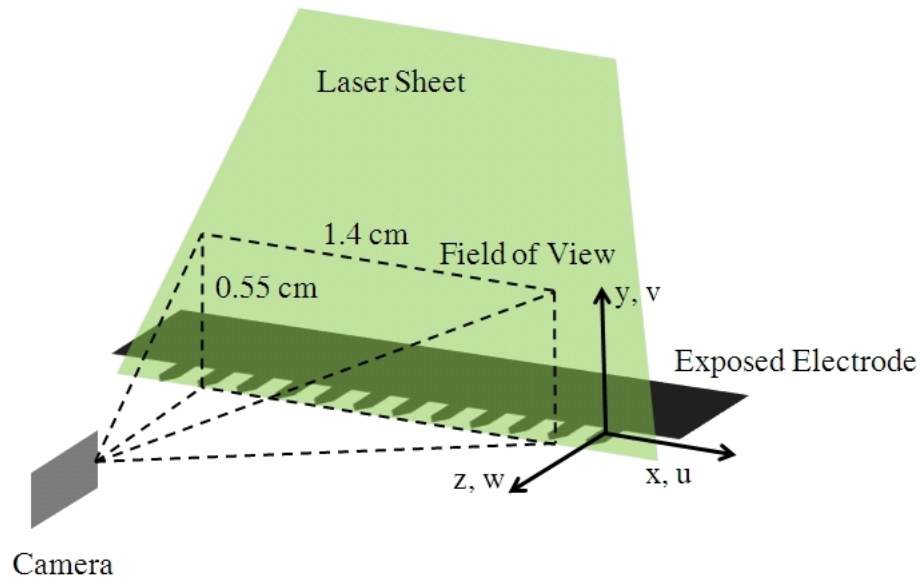


Figure 3.8. Drawing of the PIV light sheet and camera arrangement relative to the exposed serrated edge electrode

same span wise variation of the velocity field as the spacing of the serrations in the exposed electrode edge. For this purpose, the 26 x -planes are interpolated in

x-direction for a constant z-location. The result is a x-y plane with velocities in v and w direction. One of the x-y planes at $z=0.85$ cm is shown in figure 3.7. It can be seen that the height of the tangential wall jet changes with spanwise x-location. The maxima of the wall jet thickness are about 2 mm apart which corresponds to the span wise wavelength of the exposed electrode pattern. After showing that there is a span wise variation of the tangential velocity, it also needs to be demonstrated that vorticity along the z-axis is generated. In order to do that, the u and v velocity components in the x-y plane need to be measured. The arrangement to measure the u and v components is shown in figure 3.8. The x-y plane is located at $z=0.2$ cm, which corresponds to a position slightly in front of the tips of the comb electrode fingers. Again, about 0.07 cm above the Macor surface were removed from the PIV analysis because of light reflections off the surface. Figure 3.9 shows the z-vorticity calculated from the measured u-v velocity field. There is a regular pattern of changing positive and negative z-vorticity with an x-spacing of about 1.8 mm which is almost exactly matching the wavelength of the serrated edge actuator.

The PIV results show that the geometry as used on the dielectric Macor cones generates streamwise vorticity with the same span wise wavelength as the spacing of the serrations in the exposed electrode. Additionally, a wall tangential jet is generated in the same manner as for a standard straight edge DBD actuator. The thickness of the wall normal jet varies with the same span wise wavelength as the serrated actuator edge. Therefore the actuator generates 3-D disturbances, namely streamwise-vorticity and a spanwise modulation of the streamwise velocity with the same wavelength as the serration of the exposed electrode.

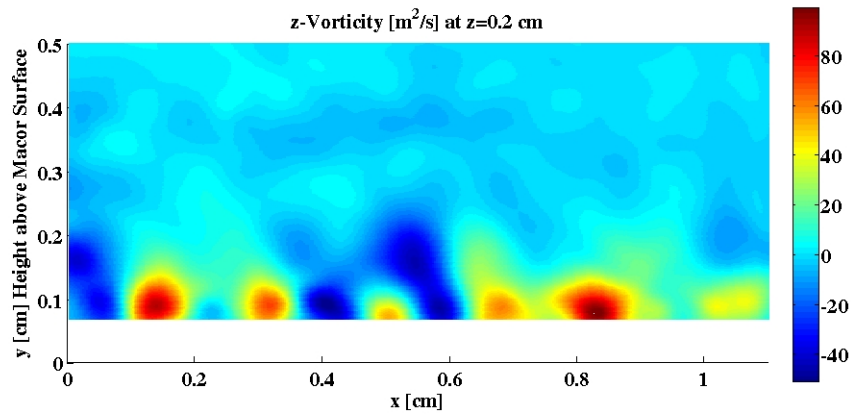


Figure 3.9. z-Vorticity of the serrated edge arrangement. The z-plane is positioned about 0.2 cm downstream of the actuator edge.

CHAPTER 4

MEASUREMENTS WITH THE DISTRIBUTED ROUGHNESS CONE TIPS

In the first step of the experiments, there has to be shown that stationary cross flow vortices are present in the cone boundary layer. If that is the case, receptivity to the used forcing wavenumber with the dimpled Torlon cone tips needs to be verified. Finally, the question can be answered if subcritical forcing delays the onset of laminar-turbulent transition in the same way as it does in subsonic flow. The following subsections illustrate the results of surface flow visualizations to visualize stationary structures and Pitot probe measurements to quantitatively evaluate the receptivity and laminar-turbulent transition of the boundary layer.

4.1 Surface Flow Visualization

Surface flow visualization is an indirect measure of the shear stress a surface is exposed to in air flow. The highly viscous visualization liquid is removed faster from the surface in regions of high shear stresses than in regions with lower shear stresses. This will lead in case of cross flow vortices to a streaky pattern on the surface the cone. The streaky pattern corresponds to the thinner and thicker parts of the boundary layer which are formed by the mean flow distortion of the cross flow vortices.

Half the cone surface was coated with a mixture consisting of 15 parts *Si* oil (1000

cs), 5 parts Oleic acid and 1 part TiO_2 . Different stagnation pressures between 25 *psia* and 50 *psia* were used for the three different cone tips. Snapshots from the videos showing the development of the surface patterns were taken and are presented in figure 4.1. The visible part of the cone which shows the surface flow visualization ranges from $x = 11$ in to $x = 14$ in. In each video the initially uniform oil coating developed into the shown stationary patterns, meaning that there was no change or shift of the pattern in progressing time. All pictures except otherwise stated are run in the windtunnel with open bleed valves so that the windtunnel was running in quiet mode. The notable difference with increasing Reynolds number is that the clear pattern of streamwise streaks disappears and is replaced by a diffuse layer of white color. The streaks are assumed to be cross flow vortices which are present on the entire visible surface from 30° to 180° at a tunnel total pressure of 25 psi. A comparison between the surface flow visualization of the three different tips shows that there is a slightly different azimuthal distribution of the cross flow vortices. This is a first qualitative indication that the boundary layer has been receptive to the different roughness distributions on the exchangeable cone tip. When the streaky pattern that dominated at $p_0 = 25$ psi disappears at higher stagnation pressures, transition is assumed to have taken place which washed away the stationary cross flow vortices. The baseline tip at $p_0 = 35$ psi shows almost no sign of stationary cross flow vortices except for three or four streaks on the leeward side. If the bleed valves are closed these streaks disappear completely. Looking at the flow visualization at 42 psi with open bleed valves shows that there are still some faint streaks left on the leeward side of the cone.

Because the cross flow instability is either exclusively governed by the stronger

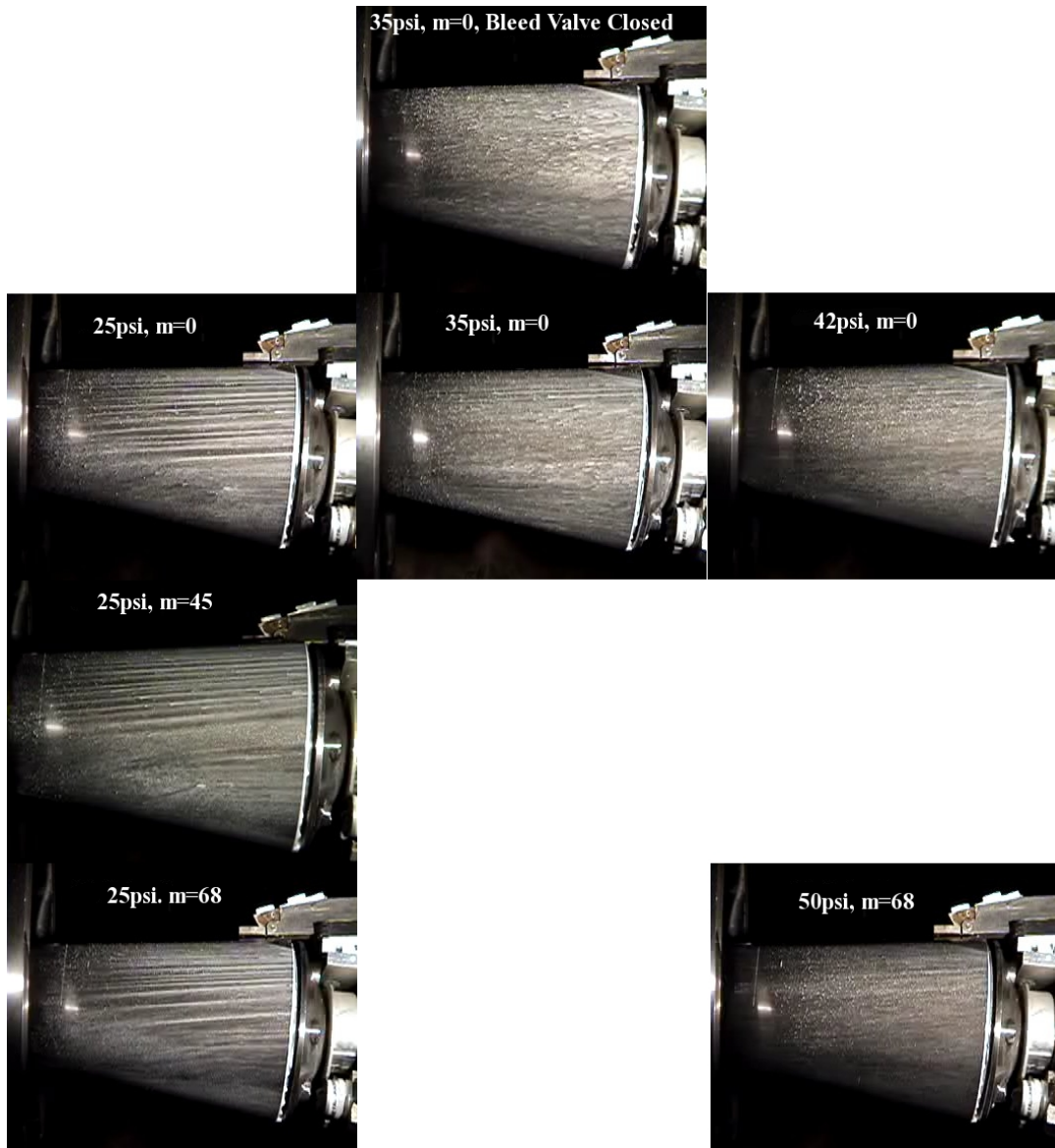


Figure 4.1. Surface Flow Visualization at different unit Reynolds numbers and flow conditions at Mach 3.5.

$$p_0 = 25\text{psi} \equiv Re = 9.45 \times 10^6 m^{-1}, p_0 = 35\text{psi} \equiv Re = 1.32 \times 10^7 m^{-1},$$

$$p_0 = 42\text{psi} \equiv Re = 1.59 \times 10^7 m^{-1} \text{ and } p_0 = 50\text{psi} \equiv Re = 1.89 \times 10^7 m^{-1}.$$

amplified travelling modes or the less amplified stationary modes, it can be concluded based on the clearly stationary structures in the flow visualization that the

dominant cross flow mode is stationary. This is exactly what is expected for a wind tunnel with low background disturbance levels.

4.2 Pitot Tube Surveys

The Pitot probe surveys make it possible to directly measure the mean flow distortion of the boundary layer and therefore the azimuthal wave numbers of the stationary cross flow instability. A quick method to prove receptivity to the forcing wavenumber are azimuthal scans at constant height above the cone surface inside the boundary layer. Whenever the pitot probe traverses thicker or thinner parts of the boundary layer, an increase or decrease of measured pressure will be registered.

4.2.1 Receptivity to Forcing Wavenumber

Receptivity to the used distributed roughness tips is shown with azimuthal pitot probe scans at constant height above the surface. The traces of the azimuthal scans is schematically shown in figure 4.2. Based on the flow visualization images in figure 4.1 a stagnation pressure of 25 psia is chosen to ensure laminar flow over the entire cone body. The axial location of the pitot probe is $x = 11.2$ in or at an axial Reynolds number of 2.79×10^6 . The total temperature was set to 100° F. The cone tips used in these measurements were a polished steel tip for the $m = 0$ or natural roughness case and the $m = 68$ subcritical wavenumber Torlon tip. The first pitot probe scan is shown in figure 4.3. The measured azimuthal Pitot pressure traces are analyzed three-fold. At first, the signal is at $m = 15$ high pass filtered and then normalized by its maximum. Absolute amplitudes are at this point of no specific interest because only the wavenumber content is

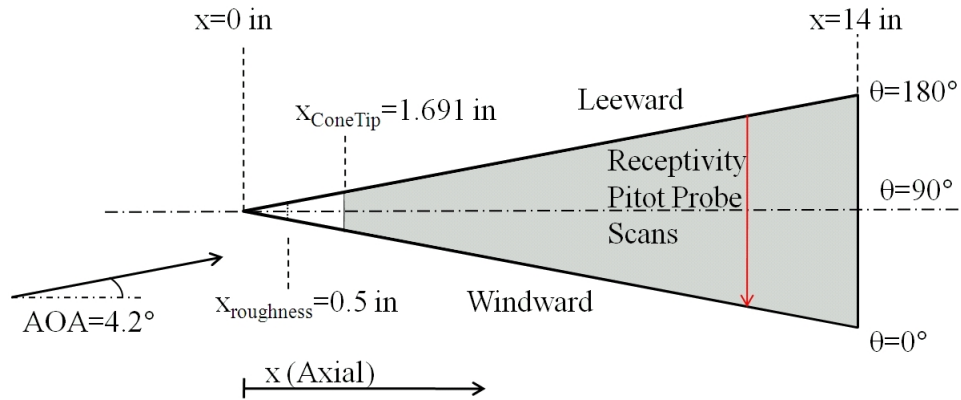


Figure 4.2. Schematic drawing of the cone showing the axial and azimuthal coordinates

analyzed. The filtered and normalized signal is shown at the top of figure 4.3. At second, a fast fourier transform is applied to the entire signal from 110° to 180° to identify which wavenumbers are dominant in the signal. It can be seen that the majority of the energy is contained around a wavenumber of 55. At third, a complex wavelet analysis of the signal is done. In our case, Morlet wavelets were used as shape functions. The wavelet analysis allows to identify when or at which location which wavenumber is present. It can be seen that $m \approx 55$ is present throughout all azimuthal angles. When the $m = 68$ distributed roughness Torlon tip is used, the pattern changes its appearance. The normalized Pitot probe pressure traces are more regular as can be seen in the top graph of figure 4.4. If the FFT analysis over the complete signal from 100° to 180° is done as shown in the middle graph of figure 4.4, a dominant frequency of slightly less than 50 can be seen. At this point the wavelet analysis at the bottom of the figure shows that different frequencies dominate at different azimuthal locations. There is a higher frequency content in the signal from approximately 140° to 180° as

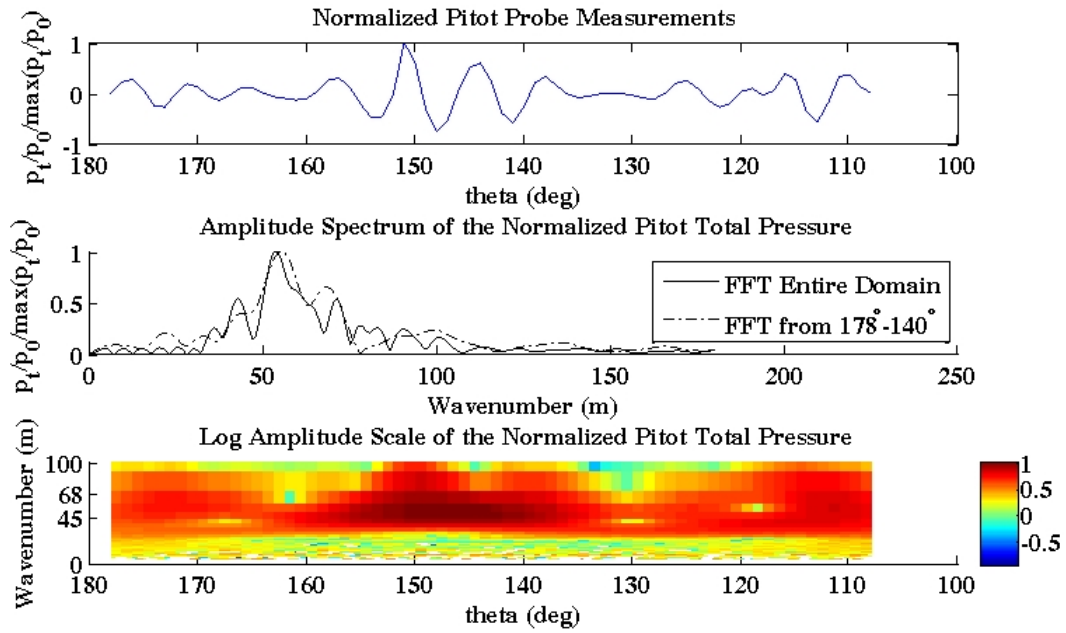


Figure 4.3. Azimuthal scan at 0.0015 in above the surface and $x=11.2$ in with the $m = 0$ tip. Shown at the top is the high pass filtered Pitot probe pressure normalized by its maximum. The middle figure shows the normalized power spectral density (PSD) of the scan. At the bottom of the figure, the normalized power for each frequency at different azimuthal location is shown (wavelets).

recognizable by the higher energy-levels in the wavelet plot. If the FFT analysis is repeated over this range, a wavenumber of 70 appears as dominant frequency. Although a weak peak of $m = 70$ can also be seen in the FFT from 100° to 180° , the amplitudes of the lower frequency content at angles down to 100° overpower the $m = 70$ wavenumber content.

The results of these two measurements indicate clearly that receptivity to the $m = 68$ forcing has happened. The naturally occurring stationary cross flow mode number seems to be as predicted in the numerical stability analysis around

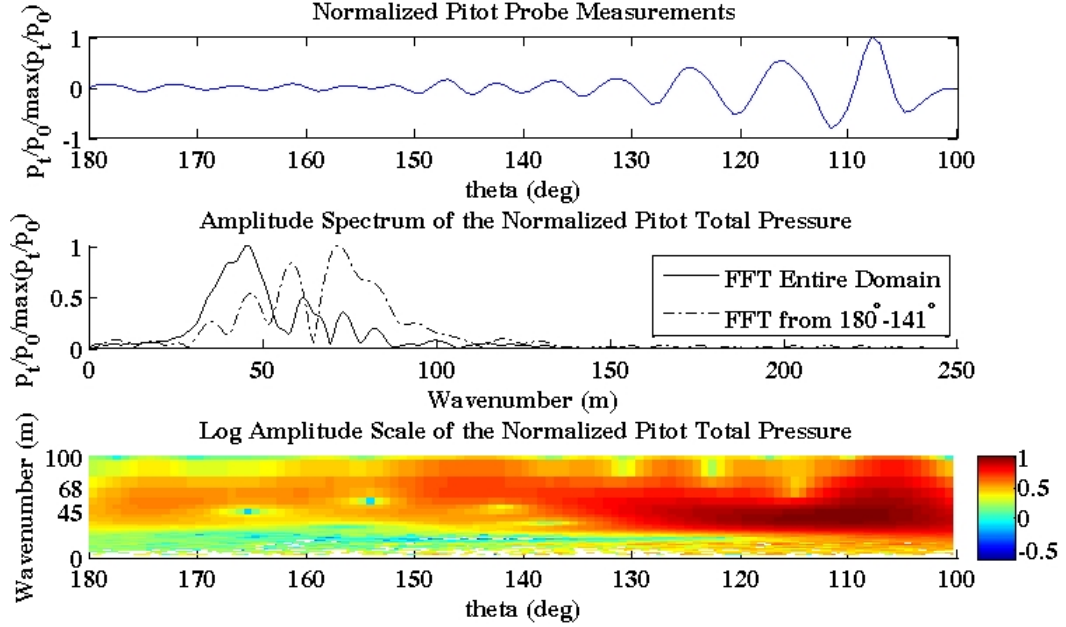


Figure 4.4. Azimuthal scan at 0.0015 in above the surface and $x=11.2$ in with the $m = 68$ tip. Shown at the top is the high pass filtered Pitot probe pressure normalized by its maximum. The middle figure shows the normalized power spectral density (PSD) of the scan. At the bottom of the figure, the normalized power for each frequency at different azimuthal location is shown (wavelets).

$m = 50$. This wavenumber exists for the entire range of the $m = 0$ forcing case and the further windward side of the $m = 68$ forcing case. A wavenumber in the Pitot probe scan of $m = 70$ for the $m = 68$ distributed roughness tips is therefore caused by the used forcing tip. Nonetheless, it seems that the range of where the distributed roughness cone tip changes the mean flow is limited to angles towards the leeward side of the cone. This behaviour might be due to the fact that each cross flow vortex which reaches the far downstream location of the scan has its origin in a certain region of the cone tip and some of them, especially towards

the windward side might not have passed the roughness array at the tip of the cone. A comprehensive investigation of this possibility is done in the following subsection.

4.2.2 Cross Flow Vortex Path

The paths of the stationary cross flow vortices are identified by connecting the appropriate pressure maxima of each azimuthal Pitot probe scan from several axial locations as shown in figure 4.5. The azimuthal pressure scans were done at about 0.0015 in above the surface. A comparison of the cross flow vortex paths obtained

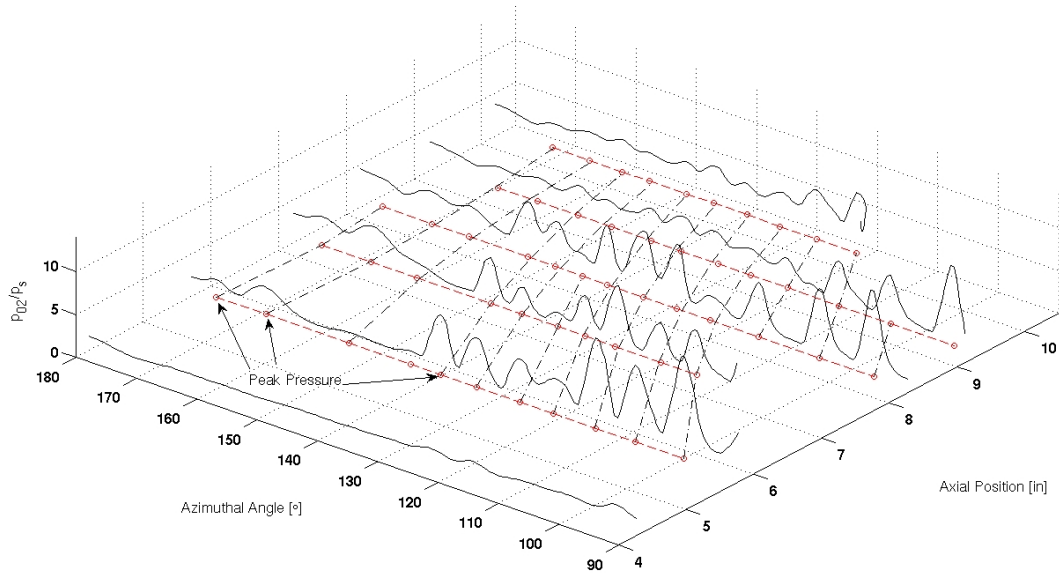


Figure 4.5. Pitot Tube scans at different axial and azimuthal locations at 0.0015 in above the surface for $m = 68$.

from the measurements with the streamlines of the baseflow and the paths of the vortices of Balakumar's DNS calculation are shown in figure 4.6. Over this range

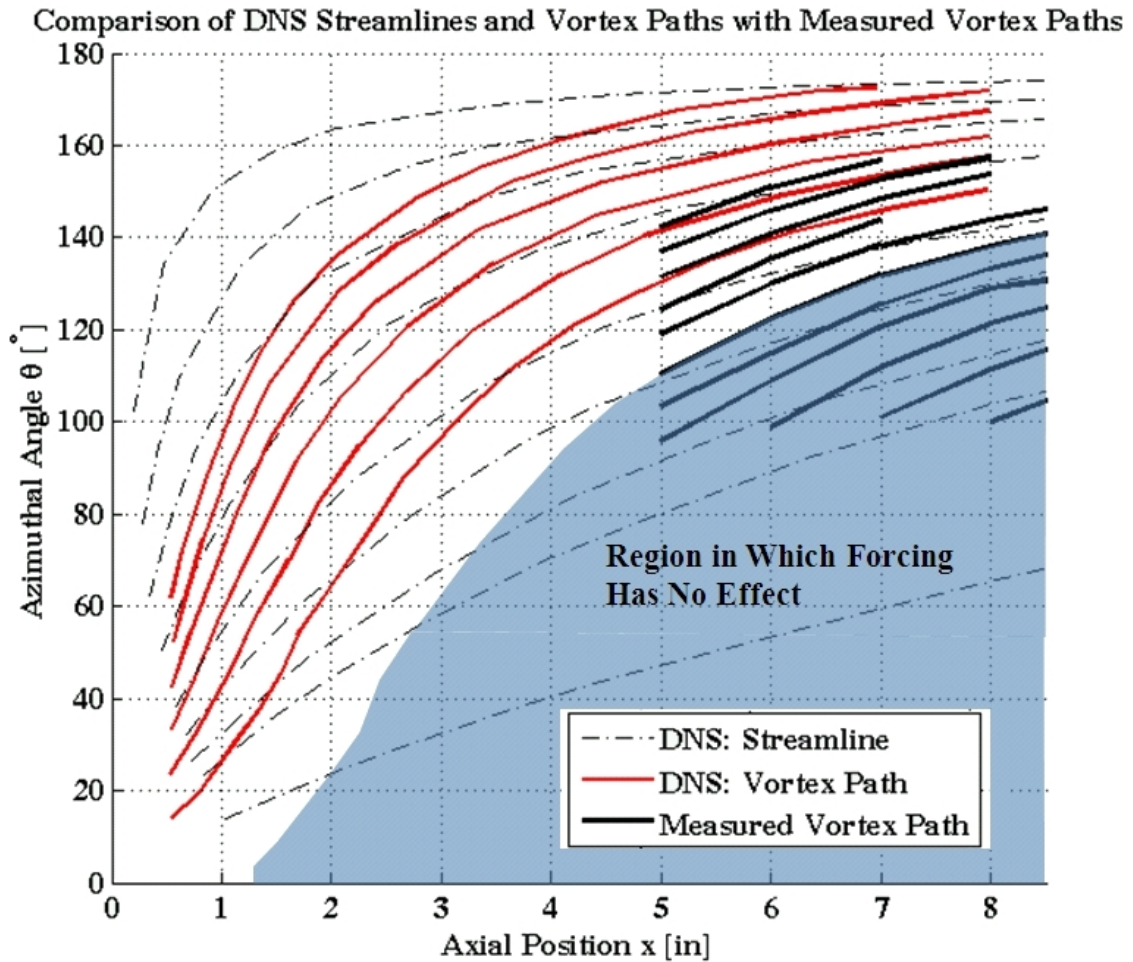


Figure 4.6. Paths of the cross flow vortices of the $m=68$ roughness tip as measured with the Pitot tube in comparison with the surface streamlines of the baseline flow and vortex paths of the DNS calculations with a $m=40$ distributed disturbance at $x=0.5$ in obtained from Balakumar's CFD calculations [3].

of axial locations, the measured and the computed vortex paths agree pretty well. This allows to assume that the computed vortex paths can be used to predict the path of the measured cross flow vortices into regions where no measurements were taken. This is especially interesting for the upstream directions towards the distributed roughness array at $x = 0.5$ in. Most of the vortices which can be found towards the leeward side of the cone have their origin upstream on the windward side of the cone. This was somewhat expected because the cone is mounted at angle of attack which means that the flow stagnates on the windward side of the cone and moves then on curved streamlines on its way downstream towards the leeward side. In order to get an estimate of where an initiated stationary disturbance can affect the downstream flow, the limiting or dividing vortex path line is estimated from the azimuthal Pitot probe scans. As shown in the chapter before, the forcing wavenumber can only be found in a certain range of azimuthal angles. The vortex where the forcing wavenumber transitions to the wavenumber of the unforced flow is then identified as the parting vortex path. This is again done with a wavelet analysis as shown in the bottom graph of figure 4.7. The wavelet transform indicates that the region where the forcing wavenumber of 68 disappears starts around an azimuthal angle of 115 degrees and continues towards the windward side at an axial location of $x = 5$ in. The corresponding parting vortex path and the corresponding region of ineffective forcing is shown in figure 4.6 as shaded area. The extent of the ineffective forcing region is estimated by parallel shifting the most windward vortex path from the DNS simulation until it overlays the measured parting vortex path. Interestingly it points towards an azimuthal angle of 0° close to the forcing location at $x=0.5$ in. This is a very strong hint that the parting vortex line has its origin close to the 0° windward

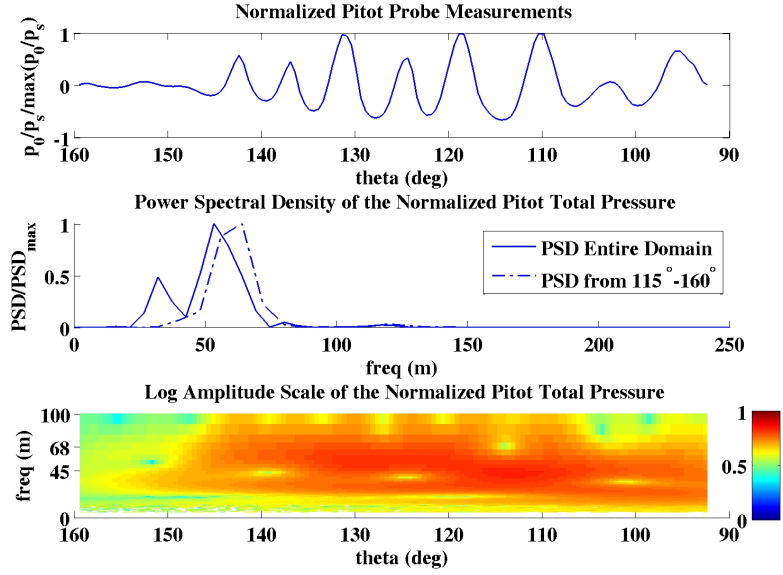


Figure 4.7. Azimuthal scan at $x=5$ in with constant Pitot probe height of 0.05 mm (top). The figure in the center shows the normalized PSD of the Pitot probe scan for the entire domain and the region of passive forcing which is identified in the wavelet plot at the bottom.

side of the distributed roughness array on the cone tip.

4.2.3 Detailed Wavenumber Analysis

Figure 4.6 shows that the paths of the measured stationary cross flow vortices have a certain inclination angle relative to the rays of constant azimuth. This inclination angle is not constant for each axial location which means that if the wavenumber of the stationary vortices is estimated by moving along the azimuthal angle at constant axial location, the wavenumber of the cross flow structure changes with each axial location. This effect is especially significant closer to the tip of the cone where the vortex paths are highly inclined relative to the

constant azimuth rays. The change of the azimuthal wavenumber with increasing Reynolds number from 1.25×10^6 to 1.75×10^6 is shown in figure 4.8. The range of the analyzed azimuthal angles is based on the location of the previously identified parting vortex trace. Each azimuthal pressure trace was additionally padded with zeros to increase the frequency resolution of the fast fourier transform. The

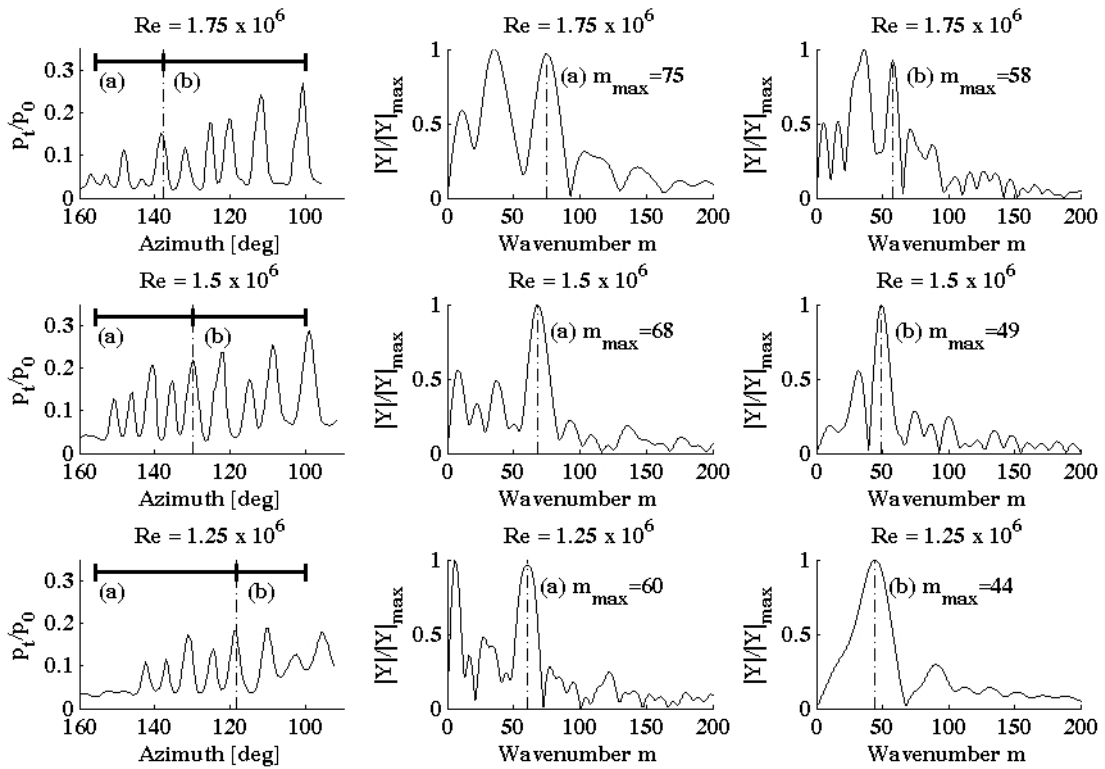


Figure 4.8. Comparison of the dominant wavenumbers with the $m=68$ dimple tip at 25 psia for different Reynolds numbers at 0.05 mm height above surface. There are two azimuthal ranges of the FFT. (a) and (b) correspond to the zones wind- and leeward of the previously identified parting vortex trace.

FFTs of zone (a) in the center column of figure 4.8 show that the highest amplitude wavenumber increases from 60 to about 75 when moving 2 in downstream. This effect is based on the previous observation that the measured vortex paths appear under varying inclination angles relative to the constant azimuth rays. The wavenumber of the excited cross flow vortices will most likely not increase much more further downstream because the vortex paths appear under a shallower inclination angle at higher Reynolds numbers and approach the orientation of the constant azimuth rays. The FFTs of zone (b) in the right hand column show the dominant wavenumbers in the zone which is not affected by the $m=68$ dimples. The wavenumbers are about $m = 16$ smaller than in the (a)-zones and show the same increasing trend with Reynolds number. It shows that the parting vortex trace was identified correctly because there is a distinct difference in wavenumbers between zones (a) and (b).

The increase of wavenumber with increasing Reynold number as initially suspected by looking at the inclination angles of the vortex traces, was clearly identified in the spectral analysis of the measured pitot probe traces. The reason for that might be nonlinear interactions of the stationary modes, generating higher wavenumber modes as consequence. This effect was shown in Saric's low speed cross flow measurements, where initially excited stationary cross flow modes would generate superharmonics with higher wavenumbers but never longer wavelength subharmonics.

4.2.4 Repeatability

Besides the wavenumber fingerprint of the used cone tip, repeated measurements of azimuthal pressure distributions were done as shown in figure 4.9. The

basic idea is that the initial amplitudes generated by the dimples are far stronger than the disturbances initiated by random surface roughness. Thus, in cases where the modenumber is fixed by forcing, the amplified cross flow vortices should be located at some fixed location on the surface of the cone. Exactly this can be seen on the right hand side of figure 4.9. The repeated pressure measurement at the same locations gave identical results for two different runs, even with a tunnel shutdown between them. No locking-in of the cross flow pattern could be seen for the unforced smooth cone tip (left hand side of figure 4.9). Most likely very small changes of the local shape of the cone tip surface lead to the change of the cross flow pattern. This could have been caused e.g. by little dust particles accumulating on the surface or other random events. The forced cross flow vor-

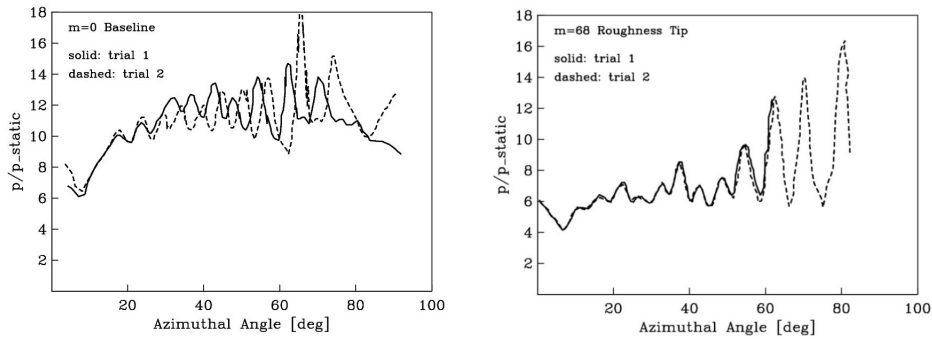


Figure 4.9. Repeated measurements of azimuthal pressure distributions at constant axial position. The left hand side shows the non-repeatability for the smooth tip and a well repeatable pattern for the $m = 68$ tip.

tices are not only spacially fixed for repeated runs but also when the free stream

stagnation pressure is changing. Figure 4.10 shows Pitot probe scans at constant azimuthal angle on traves in axial direction. The normalized pressure amplitudes for all three free stream stagnation pressures are different but almost all peaks and minima are at the same location. These peaks and minima are attributed to cross flow vortices which cause a thickening and thinning of the boundary layer. Hence the spacial location of the vortices did not change with changing free stream unit Reynolds number when forced with the $m = 68$ tip.

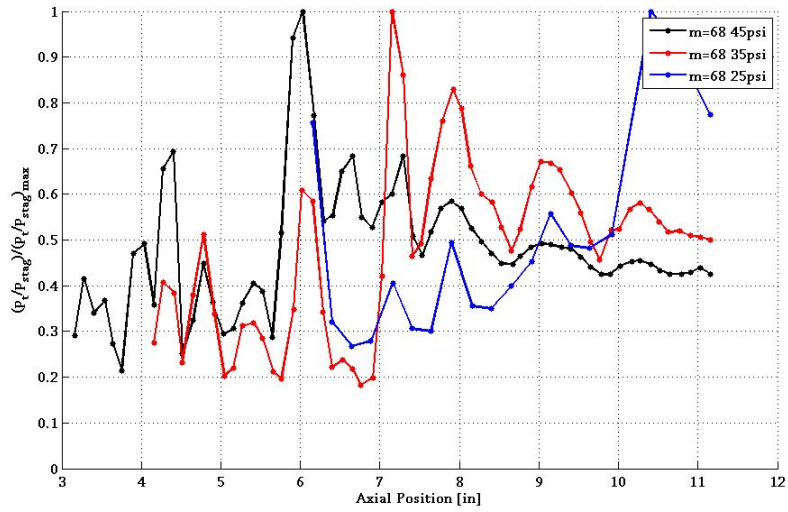


Figure 4.10. Pitot probe measurements at constant azimuthal angle and three different free stream unit Reynolds numbers:
 $Re_{25psi} = 0.25 \times 10^6 in^{-1}$, $Re_{35psi} = 0.35 \times 10^6 in^{-1}$ and
 $Re_{45psi} = 0.45 \times 10^6 in^{-1}$.

4.3 Transition Front Detection

Because the range of motion for the pitot probe is limited from about 3 in to about 10 in transition needs to occur within this range to be documented with mean flow measurements. Using the flow visualization pictures from figure 4.1, a tunnel stagnation pressure of 45 psi was chosen because transition seemed to have happened in the visible range from 11 *in* to 14 in downstream of the cone apex. At first Pitot pressure measurements were taken on the surface of the cone in order to map the development of a few cross flow vortex structures on their way downstream (similar to Figure 4.5) through the regions of maximum cross flow activity as obtained from Balakumar's CFD solutions [3]. The azimuthal Pitot probe scans for the transition front detection are done by moving the Pitot probe to the surface of the cone which is different from the receptivity measurements where the Pitot probe was kept at a constant height above the surface. By being as close as possible to the surface, the measured pressures can be related to regions of high and low shear stress of the boundary layer. Details about the so called Preston probe measurements are given later in this section. Figure 4.11 shows the Pitot data for seven different axial positions ($1.7 \times 10^6 \leq Re_x \leq 3.5 \times 10^6$) and azimuthal angles covering approximately 20° . The space in between each axial position is interpolated to underline the evolvement of the vortices. The height and coloring of the 3-D plots represent the total pressure normalized with the stagnation pressure of the wind tunnel. The interpolation involves three steps. Each pressure maximum of the azimuthal scans at each axial position is assigned to a certain CF vortex. This is the step where CF traces are identified from the azimuthal scans. Then a linear interpolation is used to transform the location of the maxima of each azimuthal scan to the same location as the starting angles

of their respective arbitrarily chosen reference CF vortex. If the maxima of each cross flow vortex are aligned a 2-D interpolation in axial direction is performed. Finally the whole 2-D field is back-transformed so that the original spacing between the maxima are restored. The points from the 2-D interpolation in between each axial location are back-transformed according to a third order polynomial fit to the interpolated cross flow vortex traces in axial direction.

There are three major pieces of information which can be extracted from figure

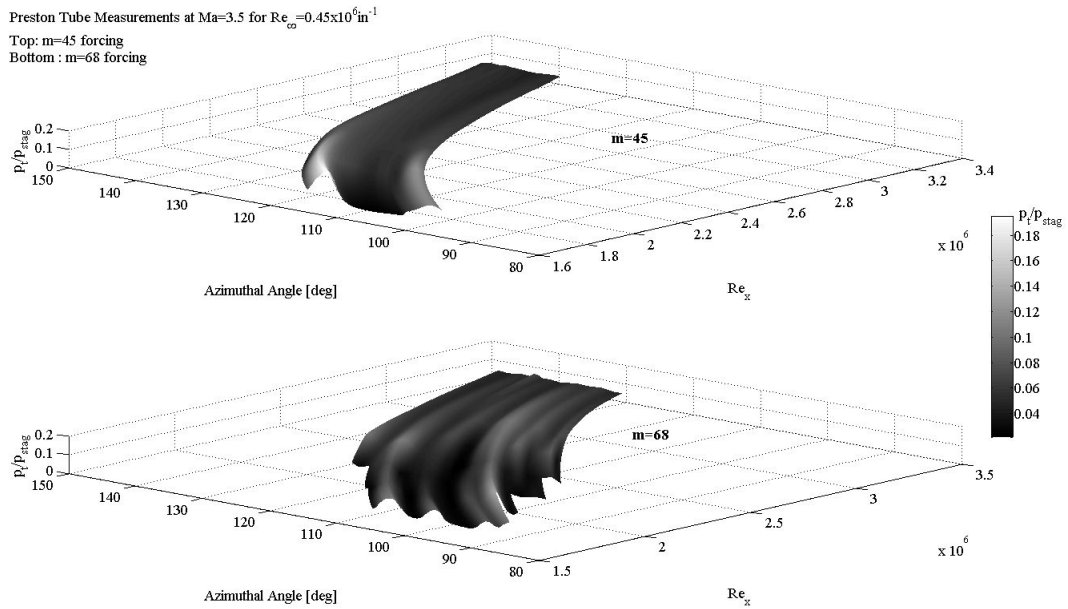


Figure 4.11. Preston Probe measurements for $m = 45$ (top) and $m = 68$ (bottom) forcing at $Ma = 3.5$ and a freestream unit Reynolds number of $0.45 \times 10^6 \text{ in}^{-1}$. The heights correspond to the normalized total pressure at the probe tip.

4.11. These are the approximate wavenumbers of the mapped vortical structures, the amplitudes of the measured stagnation pressures of the CF vortices and their paths. Assuming that one CF vortex extends in azimuthal direction from one pressure peak to another (minimum BL thickness to minimum BL thickness), the $m = 45$ forcing case shows a vortex corresponding to a local wavenumber of $m \approx 26$. The $m = 68$ forcing case results in a wavenumber of $m \approx 51$. Although the measured wavenumbers are lower than the forced wavenumbers, the ratio of both cases is roughly maintained and the wavenumber increases further downstream as shown before with the $m = 68$ dimple tip at $p_0 = 25$ psi. A comparison of the amplitudes of both cases makes it obvious that the vortical structures of the $m = 45$ forcing case decay quickly on their way downstream whereas in the subcritical forcing case the amplitudes persist over a longer distance. In order to quantify the persistence of the vortices, the azimuthal RMS values for each axial position are shown in Figure 4.12. A decayed vortical structure can be seen as

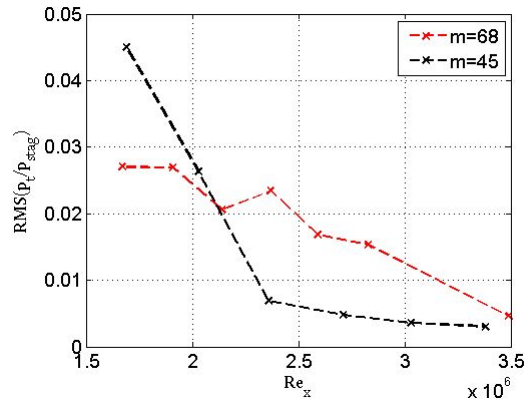


Figure 4.12. RMS values for constant Reynolds numbers from figure 4.11.

an indicator for a boundary layer that transitioned to turbulence. Similar conclusions were drawn from Naphthalene flow visualizations as done by Saric (Figure 1.3). He concludes that if the streaks that represent cross flow vortices disappear, the boundary layer turns turbulent [26],[23]. Assuming that the measured steady structures correspond to stationary CF vortices, transition is completed whenever these coherent structures disappear. Under these assumptions transition is definitely delayed by the $m = 68$ forcing relative to the $m = 45$ forcing reference case. If the RMS value of the $m = 45$ forcing case after the quick decay of the CF vortices is taken as criterion for finished transition, the transition of the $m = 68$ forcing case is delayed by a Reynolds number of almost $Re = 1,000,000$.

Another method to detect transition is also based on Preston tube measurements. King [18] used a Preston probe which was mounted on the surface of a 5° half angle cone at a fixed location and changed the free stream unit Reynolds number in order to change the Reynolds number at the Preston tube. When the transition front moved across the Preston tube a sharp rise of the total pressure at the probe was detected 4.13. Similar data can be extracted from the just described surface Pitot probe measurements with the $m = 45$ and $m = 68$ Torlon dimple cone tips. The main challenge is that there is already a strong mean flow distortion caused by the stationary cross flow vortices. It is therefore not possible to distinguish between an increase of total pressure due to the thickening of the boundary layer and an increase of surface shear stress based on laminar turbulent transition or the presence of a cross flow vortex if scans are done on arbitrary traces, e.g. on axial rays of constant azimuthal angle. Hence the measured total pressures are compared on traces parallel to the identified vortex traces. The traces are extracted from the interpolation procedure in figure 4.11 and are shown in figure 4.14. A

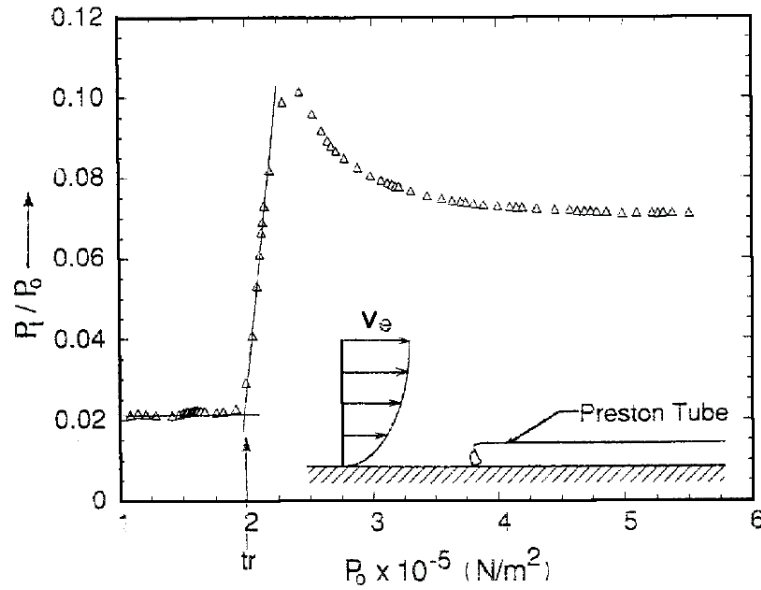


Figure 4.13. Preston probe method showing sharp rise in measured total pressure with increasing free stream Reynolds number at location of transition onset. The measurements were taken in the NASA Mach 3.5 SLDT with $T_0 = 100$ F. Figure is taken from [18].

comparison of the total pressures which are normalized by the total pressure in the settling chamber to the same values in King's paper [18] shows that his transition criterion must have been based on the total pressure in the low pressure region of the mean flow which is about 0.02. This corresponds in our measurements to the thick boundary layer part of a stationary cross flow vortex. The extracted pressure traces are shown in figure 4.15 for the $m = 45$ case and figure 4.16 for the $m = 68$ case. The shown traces are centered in between two maxima of the normalized Preston probe measurement. Each trace in the $m=45$ case starts at low normalized pressures around 0.022 and rises quickly to a certain peak value that is about three times larger than the starting value. After that, the normalized pressure falls off slowly. A first order polynomial is fitted to the part of the pres-

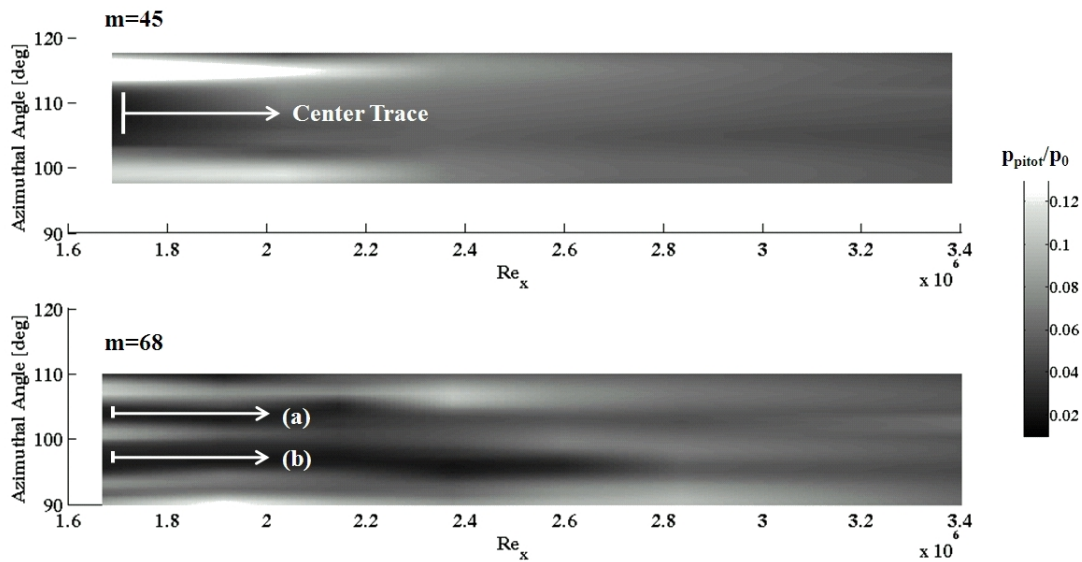


Figure 4.14. Straightened Preston probe scans showing the normalized total pressures and paths of the analyzed pressure traces for the detection of laminar-turbulent transition. $p_0 = 45$ psi

sure signal which exhibits the fastest rise. The location where the fitted curve and the pre laminar-turbulent transition pressure intersect is defined as the turbulent transition Reynolds number in a very similar manner to King's approach as shown in figure 4.13. The pre laminar-turbulent transition pressure of the $m = 68$ tip is estimated by averaging all pressures before the onset of the rising pressure. Black dash-dotted lines in figures 4.15 and 4.16 show the interval where 95 % of that pre-transition values lie within. The pre-transition pressure for the $m = 45$ tip is chosen to be the lowest measured pressure of the shown pressure traces. This is done because the measurement does not extend far enough upstream to capture the leveled pre-transition pressure. It is then assumed that the uncertainty in the estimated pressure is the same as for the $m=68$ case. Figure 4.15 shows besides the mean laminar turbulent transition Reynolds number also the variation of it for

the lowest and highest estimate around the center location. It ranges from 1.61 million (a) to about 1.71 million (c) with a mean value of 1.67 million (b). The

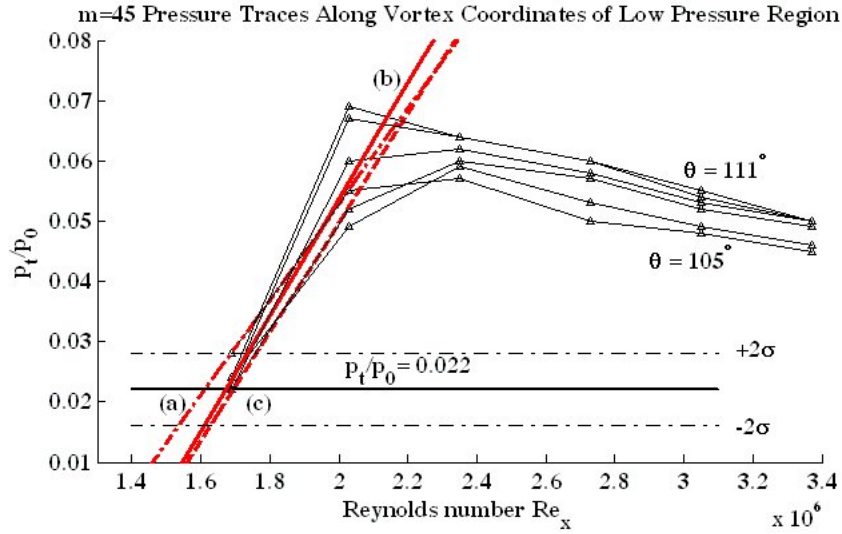


Figure 4.15. $m=45$ normalized pressure traces parallel to the cross flow vortex structure. The traces are azimuthally centered in the middle between the two visible pressure maxima. They are shown for every 0.5° and cover approximately 6° from 105° to 111° in azimuthal direction. The angles refer to the initial angle where the measurement was started for each trace. The dashed red line is a linear curve fitted to the slope of the pressure signal before it levels out. The intersection with the $p_t/p_0 = 0.022$ is defined as laminar turbulent transition onset.

azimuthal spacing between each axial pressure trace is 0.5° . Because the spacing between the CF vortices is smaller in the $m = 68$ wavenumber case, less traces can be taken to calculate the mean laminar turbulent transition location for one single CF vortex. Again, several traces for the two different azimuthal starting

angles (a) and (b) are shown for the $m = 68$ case in figure 4.16.// In order to be

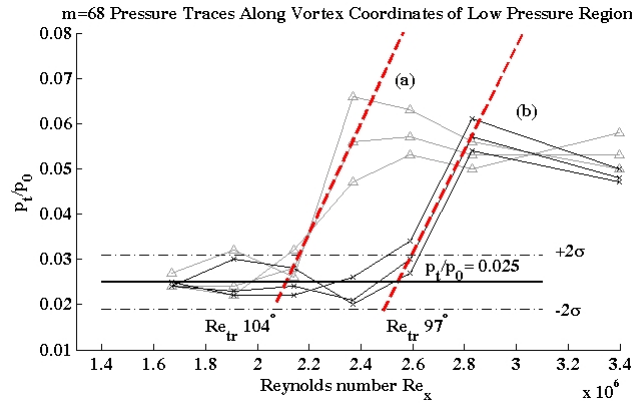


Figure 4.16. $m = 68$ normalized pressure traces parallel to the cross flow vortex structure. There are two low pressure regions (a) and (b) for which the transition Reynolds number Re_{tr} is estimated. The angles correspond to the initial angle where the measurement of the traces was started.

able to directly compare the transition locations for the $m=45$ and $m=68$ tip, the axial laminar turbulent transition location and the corresponding cross flow vortex trace is shown in figure 4.17. It can be seen that laminar-turbulent transition over the range of measured angles is delayed by a Reynolds number of 400,000 to approximately 800,000 depending on which locations are compared. The location of turbulent transition moves upstream when moving to larger azimuthal angles as already seen in previous cone transition measurements. The amount of data is not large enough to compile a complete transition front but nonetheless the result shows that the location of laminar-turbulent transition was moved downstream

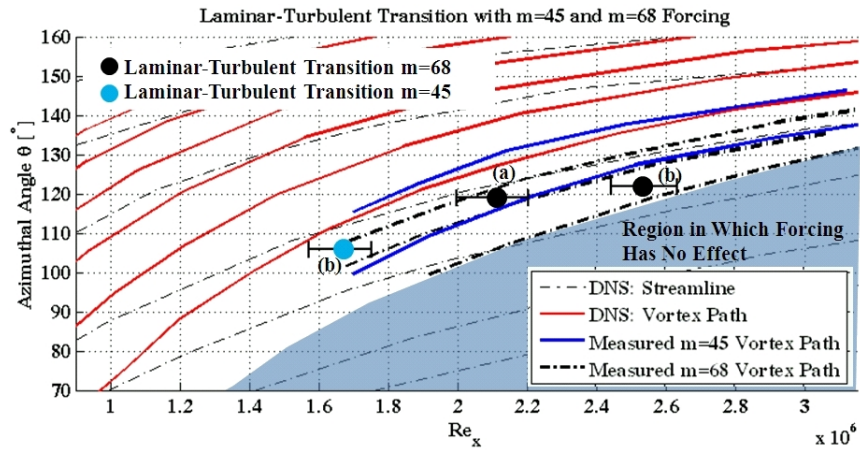


Figure 4.17. Shown are the laminar-turbulent transition locations for the $m = 45$ and $m = 68$ distributed roughness tips including error bars. The black circular dots (a) and (b) correspond to the traces in figure 4.14 with $m = 68$ forcing. The blue dot corresponds to the location identified in figure 4.15 with $m = 45$ forcing.

with subcritical forcing by a minimum of 25 %.

Figure 4.17 includes error bars which are based on the uncertainty of the estimated pre-transition pressure measurement as shown in figures 4.16 and 4.15 as well as on the range of possible transition locations as based on the different pressure traces for trace (a) or (b).

A more complete picture of the expected laminar turbulent transition front is shown in King’s 1991 paper. As described before, transition to turbulence happens further upstream towards the leeward side and further downstream on the windward side. A comparison with Balakumar’s N-factor calculations gives a similar picture for the windward side transition front but not for the leeward side. N-factors of the stationary and travelling cross flow instability become smaller when moving towards the leeward ray at 180° , suggesting that transition to turbulence caused by cross flow instabilities starts first around azimuthal angles of

130°. The discrepancy between the actually measured transition fronts by King and Balakumar's N-factor calculations close to the leeward side at 180° is most likely due to the fact that not the cross flow instability but some other inviscid instability is responsible for laminar turbulent transition.

In order to project the laminar-turbulent transition front of the conducted experiments to higher azimuthal angles, the N-factor at the measured laminar-turbulent transition location is estimated from Balakumar's N-factor calculation and defined as the transitional N-factor. The projected laminar-turbulent transition front for the $m = 45$ and $m = 68$ case based on Balakumar's N-factor calculations is shown in figure 4.18.

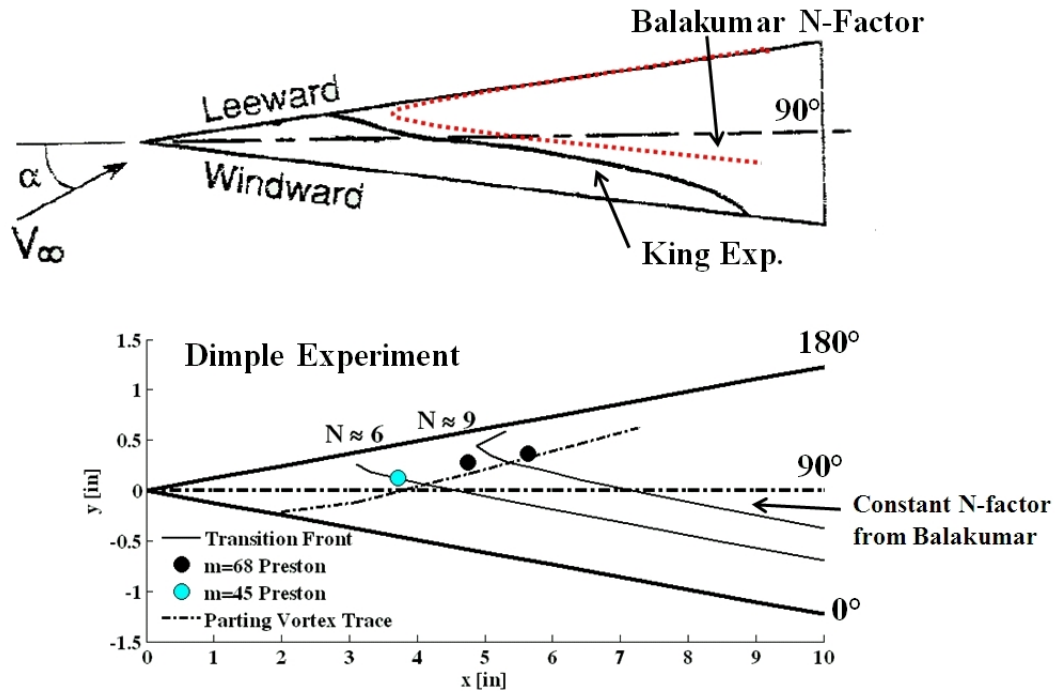


Figure 4.18. The top figure is adapted from King [18] and shows the qualitative shape of the transition front. Added to that is the shape of the transition front based on Balakumar's linear stability analysis [3]. A N-factor of 11 is assumed at the onset of laminar turbulent transition. The bottom figure shows the results of the Preston probe measurements including curves of constant N-factors which pass through the location of the measured onset of transition to turbulence. These correspond to $N \approx 6$ for $m = 45$ and $N \approx 9$ for $m = 68$.

CHAPTER 5

MEASUREMENTS DBD PLASMA ROUGHNESS CONE TIP

The two main objectives of the preceding experiments with distributed roughness cone tips were to show receptivity of the stationary cross flow instability to the applied forcing and that subcritical forcing delayed the onset of laminar turbulent transition. In the next step, the distributed roughness element tips are replaced by the described DBD plasma actuator array tips. Again, $m = 68$ as subcritical wavenumber and $m = 45$ as critical or most amplified wavenumber were chosen for the design of the DBD plasma array cone tips.

5.1 Pitot Tube Surveys: Receptivity to Forcing Wavenumber

The most important part is to show receptivity of the cross flow instability to forcing with a DBD plasma actuator array. For this purpose, azimuthal scans at various constant axial locations were done with a Pitot probe at 0.04 mm above the surface. Based on Balakumar's DNS simulations of the boundary layer, the Pitot probe height is within the boundary layer thickness (0.02 - 0.03 in). The azimuthal scans were done at a total pressure of 25 psia at five different axial locations from 5 in to 9 in in 1 in steps. For each tip, plasma on and plasma off cases are compared. An overview in axial versus azimuthal coordinates for the $m=45$ tip is shown in figure 5.1 and for the $m=68$ tip in figure 5.2. There are two things which

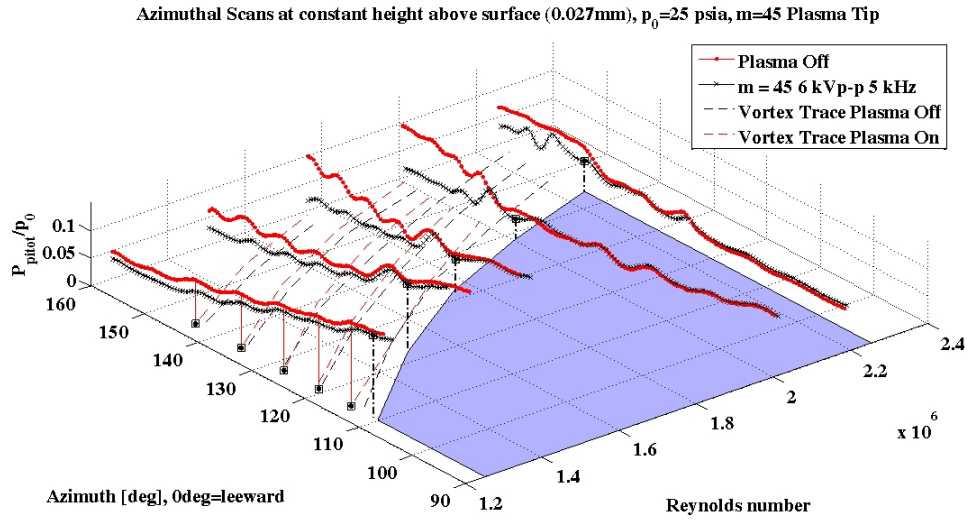


Figure 5.1. Pitot probe traces at 0.027 mm height above the surface for multiple axial locations at 25 psia and $T_0 = 100$ F with the $m=45$ DBD plasma cone tip. Also shown are the vortex traces with plasma on and off as dashed lines. The blue area corresponds to the zone where forcing at 0.5 in has no influence (from figure 4.6.)

become immediately obvious. At first, the plasma on cases cause a significant change of the mean flow profile. Compared to the measured baseline case there is a stronger periodic change of the pitot pressure, indicating that stationary cross flow modes of larger amplitude are generated. At second, the azimuthal range where the plasma on and the baseline cases converge to the same profile is almost exactly where the parting vortex path between effective and ineffective forcing was found in the distributed roughness cone tip measurements. To answer the question if the boundary layer was receptive to the input wavenumber of the DBD plasma actuator, the spacing of the pressure maxima for each case are compared. It has to be shown that the wavenumbers between the plasma on and off cases of the $m = 45$ and $m = 68$ are different. If that is the case, the DBD plasma caused the

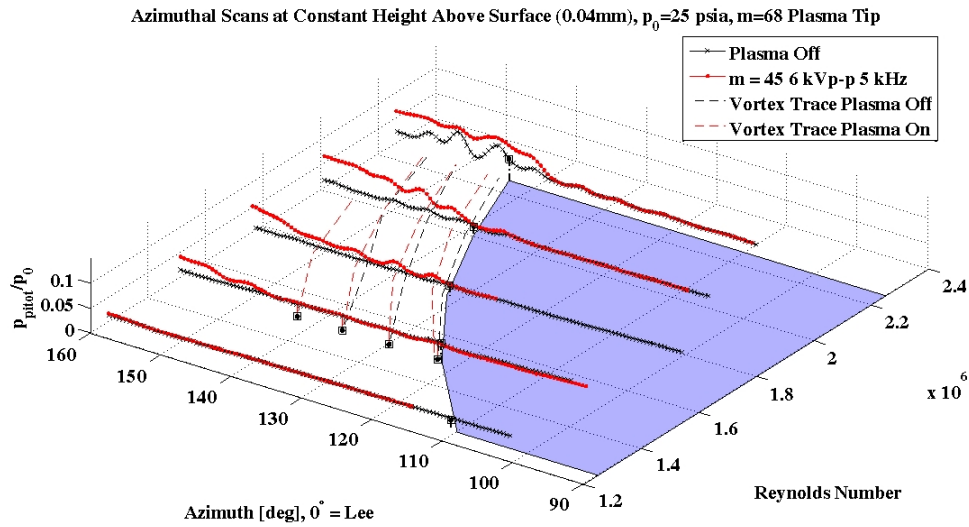


Figure 5.2. Pitot probe traces at 0.04 mm height above the surface for multiple axial locations at 25 psia and $T_0 = 100$ F with the $m=68$ DBD plasma cone tip. Also shown are the vortex traces with plasma on and off as dashed lines. The blue area corresponds to the zone where forcing at 0.5 in has no influence (from figure 4.6.)

presence of stationary cross flow vortices with different wavelengths. Figures 5.3 and 5.4 show the azimuthal Pitot probe traces at $Re_x = 1.5 \times 10^6$ with plasma on and off for the $m = 45$ and $m = 68$ DBD plasma tips. Figures 5.5 and 5.6 are the corresponding figures for $Re_x = 1.75 \times 10^6$. These two Reynolds numbers were chosen to ensure that there is enough azimuthal range with moderate undulations for the following frequency analysis. Especially the $m=68$ case shows only very weak modulations of the pressure signal in the baseline case and plasma on case at $Re_x = 1.2 \times 10^6$. The top part of the following figures shows the measured pressure trace and the bottom part displays the fourier transform of the pressure scan over the azimuthal range which is marked white. The blue area corresponds roughly to the location of the parting vortex line which was indentified earlier. The FFT

is applied to the normalized pressure signal with its mean removed. There is a strong low wavenumber content in the amplitudes of the transformed signal which is caused by the change of the overall measured pressure with azimuthal location. The most dominant wavenumber in terms of amplitude besides the low frequency content below $m=30$ is identified as the wavenumber of the visible undulations in the pressure scans. The raw signal was in some cases truncated towards the leeward angles to remove parts where the signal had no visible modulation. The frequency resolution of the fourier transform is increased by padding the raw signal with zeros.

It can be seen that the wavenumbers for the $m = 68$ plasma on cases are by about $m = 10$ larger than the reference plasma off case for both shown Reynolds numbers. The comparison between the plasma on and off case of the $m=45$ plasma cone tip shows that the wavenumber is slightly reduced relative to the baseline case. The behaviour is exactly as expected with subcritical and critical forcing. The forcing wavenumber is in case of subcritical forcing larger than the naturally most amplified wavenumber which should cause a shift to higher wavenumbers when the plasma array is activated. In case of the critical forcing wavenumber on the other hand, the most amplified wavenumber or a wavenumber very close to the most amplified wavenumber is excited. This leads, if at all, to a small shift of the forced wavenumber which could be observed in these comparisons between the $m=45$ plasma on and off cases. Interestingly, the baseline wavenumbers of the plasma off cases are not the same for both used cone tips. They are consistently higher for the $m=45$ plasma cone tip than for the $m=68$ plasma cone tip which means that passive roughness due to the deposited electrodes is not the reason for the difference. If it was the periodic electrode roughness that induced the

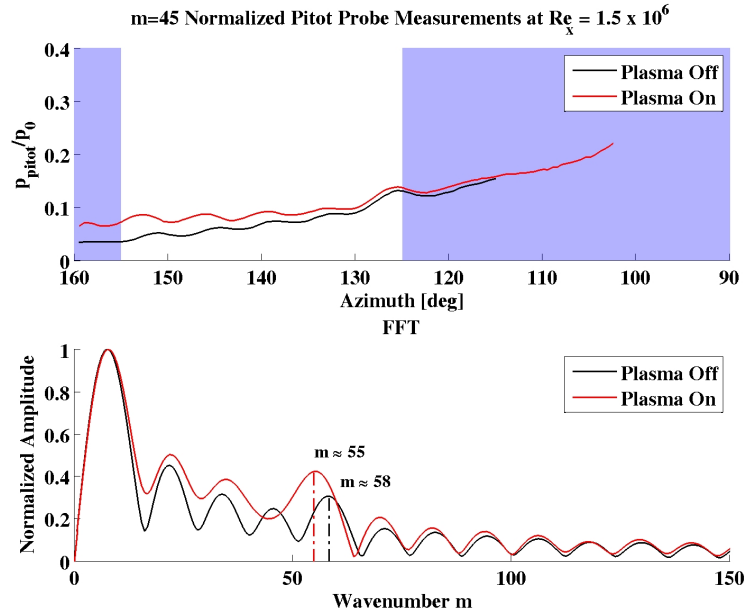


Figure 5.3. Shown are azimuthal pitot probe scans at constant height and $Re_x = 1.5 \times 10^6$ on the $m = 45$ DBD plasma cone tip. The white area in the top plot corresponds to the range of azimuthal angles where the FFT analysis of the bottom plot is done.

baseline difference, the detected wavenumbers should have been higher for the $m=68$ plasma cone tip. Instead, an increase of the measured wavenumber of the baseline and plasma case can be observed when the wavenumbers at the two axial locations are compared. The increase of wavenumber when moving downstream is exactly the same effect as shown with the dimpled tips.

The dominant wavenumbers are summarized in table 5.1.

Another effect that can be seen with running plasma is that the azimuthal location of the pressure maxima shifts when the plasma is turned on. This means that the origin of the cross flow vortices moved to the new locations of initial disturbances which were generated by the DBD plasma discharge.

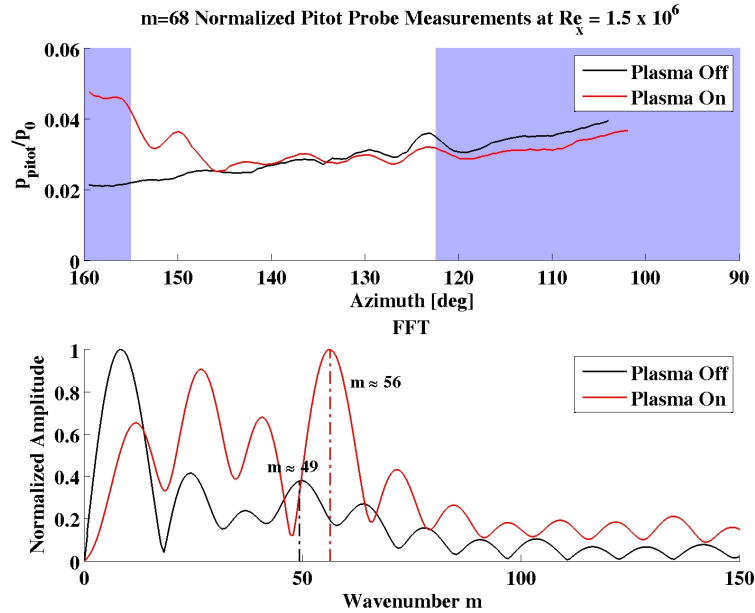


Figure 5.4. Shown are azimuthal pitot probe scans at constant height and $Re_x = 1.5 \times 10^6$ on the $m=68$ DBD plasma cone tip. The white area in the top plot corresponds to the range of azimuthal angles where the FFT analysis of the bottom plot is done.

5.2 Repeatability

To ensure that the measured traces with running plasma actuators were not the result of some randomly changing process during receptivity, repeated azimuthal pitot probe scans were done with a complete tunnel shutdown in between. The result of the repeated Pitot pressure scans with running plasma is shown in figure 5.7. It can be clearly seen that the vortical structures appear for most of the azimuthal angles at the same locations with the same amplitudes in repeated scans. The region where the repeated scans match up perfectly is towards the leeward side of the cone which corresponds to the region that is directly affected by the forcing array at $x = 0.5$ in as identified in the preceding azimuthal pressure

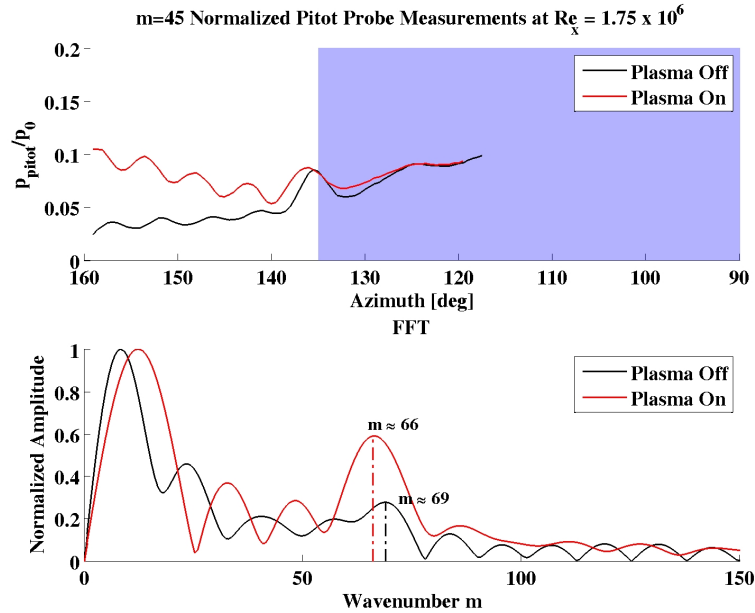


Figure 5.5. Shown are azimuthal pitot probe scans at constant height and $Re_x = 1.75 \times 10^6$ on the $m=45$ DBD plasma cone tip. The white area in the top plot corresponds to the range of azimuthal angles where the FFT analysis of the bottom plot is done.

scans. This means that the stationary modes were locked-in on the stationary disturbances generated by the plasma actuator array at the tip of the cone.

5.3 Initial Amplitudes

In order to investigate the influence of initial amplitude and driving frequency of the DBD plasma on the formation of the stationary cross flow vortices, azimuthal scans at constant height above the surface were repeated at one axial location with different input voltages and AC driving frequencies. Figure 5.8 shows the measured traces at constant height above the surface at an axial location of $x = 8$ in or $Re_x = 2 \times 10^6$. The total pressure is again 25 psia. The voltage was kept

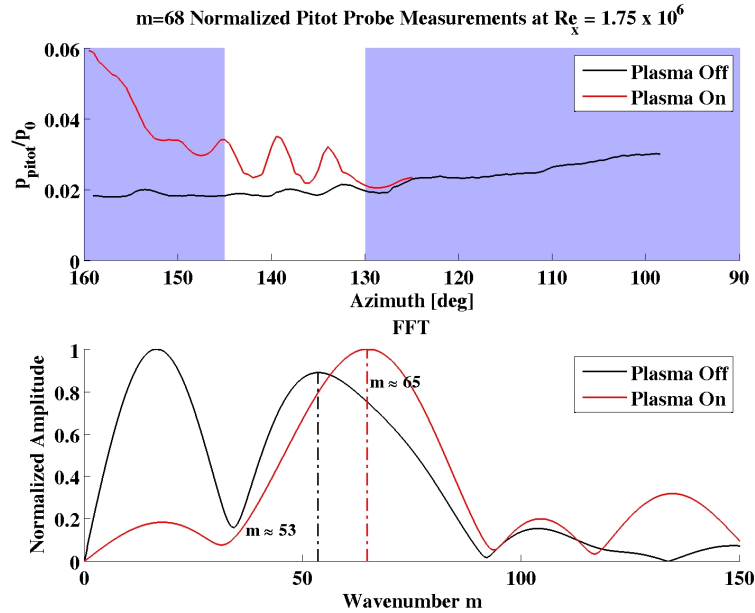


Figure 5.6. Shown are azimuthal pitot probe scans at constant height and $Re_x = 1.75 \times 10^6$ on the $m=45$ DBD plasma cone tip. The white area in the top plot corresponds to the range of azimuthal angles where the FFT analysis of the bottom plot is done.

roughly constant around 5 kVpp and the frequency was increased in 1 kHz steps from 1 kHz to 6 kHz. Amplitudes and the overall pressure level at the Pitot probe increase from 1 to 3 kHz AC driving frequency until they converge to the same azimuthal pressure trace from 4 to 6 kHz. At those saturation frequencies, the location of the cross flow vortex structures is slightly shifted in azimuthal direction. An extra azimuthal pressure trace was taken with 5 kHz AC driving frequency and 2.8 kVpp voltage to investigate the influence of voltage versus AC driving frequency. The azimuthal pressure trace matches almost perfectly the measurements with 5.1 kVpp and 2 kHz driving frequency. It is usually assumed that the frequency has a linear effect on the scaling of the body force whereas the voltage

TABLE 5.1

Summary of the dominant wavenumbers at $Re = 1.5$ and $Re = 1.75$ million.

$Re = 1.5 \times 10^6$	Off	On	$Re = 1.75 \times 10^6$	Off	On
m=68 Forcing	49	56	m=68 Forcing	53	65
m=45 Forcing	58	55	m=45 Forcing	69	66

Repeatability at constant height above surface (approx. 0.2 mm), $p_0=25$ psia, $m=68$

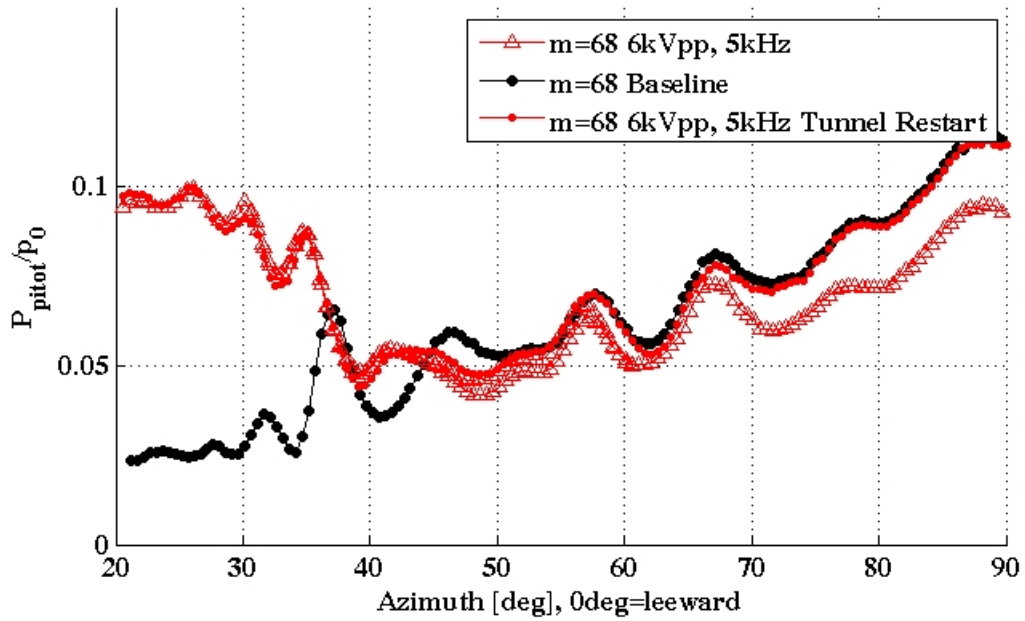


Figure 5.7. Repeated azimuthal pressure scans with plasma on before and after a wind tunnel restart. $m=68$, $p_0 = 25$ psi, $T_0 = 100$ F, $Re_x=2,000,000$

scales the body force by a power of 3.5 in atmospheric pressure and approximately 2.4 in 1/10 atmosphere ambient pressure [33]. This would mean that an increase

of voltage from 2.8 kVpp to 5.1 kVpp causes an increase of body force by a factor of approximately four whereas an increase of AC driving frequency from 2 kHz to 5kHz would increase the body force by a factor of 2.5. This means that the 2.8 kVpp voltage with 5 kHz AC driving frequency asserted roughly 2/3 of the body force on the flow as its equivalent with 5.1 KVpp and 2 kHz AC driving frequency while causing the same response of the boundary layer. This is roughly the same body force and it is therefore very likely that body force scaled the response of the boundary layer and not the proximity of the AC driving frequency to the most unstable frequency of an instationary instability of any kind.

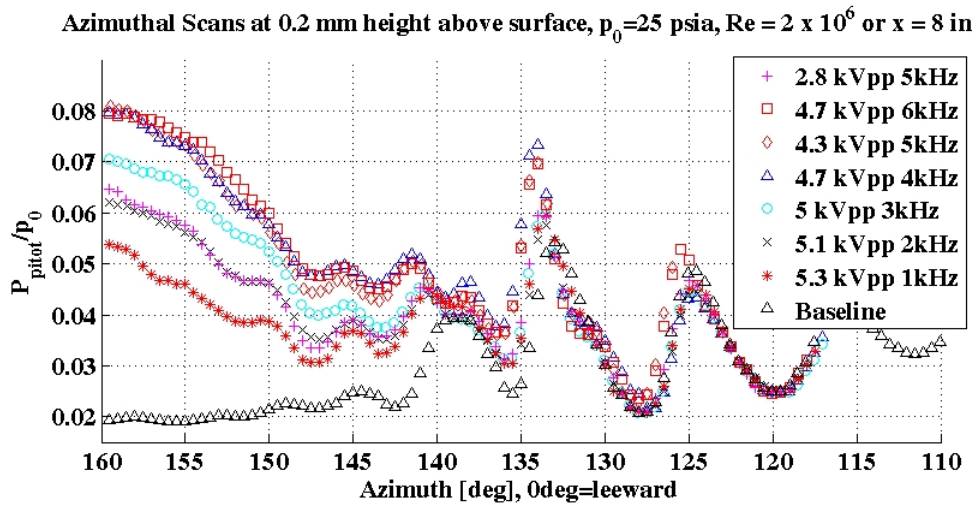


Figure 5.8. Repeated azimuthal pressure scans with AC driving frequencies from 1 kHz to 6 kHz and different voltages. $m=68$, $Re_x = 2 \times 10^6$, $p_0 = 25$ psi, $T_0 = 100$ F

5.4 Comparison with the Dimple Cone Tips

Receptivity to the forced wavenumber could be shown, as proven by the wavenumber analysis of the azimuthal Pitot probe scans and the azimuthal shift of vortex traces relative to the baseline plasma off measurements. However, there are some differences to the forcing cases with the dimpled Torlon tip. One major difference is the overall pressure increase towards the leeward side of the Pitot probe scans when the DBD plasma is turned on. It seems that the high pressure region originates from the leeward side and spreads towards the windward side when moving downstream. If the overall increase of pressure is interpreted as onset of turbulence, it might be that the source of the laminar-turbulent transition is somewhere on the leeward ray at 180° . As shown in Balakumar's N-factor calculations, the leeward side of the cone shows very weak amplification of cross flow instabilities. Instead, the maximum N-factors are expected around an azimuthal angle of 130° which means that CF modes can be excluded as the reason for laminar-turbulent transition. Anyhow, the leeward ray is the location where the fluid from both sides of the cone meet. A thick boundary layer is formed there, which is inflectional further downstream. The introduced forcing by the DBD plasma actuator might have excited instability modes which caused the flow on the leeward ray at 180° to transition to turbulence prematurely. Especially T-S modes are highly sensitive to acoustic free stream disturbances which might have been generated by the plasma AC driving frequency. Frequencies of the fastest growing viscous instability on the same cone at 25 psi at 100° F are in the range of 20 - 30 kHz [19]. It might well be that the unstable frequencies on the leeward side of the cone are lower than that because the flow is more decelerated and the boundary layer is much thicker than on the equivalent cone at zero incidence.

Another difference is the magnitude of the undulations in the azimuthal range windward of the parting vortex trace where the actuator array at $x = 0.5$ in is not effective. It would be expected that relatively large azimuthal variations of the measured pressure signals as with the Torlon tip can also be found in the plasma cone tip case. This does not happen which can be explained with the rms roughness of the cone tip. The Macor cone tip is much smoother than the Torlon cone tip which means that the initial amplitudes of the stationary cross flow vortices are much smaller. The result is stationary cross flow vortices with smaller amplitudes leewards of the parting vortex path in comparison with the Torlon tip case.

CHAPTER 6

CONCLUSIONS

The main objective of this research project was the delay of cross flow instability induced laminar-turbulent transition in a wall boundary layer in Mach 3.5 supersonic flow by using an array of DBD plasma actuators. A 7° half angle cone at 4.2° angle of attack was used in the NASA Mach 3.5 Supersonic Low Disturbance Tunnel to generate a boundary layer which undergoes laminar turbulent transition caused by stationary cross flow instabilities. Stationary cross flow instabilities are at the point of neutral amplification highly sensitive to 3-D surface roughness and dominate in low disturbance flows as generated in the NASA Mach 3.5 SLDT or as can be found in natural free flight environments. Saric was able to show by forcing the stationary cross flow instability with micron size roughness elements at a spacial wavenumber larger than the most amplified wavenumber that the most amplified stationary cross flow waves were completely suppressed and thus laminar turbulent transition delayed. His principle of subcritical forcing is well documented and has been shown to work in subsonic flows. There exists only very little and not completely conclusive data for supersonic flows and is therefore investigated in this work. Hence the logical first step was to document the effect of subcritical forcing with traditional micron sized roughness elements or dimples on laminar turbulent transition and then as second step, to show the

effect of the designed DBD plasma actuator roughness array on the stationary cross flow instability.

6.1 Disturbance Generators

Two Torlon cone tips were used to force the stationary cross flow instability at its critical and subcritical wavenumber of $m = 45$ and $m = 68$. The roughness array consists of about 80 micron deep equidistant dimples located at $x = 0.5$ in downstream from the tip of the cone. The choice of azimuthal spacing as well as the axial location is based on the results of a linear stability analysis of the compressible supersonic flow field of the cone.

Two more cone tips were made of Macor as carrier for the DBD plasma actuator array. The plasma actuator consists of two electrodes which are separated by the Macor dielectric. Special care had to be taken to minimize passive roughness effects caused by the presence of the exposed electrode on the surface of the Macor. By using vapor deposition, an electrode thickness of only 60 nm could be achieved. This is smaller than the rms surface roughness which makes the electrode undistinguishable with the natural background surface roughness. The exposed electrode is shaped like a comb which generates concentrated plasma at each single finger of the pattern. PIV measurements of the plasma generated flow field in quiescent air show that streamwise vorticity as well as a streamwise velocity component with the spacing of the fingers of the comb electrode is generated.

6.2 Receptivity

Receptivity was shown by traversing the boundary layer azimuthally at constant height above the surface at constant axial locations with a pitot probe. The

Pitot probe helps to detect the mean flow distortion which is caused by the stationary cross flow vortices. A cross flow vortex moves low momentum fluid into higher layers of the boundary layer which means that when the streamwise oriented Pitot probe traverses the cross flow vortex, a drop in measured pressure can be observed. The spacing of the minima and maxima of the measured pressure trace can then be directly translated into the wavelength of the stationary cross flow vortices. A comparison between the measured cross flow vortex wavenumbers of a natural roughness tip and the $m = 68$ Torlon dimple tip showed receptivity to the forcing wavenumber. The forced wavenumber was surprisingly only visible towards the leeward side of the cone, as identified with wavelet transforms. This could be explained by tracing the cross flow vortex paths to their upstream origin. The vortex which originates from the windward side at the upstream forcing location moves on its way downstream towards the leeward side. Every vortex towards the leeward side of the so called parting vortex path originates from the upstream roughness array whereas every vortex towards the windward side of the parting vortex path never got in touch with the roughness array.

The stationary cross flow vortices were also receptive to the plasma roughness array. A comparison between plasma on and plasma off cases shows that the wavenumber increases with subcritical plasma forcing relative to the plasma off case. This is expected because subcritical forcing means that the forced wavenumber is larger than the most amplified, naturally occurring wavenumber. The critical forcing case at the most amplified wavenumber leads to a very small shift to slightly lower wavenumbers when comparing the plasma on and plasma off case.

6.3 Transition

The onset of transition had to be estimated from the mean flow properties of the boundary layer. For that purpose, Pitot probe scans were done on the surface comparable to a Preston probe measurement. The challenge with cross flow vortices is that they introduce a strong mean flow distortion which makes it impossible to distinguish between the presence of a cross flow vortex or the increase of shear stress due to the onset of transition. To avoid this problem, Preston probe scans were done along the path of a cross flow vortex. A sudden increase in pressure indicates then the onset of laminar turbulent transition. This method showed that the onset of laminar turbulent transition with subcritical dimple forcing was delayed by a Reynolds number of at least 400,000 or 25% in comparison with the critical forcing reference case. A second criterion based on the disappearance of coherent mean structures in the turbulent part of the boundary layer results in a delayed laminar turbulent transition location of about $Re=800,000$ when comparing the subcritical and the critical forcing case.

Receptivity of the the cross flow instability could be shown to the wavenumber of the BDB plasma actuator array, although the overall pressure levels were raised. This is most likely an effect owed to the thick inflectional boundary layer on the leeward ray that was most likely receptive to the acoustic disturbances generated by the plasma actuator. Nonetheless the earlier decay of the coherent structures in the critical forcing case hint towards a delayed transition with the subcritical plasma forcing.

CHAPTER 7

RECOMMENDATIONS FOR FUTURE WORK

One of the main challenges in the design of the forcing arrays was the size and shape of the cone tip surface. It was extremely difficult to manufacture the DBD plasma actuator array on such a confined space. Standard MEMS techniques were not directly applicable because of the surface curvature. It would be very helpful to move the location of branch I of the stationary cross flow instability further downstream by either running at an even lower free stream Reynolds number or decreasing the angle of attack. This would allow for more space to build the actuator array or in other terms, it would make it possible to confine the plasma more easily to the desired locations by using a larger structure size to dielectric thickness ratio. Circular plasma dots or streamwise plasma vortex generators without a superimposed 2-D streamwise velocity could then be manufactured. However, weakening cross flow might make viscous modes the dominating laminar turbulent transition mechanism or there would be no transition on the cone at all. The details would have to be estimated by a stability analysis of the boundary layer flow. Anyhow, the replaceable cone tip has a total length a about 1.7 in which is again limiting the maximum downstream location of a possible actuator array. A more accessible cone tip would also make it possible to use the same comb actuator design in the opposite direction. The current 2-D component of the actuator adds momentum in upstream direction. If the direction could be reversed

it would blow the 2-D component downstream which might mitigate the effect on the leeward side boundary layer and the observed overall pressure increase.

Another possibility of improving the accessibility of the model for active plasma roughness control would be the usage of a different geometry. One possible model would be a wedge with conical sides. Branch I of the stationary cross flow instability can be found on the flat slope of the wedge and the wavelengths of the most amplified wavenumbers are in the range of millimeters instead of 1/100 of millimeters as in our case.

The spacial limitations as experienced in our experiment are no concern for the application on actual swept wings. The wavenumbers of the most amplified stationary cross flow modes are in the range of millimeters which does not pose any problem for the generation of DBD plasma. The dielectric strength of the used insulating material is also not too much of a concern because the initial disturbance of the Plasma actuator seemed to be sufficient to trigger cross flow vortices as soon as plasma formed on the surface. Therefore, thin dielectrics are sufficient to sustain the actuator. The question might rise if corrosion of the exposed copper actuator is a problem for longer operation in outdoor environments. It might be that the copper corrodes but it can be also manufactured from other, more inert conductive materials like gold or platinum. There is also the possibility to apply a thin protective coating on the entire actuator surface. This would shield the electrodes from environmental effects without overly weakening the DBD plasma on the surface. The actuator would then be a double instead of a single dielectric barrier discharge actuator.

For real time adaption of the forcing wavenumber and forcing location of the Plasma actuator array, separately adressable plasma cells need to be designed.

This could be achieved by supplying separate electrodes with high voltage from one high voltage source. Optically insulated high voltage transistors can be used for that purpose.

Separately adressable arrays of plasma actuators might be also interesting for academic research, especially if the interaction of stationary and travelling waves needs to be observed. Again, the stationary cross flow instability is highly sensitive to surface roughness. If deployable dimples, bumps or vibrating ribbons are used to excite travelling cross flow waves, also stationary cross flow vortices are excited at the same time. A plasma actuator of the kind as used in these experiments is invisible to the cross flow instability when turned off and makes it possible to excite a travelling wave with the desired wave angle and wavenumber without exciting parasitic stationary vortices.

CHAPTER 8

APPENDIX

8.1 Experimental DBD Plasma Body Force Study in Sub-Atmospheric Pressure

Plasma actuators as active flow control devices in the context of laboratory experiments are usually used at atmospheric pressure in air. However, a lot of environments in which the target application of a plasma actuator lies, will be at non-atmospheric pressures. One example is the usage of plasma acutators in compressor stages of a turbine on the high pressure side or the usage of a plasma actuator in low pressure environments like high altitutde flight. The experiments described in this thesis are of course also part of the low pressure experimentation. In order to empirically investigate the effects of sub-atmospheric pressure on the performance of the plasma actuator, thrust measurements in a vacuum vessel at different pressures are done. The results contribute to the understanding of plasma actuators and deliver further input for the numerical modelling of DBD plasma actuators.

The independent variable of the experiments is body force or measured thrust force. Dependent variables are ambient pressure, AC voltage and the amplitude of the input voltage.

8.1.1 Experimental Setup

A standard straight edge DBD plasma actuator was mounted vertically on the weighing pan of a Acculab ALC 320.3 scale with a total range of 320 g and a repeatability of 1 mg. The generated tangential wall jet points away from the scale which means that the plasma actuator pushes on the surface of the force balance. The scale itself was covered with copper tape and electrically grounded to minimize electromagnetic interference between the high voltage wire of the plasma actuator and the scale. The entire setup was situated in a vacuum vessel made of a PVC tube and two endplates. A picture of the entire experimental setup is shown in figure 8.1.

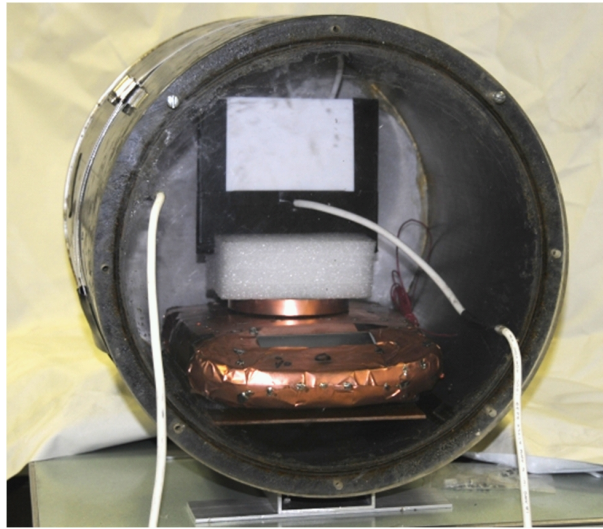


Figure 8.1. Teflon plasma actuator on the shielded force balance inside the vacuum vessel.

8.1.2 Actuator Measurements

Several dielectrics with different thicknesses and electrode widths and spans were used for this study. The waveforms used were ramps and all thrust values are normalized with the width of the electrodes. The first actuator consists of 1/4 in thick Quartz glass with an overlap of 1/8 in and a span of only 2.5 in. The width of the covered electrode is 1 in. The first measurement was a comparison between the measured thrust inside the vacuum vessel and outside the vacuum vessel. Figure 8.2 shows the obtained curves including a fit to the 7/2 power law. It can be seen that there is no difference in between the measurements and that

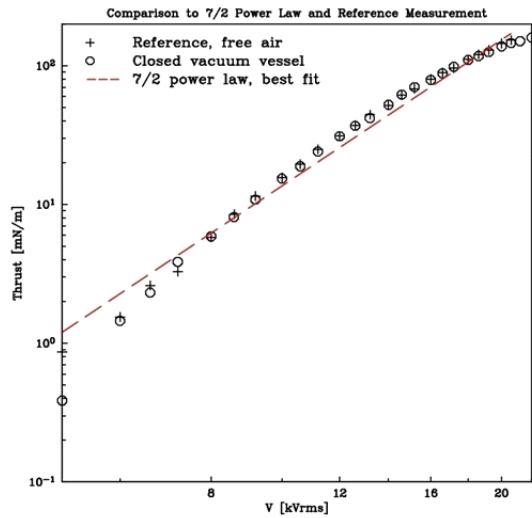


Figure 8.2. Comparison of thrust measurements inside and outside the vacuum vessel.

the data points match the power law relatively well. In the next step, the AC

driving frequency was kept constant at 2 kHz ramps and the influence of ambient pressure on the thrust was obtained. The ambient pressure inside the vacuum vessel was reduced in several steps down to about 8 inHg. For each pressure, the input voltage versus thrust curve was recorded as shown in figure 8.3. The voltages at which the thrust reaches its maximum is coincidental with the formation of filamentary discharges.

A very similar behavior can be seen when the ambient pressure is kept constant

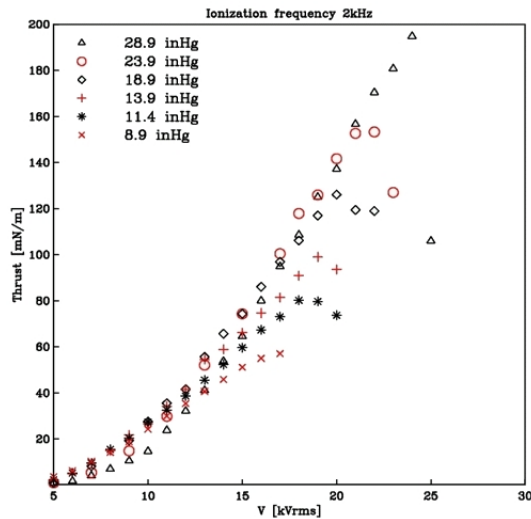


Figure 8.3. Influence of different ambient pressures on the voltage vs. thrust curves. 2kHz ramps.

at atmospheric pressure and the AC driving frequency of the plasma actuator is increased. The thrust increases up to a certain point and falls off quickly. The maximum thrust is reached whenever the plasma discharge shows strong filamen-

tary discharges over the region of the covered electrode. Figure 8.4 shows the measured curves.

Based on repeated measurements with different AC driving frequencies and dif-

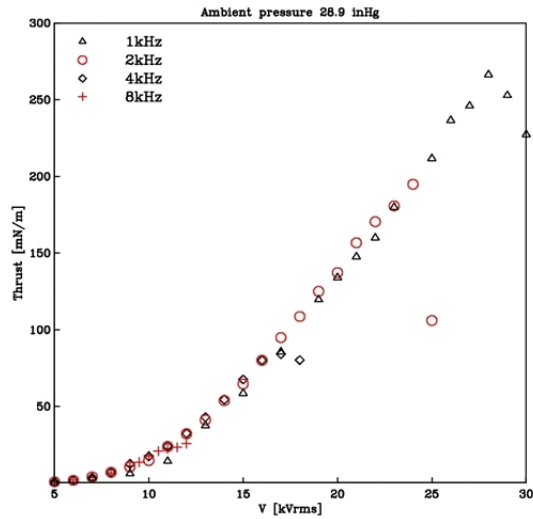


Figure 8.4. Influence of different ambient pressures on the voltage vs. thrust curves. 2kHz ramps.

ferent pressures, a figure of maximum thrust in dependence of ambient pressure and frequency is compiled. The result can be seen in figure 8.5. The maximum pressure is obtained with the lowest AC driving frequency for all tested ambient pressures and decreases with decreasing ambient pressure. Because the thrust is limited by the maximum voltage at which the filamentary discharge occurs, filamentary discharges seem to appear earlier at lower voltages with higher frequencies and lower ambient pressures.

Another interesting question is, how the thrust develops for the remaining part

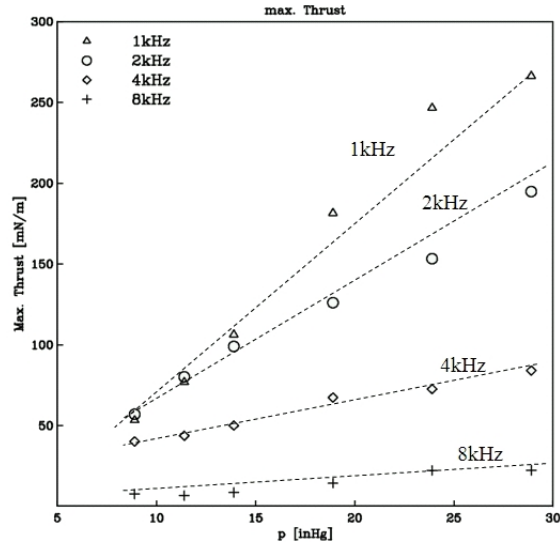


Figure 8.5. Maximum thrust values in dependence of ambient pressure for different AC driving frequencies.

of the voltages, far below the voltage at which filamentary discharges occur. For that purpose, figure 8.6 shows the development of thrust in dependence of the ambient pressure when the amplitude of the applied voltage is kept constant. The interesting observation is, that the thrust increases at when the ambient pressure is reduced and the applied voltage is kept constant. The values shown are just for lower voltages since the data points will reach the filamentary regime earlier towards the lower pressures. This will diminish the just shown effect.

The same effect can be shown when the voltage needed to sustain a certain amount of thrust is plotted versus the ambient pressure. For low values of thrust, the

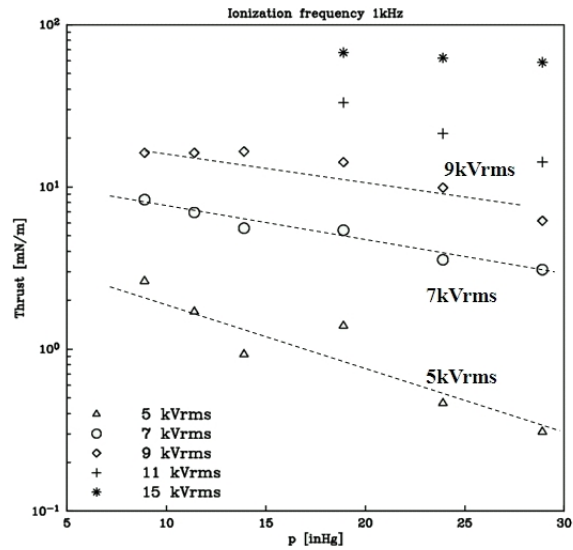


Figure 8.6. Dependence of thrust at constant applied voltage on ambient pressure.

voltage needed to maintain those values goes down with decreasing pressure. If a larger thrust value is chosen, the discharge gets closer to the filamentary regime with decreasing pressure and the voltage necessary to maintain that level of thrust increases.

The final question to be answered is how the AC driving frequency affects the amount of thrust produced with decreasing ambient pressure. For that purpose, figure 8.8 shows again the amount of thrust which is produced by a constant applied voltage at different ambient pressures. This time, the data for 1, 2, 4, and 8 kHz AC driving frequency is shown. As expected, the thrust increases when increasing the AC driving frequency for all shown applied voltage amplitudes in the far pre-filamentary regime. The most notable increase in thrust happens from 1 to 2 kHz. The thrust values for higher frequencies are less distinguishable which might also be a consequence of the logarithmic representation of the data.

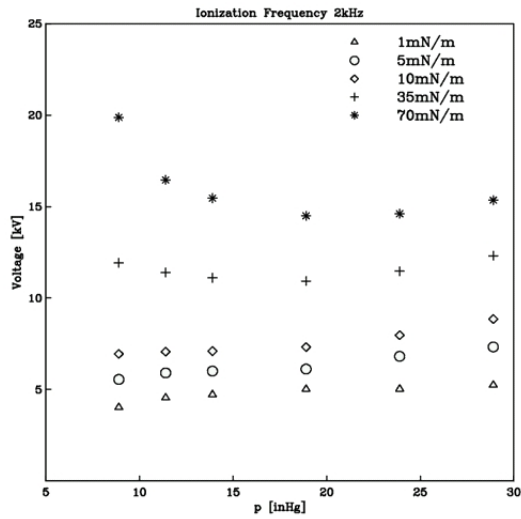


Figure 8.7. Necessary applied voltage to maintain constant body force for different ambient pressures.

There are several trends which can be derived from the data.

1. The maximum thrust is limited by the formation of filamentary discharges.
2. Filamentary discharges happen at lower applied voltage amplitudes for higher AC driving frequencies and lower ambient pressures.
3. The same constant applied voltage amplitude generates more thrust when the ambient pressure is reduced, as long as the voltage amplitudes are in the pre filamentary regime.
4. Increasing the AC driving frequency increases the body force over the entire range of tested pressures.

Finally, the effect of the width of the covered electrode for different AC driving frequencies and ambient pressures is investigated. Two different actuators were used for this purpose. The actuator to investigate the difference between two

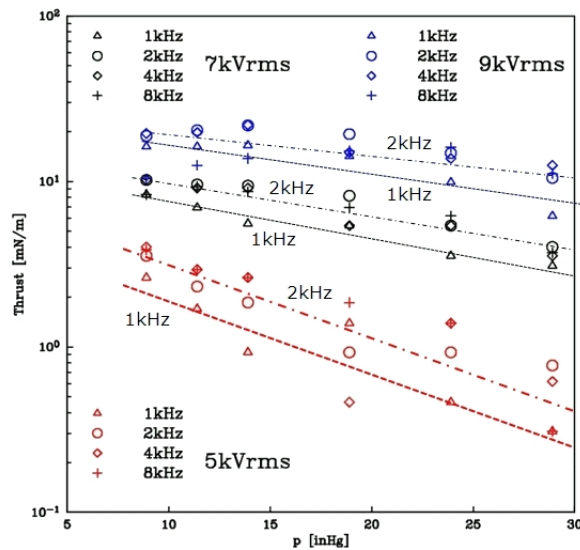


Figure 8.8. Necessary applied voltage to maintain constant body force for different ambient pressures.

different covered electrode widths at different ambient pressures consists of a 1/4 in thick Teflon dielectric with 2.75 in span and 1 in and 2 in wide covered electrodes. The results are shown in figure 8.9 for 2.3 kHz ramps. It can be seen that the thrust for all ranges of pressure is smaller with the 1 in wide covered electrode compared to the 2 in wide covered electrode. The relative difference between the two electrode widths stays almost the same over the entire tested pressure range. The corresponding thrust measurements at constant atmospheric pressure but changing AC driving frequency are shown in figure 8.10. A very similar effect can be seen which shows that the smaller electrode width leads to lower thrust values relative to the 2 in width covered electrode.

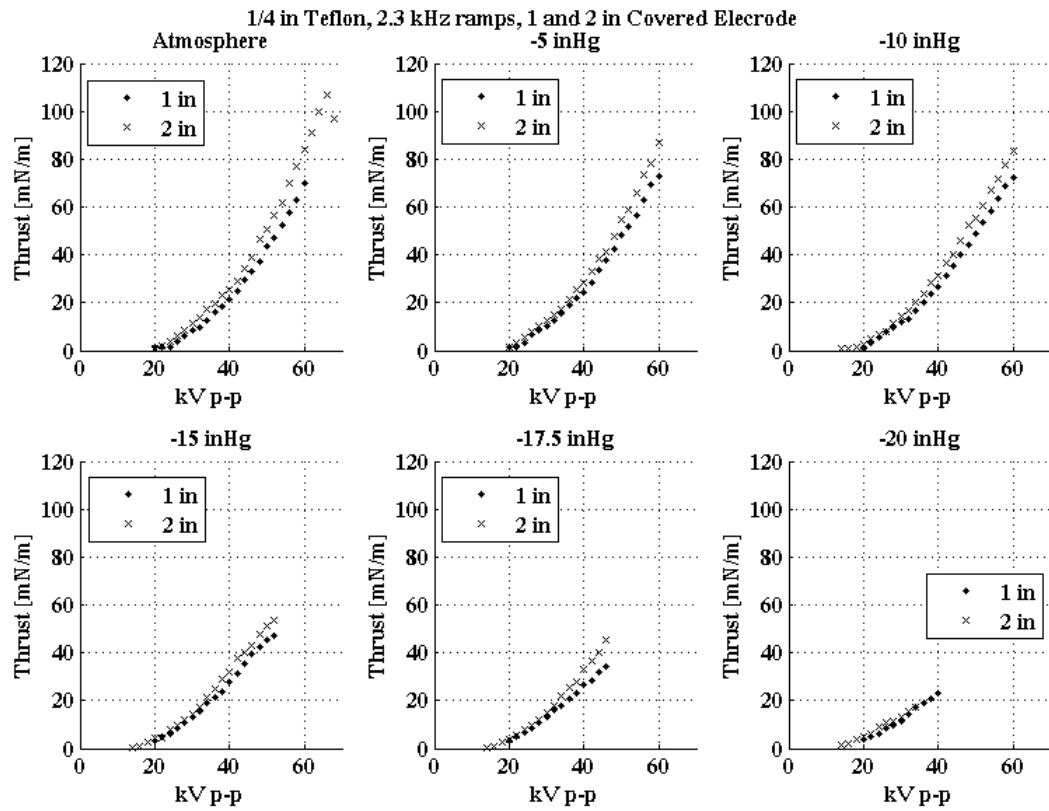


Figure 8.9. Thrust measurements for a 1/4 in thick Teflon dielectric with 1 in and 2 in wide covered electrodes at different ambient pressures.

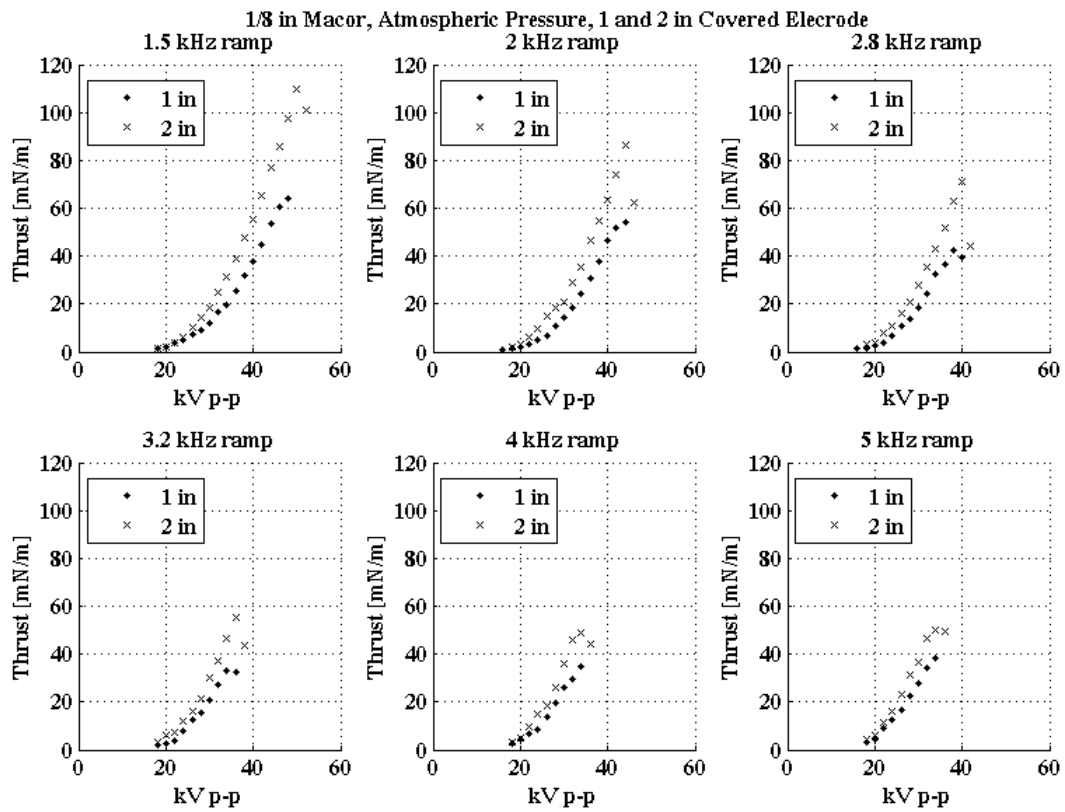


Figure 8.10. Thrust measurements for a 1/8 in thick Macor dielectric with 1 in and 2 in wide covered electrodes at constant pressures and different AC driving frequencies.

BIBLIOGRAPHY

- [1] C. Airiau, S. Walther, and A. Bottaro. Boundary layer sensitivity and reciprocity. *C.R. Meccanica*, 330:259–265, 2002.
- [2] J.D. Anderson Jr. *Fundamentals of Aerodynamics*. McGraw-Hill, Inc., 1991.
- [3] P. Balakumar. Stability of supersonic boundary layers on a cone at an angle of attack. 39th FLuid DYnamics CONference and Exhibit, June 22-25,2009, San Antonio, Texas AIAA-2009-3555, 2009.
- [4] Ivan E. Beckwith, Theodore R. Creel Jr., Fang-Jenq Chen, and James M. Kendall. Free-stream noise and transition measurements on a cone in a mache 3.5 pilot low-disturbance tunnel. NASA-TP-2180, 1983.
- [5] H. Bippes. Basic experiments on transition in three-dimensional boundary layers dominated by crossflow instability. *Progress in Aerospace Sciences*, 35:363–412, 1999.
- [6] A. Busemann. Aerodynamischer auftrieb bei φ
- [7] D. Bushnell. Reseaarch status/requirements and nasa applications for wall layer transition. Proceedings of the Workshop on Transition, Turbulence and Combustion, Volume I, Transition, 1993.

- [8] D. Cavalieri. On the experimental design for instability analysis on a cone at mach 3.5 and 6 using corona discharge perturbation method. M.S. Thesis, Illinois Institute of Technology, Chicago, IL, 1995.
- [9] Valery G. Chernoray, Alexander V. Dovgal, Victor V. Kozlov, and Lennart Loefdahl. Experiments on Secondary Instability of Streamwise Vortices in a Swept-Wing Boundary Layer. *Journal of FLuid Mechanics*, 534:295–325, 2005.
- [10] P. Coen, M.J. Long-Davis, and L. Provinelli. Fundamental aeronautics program supersonic project reference document. Website, http://www.aeronautics.nasa.gov/nra_pdf/sup_proposal_c1.pdf.
- [11] T. C. Corke, C. L. Enloe, and S. P. Wilkinson. Dielectric barrier discharge plasma actuators for flow control. *Annual Review of Fluid Mechanics*, 42:505–529, 2010.
- [12] Northrop Grumman. Quiet supersonic platform (qsp), shaped sonic boom demonstrator (ssbd) program. Website, 2003. http://www.faa.gov/about/office_org/headquarters_offices/AEP/supersonic_noise/media/3-Panel1-Henne_Gulfstream.pdf.
- [13] R.A.W.M. Henkes and J.L. Ingen, editors. *Transitional Boundary Layers in Aeronautics*. Royal Netherlands Academy of Arts and Sciences, December 1996. T. Lerche and H. Bippes: Experimental Investigation of Cross-Flow Instability Under the Influence of Controlled Disturbance Excitation, ISBN 0-444-85812-1.
- [14] Preston A. Henne. A gulfstream perspective on the darpa qsp

- program and future civil supersonic initiatives. Website, 2003. http://www.faa.gov/about/office_org/headquarters_offices/AEP/supersonic_noise/media/2-Panel1-Graham-Northrop.pdf.
- [15] Donald C. Howe and Kenrick A. Waithe. Quiet spike near field flight test pressure measurements with computational fluids dynamics comparisons. 46th AIAA Aerospace Sciences Meeting and Exhibit AIAA 2008-128, January 2008.
- [16] Pete Jacobs. Supersonic low disturbance tunnel nasa langley research center. Website, 2006. http://wte.larc.nasa.gov/facilities_updated/fluid_dynamics/supersonic.htm.
- [17] Yu.S. Kachanov. Three-dimensional receptivity of boundary layers. *Eur. J. Mech. B-Fluids*, 19:723–744, 1999.
- [18] R.A. King. Three-Dimensional Boundary-Layer Transition on a Cone at Mach 3.5. *Experiments in Fluids*, 13:305–314, 1992.
- [19] Eric H. Matlis. Controlled experiments on instabilities and transition to turbulence on a sharp cone at mach 3.5. PhD Thesis, University of Notre Dame, Notre Dame, IN, 2003.
- [20] R.H. Radeztsky Jr., M.S. Reibert, and W.S. Saric. Effect of Isolated Micron-Sized Roughness on Transition in Swept-Wing Flows. *AIAA Journal*, 37(11):1370–1377, 1999.
- [21] A. Santhanakrishnan and J. D. Jacob. Flow control using plasma actuators and linear/annular plasma synthetic jet actuators. 3rd AIAA Flow Control Conference, San Francisco, CA, June 5-8, San Francisco, CA.

- [22] W. S. Saric and H. L. Reed. Supersonic Laminar Flow Control on Swept Wings Using Distributed Roughness. AIAA Paper AIAA 2002-0147, 2002.
- [23] William S. Saric, Carillo Ruben C, and Mark S. Reibert. Leading-edge roughness as a transition control mechanism. AIAA Paper AIAA-98-0781, 1998.
- [24] W.S. Saric, R.B. Carrillo, and M.S. Reibert. Nonlinear stability and transition in 3-d boundary layers. *Meccanica*, 33:469–187, 1998.
- [25] W.S. Saric and H. Reed. Control of stability and transition in swept-wing boundary layers. Website. <http://flight.tamu.edu/pubs/presentations/swept-wing.pdf>.
- [26] W.S. Saric and H.L. Reed. Crossflow instabilities-theory & technology. *AIAA Paper 2003-0771*.
- [27] W.S. Saric, H.L. Reed, and D.W. Banks. Flight testing of laminar flow control in high-speed boundary layers. Paper presented at the RTO AVT Specialists' Meeting on 'Enhancement of NATO Military Flight Vehicle Performance by Management of Interacting Boundary Layer Transition and Separation', held in Prague, Czech Republic , 4-7 October 2004, Published in RTO-MP-AVT-111, 2004.
- [28] W.S. Saric, H.L. Reed, and E.B. White. Stability and transition of three-dimensional boundary layers. *Annual Review of Fluid Mechanics*, 35:413–440, 2003.
- [29] Corning SAS. Macor. Website. <http://www.corning.com/WorkArea/showcontent.aspx?id=40321>.

- [30] S. P. Schneider. Hypersonic laminar-turbulent transition on circular cones and scramjet forebodies. *Progress in Aerospace Sciences*, 40:1–50, 2004.
- [31] N.V. Semionov, A.D. Kosinov, and V.Ya. Levchenko. Experimental study of turbulence beginning and transition control in a supersonic boundary layer on swept wing. R. Govindarajan (ed.), Sixth IUTAM Symposium on Laminar Turbulent Transition, 2006.
- [32] D. Schatzman T. Wood T. Corke, F. Thomas. United states patent application us 20110120980a1, May 26, 2011.
- [33] J. Valerioti. Pressure dependence of plasma actuated flow control. MS Thesis, University of Notre Dame, Notre Dame, IN, 2010.
- [34] E. B. White and W. S. Saric. Secondary Instability of Crossflow Vortices. *Journal of Fluid Mechanics*, 525:275–308, 2005.

*This document was prepared & typeset with pdfL^AT_EX, and formatted with
NDdiss2_ε classfile (v3.0[2005/07/27]) provided by Sameer Vijay.*